Ion Beam Modification of Surfaces for Biomedical Applications

Dissertation

zur Erlangung des akademischen Grades
doctor rerum naturalium (Dr. rer. nat.)

vorgelegt dem Rat der Physikalisch-Astronomischen Fakultät
der Friedrich-Schiller-Universität Jena

von Dipl.-Phys. Jana Sommerfeld

geboren am 03.02.1984 in Berlin

Ionenstrahlmodifizierung von Oberflächen für biomedizinische Anwendungen

Die hohe Lebenserwartung innerhalb der westlichen Welt stellt die moderne Medizin vor immer neue Herausforderungen. Die Optimierung von künstlichen Implantaten (Hüftgelenken, Stents etc.) spielt dabei eine wesentliche Rolle. Diamantähnlicher Kohlenstoff (DLC) eignet sich, neben Titandioxid (TiO_2), für diese Zwecke besonders gut aufgrund seiner hohen Verträglichkeit, seiner Härte und seiner enormen Glätte.

Im Rahmen der hier präsentierten Arbeit wurde eine massenseparierende Ionenstrahlanlage wieder aufgebaut, weiterentwickelt und die mit ihr erzeugten DLC-Schichten unter Verwendung einer Vielzahl von Techniken wie atomarer Kraftmikroskopie (AFM), Sekundärelektronenspektroskopie (SEM), Raman-Spektrospkopie und Röntgenstrahlinduzierte Photoelektronspektroskopie (XPS) charakterisiert. Es wurden Parameter ermittelt, die es erlauben eine DLC-Schicht mit hohem sp^3-Gehalt ($> 70\%$), genügend glatter Oberfläche (RMS $<$ 1 nm) und mit einer experimentell gut weiterverwendbaren Schichtdicke (50 nm) herzustellen.

Die Biokompatibilität sämtlicher erzeugten Schichten wurde mittels Adsorptionsexperimenten überprüft. Zu diesem Zweck wurde menschliches Fibrinogen (HPF) verwendet, da es erstens einen ambiphilien Charakter hat, der es dem Protein erlaubt auf hydrophilen Oberflächen eine andere Konformation einzunehmen als auf Hydrophoben, und zweitens ist HPF von besonderem Interesse aufgrund seiner wichtigen Rolle im Blutgerinnerungsprozess.

Zunächst wurde die Adsorption auf Silicium, TiO_2 und Graphit (HOPG) untersucht, da deren Oberflächenchemie bekannt ist und sie somit als Referenzen dienten. Auf diesen Materialen wies HPF starke Unterschiede in seinem Adsorptionsverhalten auf. Während es auf Silicium und Titandioxid einen dichten Film bildete, war auf HOPG die Ausbildung eines großflächigen Netzwerkes zu beobachten. Anschließend wurde die Adsorption von HPF auf flachen DLC-Schichten mit unterschiedlichem sp^3-Gehalt untersucht. Generell zeigte sich, dass DLC einen eher hydrophilen Charakter aufweist und gut biokompatibel ist. Darüber hinaus wurde eine Abhängigkeit vom sp^3-Gehalt festgestellt. Es wurde jedoch nicht klar, ob dies tatsächlich an der Oberflächenchemie lag, oder an den unterschiedlichen Rauigkeiten, die die Proben aufwiesen.

Um dem nachzugehen, wurden beide Ansätze, d.h. die Veränderung der Oberflächenchemie und die der Topographie, getrennt untersucht. Die Chemie der DLC-Schichten wurde durch ionenstrahlinduzierte Dotierung mit unterschiedlichen Ionenspezies (Ag, Ti) in unterschiedlichen Konzentrationen untersucht. Adsorptionsexperimente zeigten, dass weder die Ionenart noch deren Konzentration (< 10 at.%) einen Einfluss auf die HPF Moleküle haben. Die Oberflächentopographie von Silicium, Titandioxid wurden durch Ionenbestrahlung unter nicht-senkrechtem Einfallswinkel verändert. Die dabei erzeugten regelmäßigen Wellenmuster (auch Ripples genannt) wurden charakterisiert und ihre Abhängigkeit von der verwendeten Ionenenergie untersucht. Außerdem wurden Ripples auf Silicium zusätzlich mit DLC beschichtet, um somit DLC-Ripples zu erhalten. Erneut wurde das Adsorptionsverhalten von HPF auf sämtlichen Ripple-Proben in Abhängigkeit der jeweiligen Wellenlängen untersucht. Aufgrund des strukturierten Untergrundes, dessen Dimensionen sich mit denen des verwendeten Moleküls decken, war eine eindeutige Auswertung nicht immer möglich. AFM Messungen weisen darauf hin, dass sich Proteine auf Oberflächen so ausrichten, dass die Oberflächenbedeckung maximiert wird. Im Falle von Ripples bedeutet dies eine Orientierung entlang/über die Ripplerücken, da somit die Interaktion der Proteine untereinander gestärkt werden kann. Im Falle von Titandioxid hatten die Ripples den stärksten Effekt, da HPF auf Ripples, deren Wellen-

längen im Rahmen der Proteingröße lagen, nicht beobachtet wurden.

Zusammenfassend lässt sich feststellen, dass das Zusammenspiel von Chemie und Morphologie einer Oberfläche einen starken Einfluss auf die Biokompatibilität hat. Es wurde gezeigt, dass beides mit Ionenstrahlen gezielt verändert und somit in gezielter Weise eingestellt werden kann.

Contents

1 Introduction

"A biomaterial is a substance that has been engineered to take a form, which, alone or as part of a complex system, is used to direct, by control of interactions with components of living systems, the course of any therapeutic or diagnostic procedure, in human or veterinary medicine." *D. F. Williams [Wil09]*

Human life expectancy increased significantly within the last century. Worldwide, people are expected to reach an average age of 70.5 years[1]. In first world countries, this number is even higher. For example, people in Germany are expected to become on average 81 years old. At the beginning of the 1980s, life expectancy for the people in Germany was only 73 years.[2] Reasons for this increase are diverse. Political, as well as, economic stability are crucial contributing factors. These factors contribute to the perpetual improvements in medicine, making it possible to reach still higher ages. 'Getting old' is typically attended by physical limitations that might require surgery. The number of surgeries requiring artificial replacements, such as hip joints or stents, is increasing constantly. In order to fulfil Williams' initially presented definition of a biomaterial [Wil09], replacements must meet many requirements. Foremost is compatibility with the human body environment. The human body's natural reaction to any foreign matter is repulsion. According materials must have a high degree of biocompatibility. Depending on the place and function, this requires that materials are not cytotoxic or carcinogenic and must be, for instance, antibacterial. Interest is increasing in non-allergenic covered materials as more people are found to have allergies to nickel, for instance, which is part of most stainless steels. Intolerances cause difficulties during the healing process requiring further treatments, even surgery. Additionally, artificial replacements must often withstand physical stress. Affordability and ease of manufacturing are also major considerations.

Acceptance of artificial replacement by the human body is chiefly determined by cell and platelet adsorption out of the human environment, which in turn is mediated by protein adsorption on the surfaces of the corresponding device. [Doo84, Lin86, Roa05] Therefore, finding optimized functional materials that are able to attract or repel specific molecules is a strong focus of life sciences. [Rie11, Lor10, Stu10] Development of new materials may

---

[1]http://data.worldbank.org/indicator/SP.DYN.LE00.IN/countries?display=graph, 03.03.2014
[2]http://data.worldbank.org/indicator/SP.DYN.LE00.IN/countries/1W?display=default, 28.02.2014

hold familiar and unknown problems. Moreover, regulatory affairs take time and money detracting from these goals. Thus, focusing on improvements of already existing materials seems promising.

In its untreated form, diamond-like carbon (DLC) has remarkable properties regarding its use in medicine. There are two possible applications for DLC layers. First, DLC reduces wear in load bearing joints due to its extremely smooth and resistant surface. Second, being highly heamocompatible, it is used as cover material for implants that are in direct contact with blood, such as heart valves and stents. For the latter case, the surface is most crucial. Apart from the influence of the surface's texture, its chemical composition is a promising research field. By adding different doping species into DLC, its properties can be altered, allowing a customization of the material for a certain purpose. For instance, dopants, such as Cu, Ag and V, influence its toxicity. These elements are released from the material when put into a biological environment and thereby cause an antibacterial effect. [Hau03] It is possible to introduce a variety of elements into DLC and still maintain its structure.

Another widely used 'biomaterial' is titanium dioxide. Liu et al. [Liu04] presented, in their detailed review article, many possible applications for titanium and titanium alloys, such as hard tissue replacements and within the cardiac and cardiovascular system. These applications are possible due to the strength and corrosion resistance of titanium-based materials. Recent studies show optimum biocompatibility of titanium nanotubes [Wan14] or titanium dioxide films, whose surface was modified with an aerosol beam and a femtosecond laser [Shi14].

Within recent years, studies indicate that not only the material itself but also its topography has an influence on the interaction with biological material. It was shown that structuring in the range of tenths to hundreds of nanometers affects the orientation of some proteins and the arrangements of cells. [Ras94, Rie11, Shi14]

The aim of this work is to investigate the possibilities to influence the adsorption behaviour of biological molecules on medically relevant materials. The focus is on the possibilities that are provided by means of ion beam irradiation. Irradiation with ion beams enable changes in the physical, as well as, the chemical properties of a substrate and its surface. As illustrated in Figure 1.1, the term 'physical effects' refers to the synthesis of layers by ion beam deposition, the creation of so-called ripple structures on a given substrate or

the introduction of a certain pattern by ion beam irradiation. 'Chemical effects' include doping of a substrate and the change of its stoichiometry. These properties can be altered by ion beam irradiation under controlled conditions.

The various experiments performed within this thesis and the individual steps are illustrated in the bottom line of Figure 1.1. Hydrogen-free diamond-like carbon layers with a high degree of 'diamond-likeness', called tetrahedral amorphous carbon layers (ta-C), were synthesized via mass-separated ion beam deposition. The ion beam accelerator, used for these purposes was rebuilt, aligned and optimized at the beginning of this work. This made it necessary to investigate in detail the parameters of the ion source and ion beam performing elements on the energy and flux of the ions, which hit the target. The influence of the ion deposition energy and fluence was of particular interest in order to be able to tune the ta-C layers' 'diamond-likeness' and thickness. The obtained samples were investigated via Raman spectroscopy, scanning electron microscopy (SEM), X-ray photoelectron spectroscopy (XPS) and atomic force microscopy (AFM). The surface chemistry of ta-C layers was further altered by doping with silver and titanium. Next to different dopants, the influence of a dopant's concentration on the biocompatibility was investigated as well. According simulations were performed and compared to determine the necessary implantation parameters.

In order to investigate the influence of morphological changes, ripples were created on silicon, titanium dioxide and, for the first time, ta-C surfaces. The energy dependency of ripple characteristics such as wavelength and amplitude was determined via AFM. The influence of this morphological change on the hydrophobicitiy was investigated via contact angle measurements (CAM). In order to look for stoichiometrical changes, XPS measurements were performed.
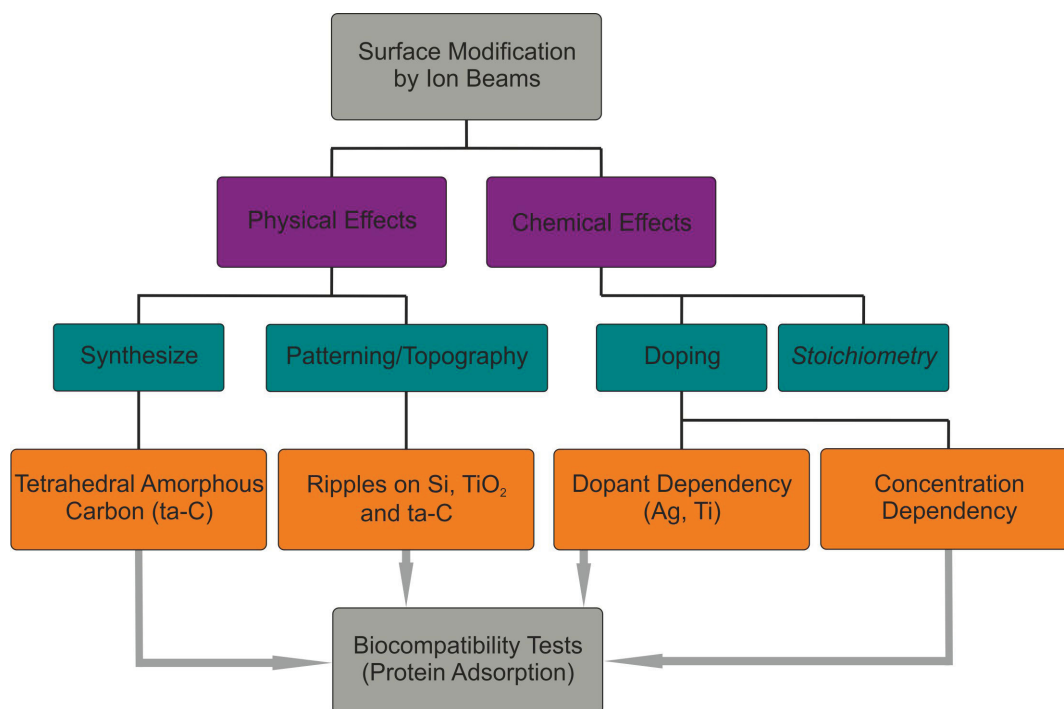
Figure 1.1: *Flow chart of the possibilities to modify surfaces by ion beams. Physical, as well as chemical properties can be altered by means of ion beam irradiation. For the work at hand, tetrahedral amorphous carbon (ta-C) layers were synthesized. Their morphology was altered by introducing so-called ripples, as was done for silicon and titanium dioxide (TiO₂) substrates. By doping ta-C with different dopants (silver and titanium) and varied concentrations (for silver), the surface chemistry was changed as well. The biocompatibility of all substrates was investigated by protein adsorption experiments. Ion beams also enable stoichiometrical changes but were not performed for this work (italic).*

The biocompatibility of the obtained surfaces was tested by performing protein adsorption experiments, as proteins are among the first molecules, which interact with the material when it is introduced into the human body. Human plasma fibrinogen (HPF) was used for these experiments for various reasons. First, it is well known and quite important for the blood coagulation process. Second, it has an ambiphilic character, meaning it contains hydrophilic and hydrophobic parts. HPF even does take different conformations on surfaces with different hydrophilicities, making it possible to conclude the state of the surface from the conformation, in which the protein adsorbs. Lastly, dealing with HPF does not require any special laboratory equipment or safety measures. Due to the nanometer dimensions of HPF and its susceptibility to damage outside of a biological/chemical environment, the adsorbed molecules were investigated via AFM.

2   Fundamentals

This chapter is an overview concerning the properties of the involved materials and their synthesis. A general understanding is delivered regarding tetrahedral amorphous carbon (ta-C) as a biomedically interesting material. Specifically, the synthesis of ta-C will be explained in detail as the applied mass-separated ion beam technique is seldom used. Morphological changes of the material's surfaces, such as ripples and their theoretical origin, will be presented, as well as, the characterization techniques, such as atomic force microscopy (AFM), X-ray photoelectron spectroscopy (XPS), contact angle (CAM) and scanning electron microscopy (SEM). A short introduction into the biological aspects of this thesis concerning the characteristics of human plasma fibrinogen will also be given.

2.1   Tetrahedral Amorphous Carbon

2.1.1   Classification

One cannot write about carbon without mentioning it as one of the most abundant elements in our planet (6th most common) and exists in 94% of all known substances. [Erd06] Carbon is by far one of the most important building blocks of modern life. Whether we look at its use as jewellery (diamonds) or as graphite with clay (for use in pencils), or its rather highly technical use as reinforcement in construction (carbon fiber), carbon offers a variety of applications. The most known allotropes of carbon are graphite, diamond and amorphous carbon. Though they all consist only of carbon, they vary widely in their structure resulting in decidedly different characteristics.

A carbon atom carries four valence electrons as its electronic configuration is $1s^2 2s^2 2p^2$ as shown in Figure 2.1. By excitation, it is possible to energetically promote one of the 2s electrons to a 2p state. In an sp^1 state, the 2s electron and one 2p electron form two equivalent hybrid orbitals that are able to bond with adjacent atoms in a strong, so called σ bond. The remaining 2p electrons can form π bonds, which are weaker due to their orientation, mirror symmetrical to the binding axis. When the 2s electron is energetically connecting with two 2p electrons, sp^2 hybrids are created lying trigonally oriented to each other and forming σ bonds. The fourth electron lies in the p_z orbital, perpendicular to the σ bond plane. This electron provides only π bonding. It is possible for all valence electrons to form σ bonds with adjacent atoms, but only if the 2s electron energetically

overlaps with the three 2p electrons. In this sp^3 hybridization state, all hybrids are oriented tetrahedrally to each other. [Rob86]
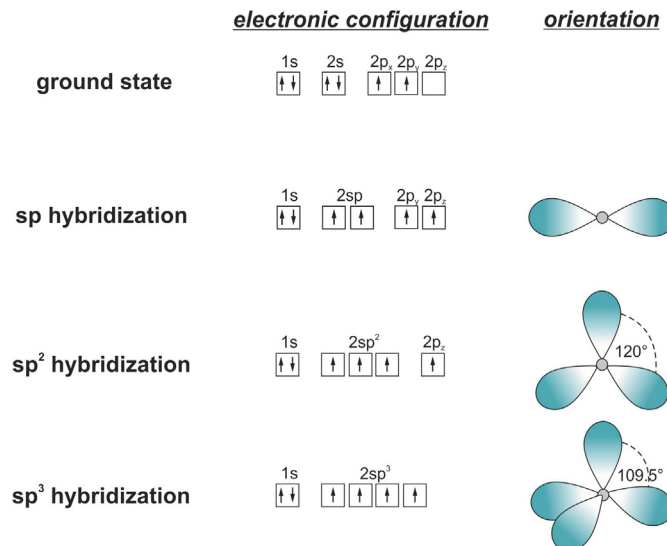

Figure 2.1: *Illustration of the various hybridization states of carbon. By excitation it is possible to promote one 2s electron to a 2p state. Thus, the 2s electron can form hybrid orbitals with 2p electrons. Depending on the hybridization state (sp, sp^2 or sp^3), different orientations are possible.*

Diamond is not only "a girl's best friend", as was musically pronounced in 1953 by Marilyn Monroe, but also a key material for a variety of application-related tools. Due to its extreme hardness of up to 100 GPa [Pan09] and its high specific resistance (higher than $10^{16}\Omega$cm [Pie93]), synthetic diamond can be used in many tribological applications, for instance, as coverage for tools [Pie93]. Due to its indirect band gap of 5.5 eV, [Dre92] diamond also qualifies as semi-conductive device and having a refractive index of 2.4 [Dre92] makes it possible for diamond to fill a niche in the optical application field. This is mainly possible by the special crystalline structure of diamond, which consists of two face-centered cubic lattices that are displaced from each other by a quarter of the space diagonal. This arrangement originates from the tetrahedral orientation of the carbon atoms, which in turn is only possible by their sp^3 hybridization. In the case of sp^3 hybridized carbon, the binding itself is covalent and has a strength of 7.36 eV/atom. The latter goes along with a lattice spacing of 154 pm. [Rie04] Although diamond offers a diversity of application possibilities, the main disadvantage of diamond is its oxidation when heated up to temperatures above 700°C in an oxygen containing environment. [Joh02]

The overall interest in **graphite** is mainly due to its highly unisotropic structure. Within one monolayer (labeled graphene), the carbon atoms are covalently bound in a hexagonal

lattice, which is possible by their sp^2 hybridization. These graphene sheets are stacked in a ABAB sequence and bound only by weak Van der Waals forces. Graphene represents an impressive electronic system as its independent particles (the π-electrons) move relativistically, but interact non-relativistically. [Gei07] The quite low specific resistance of $8 \cdot 10^{-4} \Omega$cm, combined with surprising strength along the graphene plane, make them highly desirable for electronic applications.

Apart from this strictly crystalline sp^3 or sp^2 hybridized carbon ensembles, there is also a third carbon phase, labeled **amorphous carbon (a-C)**. An extensive review about amorphous carbon, its structure and properties can be found in the work by J. Robertson. [Rob86] Amorphous carbon contains both sp^2 and sp^3 hybridized carbon atoms in which the amount of the latter determines the 'diamond-likeness' of the material. According to A. Grill [Gri99], different kinds of amorphous carbon are distinguishable. Generally, the sp^3 to sp^2 ratio and the amount of incorporated impurities such as hydrogen determine the material's properties. There are diamond-like carbon (DLC) films that contain up to 50% hydrogen (a-C:H), while others contain less than 1% hydrogen (a-C). The latter can have more than 85% sp^3 bondings. These hydrogen-free, sp^3-rich carbon layers are usually designated as **tetrahedral amorphous carbon (ta-C)**.

The ternary diagram shown in Figure 2.2a illustrates the relations between the most present hybridization states (sp^2 and sp^3) of carbon atoms within an amorphous layer and the hydrogen concentration. Tetrahedral amorphous carbon is highlighted within the diagram. A sketch of ta-C's possible amorphous structure with sp^2 (green) and sp^3 (blue) bound carbon is shown in Figure 2.2b.
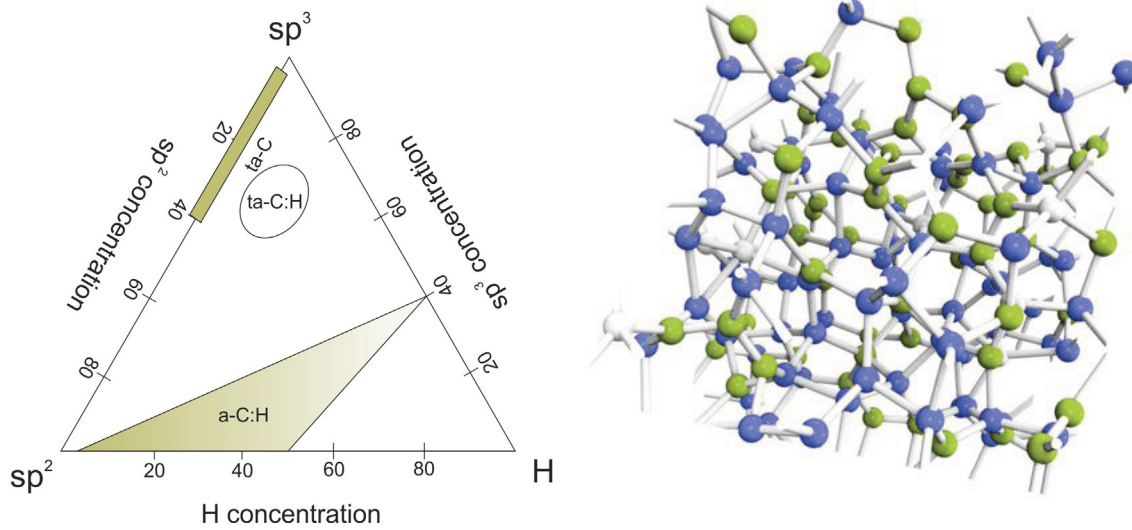
Figure 2.2: *a) Ternary phase diagram for DLC. Depending on the respective percentage within one layer, one can distinguish between several forms of carbon containing layers, such as ta-C or a-C:H that exhibit different properties. b) A sketch of the possible amorphous structure of ta-C. Green coloured carbon atoms are sp^2 bound, blue ones sp^3 bound (out of [Ric96]).*

Scientific interest in diamond-like carbon was initially shown in the early 1950's. In 1953, Schmellenmeier [Sch53] accidentally found very hard, dark accumulations of carbon *on* a tungsten cathode when he was intending to deposit carbon ('carbonize') *within* the material at low temperatures. Almost 20 years later, Aisenberg and Chabot [Ais71] successfully developed an ion beam technique to synthesize DLC out of a gaseous source. Their work was inspired by the idea that the film growth should benefit from the ions' energy rather than from heating up the substrate. They found that their obtained DLC films were transparent, highly insulating and chemically inert. Spencer et al. [Spe76] investigated in more detail the composition of ion-beam-deposited diamond-like films by means of x-ray diffraction studies and transmission electron microscopy (TEM). Although they expected to find a variety of differently hybridized carbon bonding, their films seemed to contain mostly polycrystalline diamond with grain sizes in the nanometer scale. Other groups focused more on the investigation of carbon films that were obtained by other techniques. For instance, Weissmantel et al. [Wei79] found their carbon films, that were made by ion beam plating of hydrocarbons, to have diamond-like behavior. Thereby, the diamond-likeness strongly depended on the growth conditions and the subsequent treatment. Electron diffraction analysis indicated that their 'quasi-amorphous carbon films' contain several metastable structures such as diamond clusters, graphite planes and single carbon tetrahedrals. By the end of last millennium, common techniques used

to realize diamond-like carbon layers included physical vapour deposition (PVD) and plasma-enhanced chemical vapour deposition (PECVD). [Gri99] Schultrich et al. [Sch98] figured that the energy of the impinging ions has to be high in order to obtain extremely hard ta-C films. According to him and his colleagues, film growth takes place rather by subplantation than by condensation (see chapter 2.1.2). The required high energies can be realized by a variety of techniques such as pulsed laser deposition (PLD) [Sch98, Hon98], filtered arc discharge [Chh00] or laser-controlled arc [Sch98, Sch97]. A less common technique is mass-separated ion beam deposition (MSIBD), which was introduced in the 1980's by Kasi, [Kas87] Ishikawa, [Ish87] and Miyazawa [Miy84] et al. and further developed in the 90's in the works by Lau [Lau91], Hoffsäss [Hof93] and Lifshitz [Lif96] et al. and is also the key technique to produce the ta-C layers for the work at hand.

2.1.2 Growth and Characterization

For decades, many groups investigated the growth of thin films distinguishing two stages of synthesis processes; the surface deposition, for which the carbon atoms are deposited onto the surface and form a layer, and the shallow implantation of energetic particles. The latter is also referred to as 'subplantation' and is widely accepted as the applying growth process for DLC layers [Lif90, Lif99, Rob93, Rob94, Uhl98, Hof98]: The carbon ion penetrates the substrate's surface, which is only possible if the carbon carries a critical energy. The carbon ions are trapped in a subsurface layer leading to densification. Due to successive bombardment, the target atoms are diluted until a layer containing exclusively carbon atoms evolves, which keeps growing while the bombardment continues.

There is a general agreement about the film growth; however, the actual process that determines the sp^3 content of the DLC layer is widely discussed. According to Seitz and Koeler, [Sei57] local modifications within the amorphous region originate from local relaxations in form of a 'thermal spike'. They believe these modifications either suppress or initiate the formation of sp^3 bonds. Facing the stress (caused by a density increase) driven sp^3 formation, McKenzie and Müller [McK91] proposed that the rather fast relaxation of the 'thermal spike' (called quenching) puts the carbon atoms in the metastable sp^3 state. They believe this state is thermodynamically favored in a high temperature high pressure environment that is expected within a 'thermal spike'. Molecular dynamic (MD) calculations and Monte Carlo (MC) simulations were engaged to verify some aspects

of the growth process. McKenzie [McK05] and Uhlmann [Uhl98] et al. calculated the evolution of the stress leading to the development of the layer morphology. Studies by Davis [Dav93] and Robertson [Rob94] emphasized the importance of the carbon ion energy on the film density and consequently the sp^3 content. Nevertheless, their models cannot satisfactorily explain the experimentally given energy dependency. Hence, Hofsäss et al. [Hof98] introduced the 'cylindrical thermal spike model' assuming that the layer atoms interact with each other (along the incident ion beam direction) during the relaxation process and that a sufficiently large number of rearrangement is required for the formation of sp^3-rich ta-C films. According to their findings, a universal ion energy dependency does not exist but a rather complex one that considers the thermal energy and not the ion energy. Additionally, they introduced an order parameter that enables the prediction of the most eligible ion energy range for the film growth.

The most characteristic property of a ta-C layer is its sp^3 content, as it refers to the layer's electrical and mechanical properties. Over the years, a variety of characterization techniques were employed aiming to determine the sp^3 content in a quick and precise way. An indirect method is the determination of the surface roughness. As sp^3-rich surfaces are expected to be atomically flat because of the internal growth process, it is possible to distinguish from sp^2 bound, amorphous surfaces that are rather rough due to the surface growth. [Lif95] A more direct approach is offered by Electron Energy Loss Spectroscopy (EELS). With EELS, the target is irradiated with monoenergetic electrons or X-rays. The electrons typically scatter within the sample, whereas the X-rays cause the emission of electrons. In both cases plasmons (quasiparticles that represent oscillations of the charge carrier density) are excited within the material, which leads to an energy loss of the emitted electrons. The plasmon energy is proportional to the electron density in the material. Hence, the distance between elastically and inelastically scattered electrons in the electron energy spectra gives evidence about the elements and their binding within the sample. Chhowalla et al. [Chh97] demonstrated by EELS measurements that the sp^3 content of the obtained ta-C layers from filtered cathodic arc deposition is highest when the energy of the impinging ions is around 100 eV. Works by Ronning, [Ron97] Lifshitz [Lif95], and Hakovirta [Hak95] et al. validate those findings as graphically summarized in Figure 2.3. The solid line represents an according model developed by Koponen et al. [Kop95]
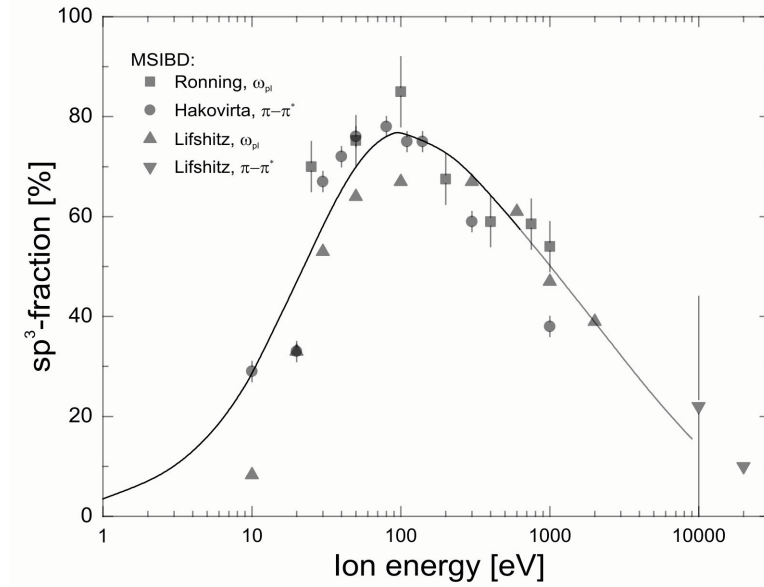
Figure 2.3: *Summary of the experimental results by Ronning [Ron97], Lifshitz [Lif95] and Hakovirta [Hak95] et al. for the sp^3 content dependency on the ion energy for MSIBD. The sp^3 content was either determined by measuring the plasmon energy (ω_{pl}) or by determining the intensity of the π-π^* transition. Both information can be gained from EELS spectra. Apparently, the sp^3 content is highest for ion energies around 100 eV. The solid line represents an according model developed by Koponen et al. [Kop95]*

According to Shindo et al. [Shi05], EELS also allows thickness measurements for DLC layers thicker than 20 nm by using a simple proportional correlation between film thickness, mean free path and EELS spectrum intensity. An extensive study about electron spectroscopic identification of carbon species was presented by Belton and Schmieg [Bel90]. Electron interactions offer one way of DLC characterization, another is provided by photon interactions. Raman measurements rely on the inelastic scattering of light (typically an argon laser) because of its interactions with the dipoles of the molecules, which causes an excitation of molecular vibrations, phonones and spin flip processes etc. within the substrate. [Kie95] These energetic interactions cause a shift in the obtained spectra that is characteristic for the investigated material. In the case of sp^2 bound carbon it is possible to excite two characteristic oscillations, the D mode around 1350 cm^{-1} and the G mode around 1580 - 1590 cm^{-1}, by irradiation in the VIS range. A sp^3 bound carbon related oscillation around 1100 cm^{-1} (T mode) [Gil00] is only detectable when the a-C material is irradiated in the UV range. Literature quotes various possibilities to extract the wanted information from the spectra. According to Gilkes et al. [Gil00], the sp^3 content can be gained by the skewness of the G mode when performing VIS Raman or by the position and relative intensities of the relevant peaks when performing UV Raman. Ferrari [Fer00], Wasyluk [Was10] and Prawer et al. [Pra96] offer similar investigations.

2.1.3 Biocompatibility and Doping

At the end of the last century, interest in improving people's health increased immensely. In the course of this new attention, industrial and research facilities all over the world pursue to develop new, not necessarily cabon-based materials or improve known ones aiming to comply with the demanding requirements for medicinal use. The application possibilities for these materials are numerous: e.g. as protective layer on artificial replacements, as dental replacement/filling and as protective layer on surgical instruments. In any case, the material will be in contact with a human body. Therefore, the material must be non-allergenic, not cytotoxic, and, importantly, easily and affordably produced. When considering application possibilities one can distinguish two kinds of implements and two kinds of effects the material should have. The first is a repelling effect that is required when the material is in contact with bacteria, fungi, or other noxious biological molecules. A bacterial repulsion is necessary when the material is used as dental replacement/filling. Almaguer-Flores et al. [AF09] investigated the adhesion of oral bacteria on amorphous films with the result that a-C was quite effective in repelling bacteria and its effect also depends on the bacterial strain itself. The possibility to decrease the formation of crystalline bacterial biofilms on ureteral stents emphasizes the use of DLC as coating material for biomedical applications. [Lau07] This was shown by a comparisons between DLC and stainless steel regarding the potential susceptibility of DLC as coating for surgical instruments. [Soi09]

Another wanted effect of DLC is an improved adhesion of biological material that makes it easier for implants to be incorporated in the human body. In this case, the hemocompatibility of the investigated material is of interest. Kocourek et al. [Koc08] investigated *in vivo* the influence of the sp^3 content and the layer thickness of DLC as coverage of textile blood vessels on their biocompatibility. They did not find any effect but the biocompatible one that is offered by DLC itself and also demonstrated by other *in vivo* and *in vitro* studies. [Uzu08, Pís13] Apparently, cell adhesion is generally improved by DLC coatings as was shown by Jelinek et al. [Jel10] Just very recently, Castillino et al. [Cas13] demonstrated that DLC coatings enable a reduction of thrombotic clots (thrombosis), which is crucial for the employment of stents in the human body. Andara et al. [And06] investigated the hemocompatibility of DLC thin films that contained metals such as silver and titanium. Apparently, metal-containing DLC exhibits an increased fibrin and platelet aggregation that might lead to thombosis. The influence of silver-doped DLC

layers on their biological activity was also observed by Chekan et al. [Che09a]. Although it is not clear how exactly dopants influence the material's hemocompatibility, there is sufficient evidence on its impact. Liu et al. [Liu08] demonstrated this by implanting phosphor, whereas Liao et al. [Lia12] showed that nitrogen doping positively effects the biocompatibility of DLC films. Grieten et al. [Gri11] focused on the influence of hydrophobicity on the adsorption behavior of proteins on nanocrystalline diamond. They came to the conclusion that hydrogenated (hydrophobic) diamond looses its biological activity, whereas oxidized (hydrophilic) diamond enables a fast protein adsorption and is highly biological active. The nanostructure of DLC thin films is suspected to have an impact on its employment for medical applications. [Nar05] Studies concerning the interaction of biological material with the substrate underneath were presented by Kowalewski and Holtzman [Kow99], who observed *in situ* conformational changes of Alzheimer's β-amyloid peptides on hydrophobic graphite. Rezek et al. [Rez10] investigated diamond-based field effect transistors in biologically relevant environments. Although there are many studies emphasizing the potential of DLC for biomedical applications, [Cui00,Roy07,All01] many of them also address the technological obstacles that have yet to be overcome. This includes difficulties covering implants homogeneously, complex geometries, and upscaling the involved carbon deposition processes to industrial standards. [Nar05]

2.2   Ripple Formation

A controlled manipulation of a surface morphology can be realized by means of ion beam erosion, which can cause a periodic structure on a nanometer scale that matches the diameter of soft matter such as proteins or other biological materials. When an energetic ion hits a target, its energy is transferred to the target system and the ion is implanted into the target. The resulting Gaussian distribution $F_D(\vec{r})$ of the energy deposited per unit volume, concerning its average depth and range, is typically characteristic for the target-ion-system studied. According to the work of Sigmund [Sig73], this distribution along the z direction depends on the ion energy ϵ, the average energy depth a and the energy distribution's range, parallel (α) and perpendicular (β) to the incident ion beam:

$$F_D(\vec{r}) = \frac{\epsilon}{(2\pi)^{\frac{3}{2}}\alpha\beta^2} \cdot \left(-\frac{(z-a)^2}{2\alpha^2} - \frac{x^2+y^2}{2\beta^2}\right). \tag{2.1}$$

If the impact energy is high enough, and the energy devolution takes place close to the surface, a fraction of target atoms will be sputtered off the substrate. The sputter yield depicts the fraction of sputtered surface atoms in relation to the impinging ions. Consequently, the sputter yield $S(\vec{r})$ for a surface element dA is proportional to the energy transferred to a certain point of the surface. The target material and its condition (impurities, surface etc.) impact the sputter yield; a constant γ refines the relation:

$$S(\vec{r})dA = \gamma F_D(\vec{r})dA. \tag{2.2}$$

As seen in Figure 2.4a, the sputter yield is highest where the maximum deposited energy is closest to the surface. The ion has an initial momentum when hitting the target; however, the maximum deposited energy is located further down in the sample. In the shown case, the ion impinges the surface at point O, but the point of the maximum deposited ion energy is closest to the surface at point C. Thus, by tilting the surface off the ion beam direction, a shift of the sputter yield maximum in relation to the ion impact point is achieved. As a consequence of this effect, the surface evolution by sputtering of a non-flat and structured surface is irregular. When an ion hits a structure at point A, as shown in Figure 2.4b, its entire energy is effective at this point. At point B, the surface atoms are affected by the ion energy that was introduced at point B and also by the ion energy that was introduced at point A due to the effect explained above. This pattern holds valid for the other points further down the surface. At point D, the energies deposited at C, D and E impact the sputter yield. Because of the different sputter yields for each point of the surface, the final surface (Figure 2.4c) is altered morphologically. Ultimately, a roughening of the surface occurs on all scales where structures with a high aspect ratio show an increase in amplitude.
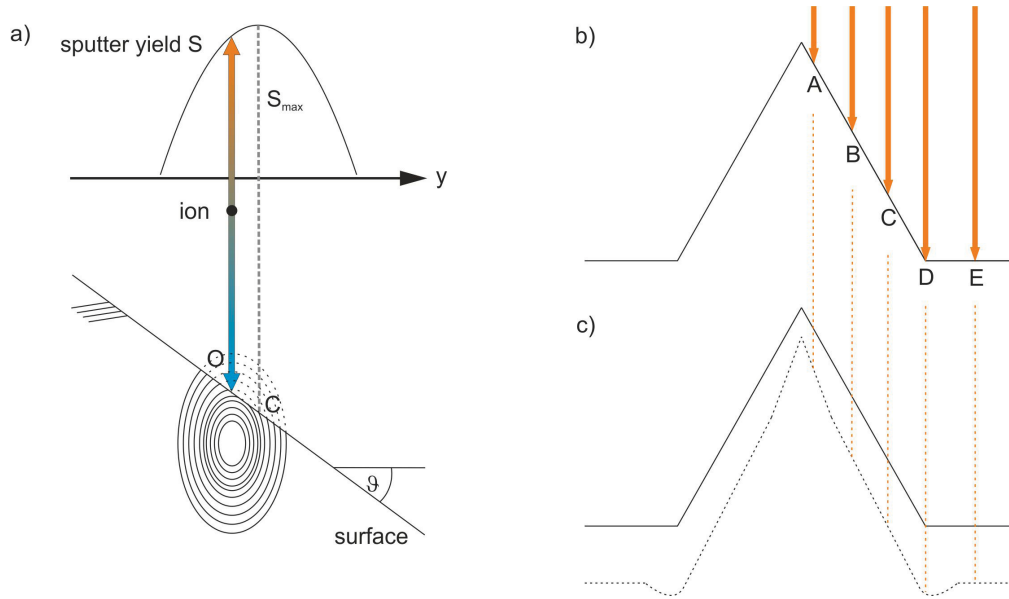
Figure 2.4: *a) Sputter yield distribution (top) for a surface that is tilted regarding the ion beam direction. The tilting angle is ϑ. The sputter yield S is highest for the point C of the surface that is closest to the maximum of the energy that was introduced by an ion that impacted at point O. b) Alteration of a surface due to ion irradiation and sputtering. At point A, only the energy that was introduced at this point is effective. At point B, the energies deposited at point B and A contribute to the sputter yield. This differences concerning the introduced ion energy at each point of the surface cause an irregular sputter yield (c).(from [Sig73])*

The described roughening of the surface causes an instability of the surface, which in competition with smoothing effects, results in periodic structures. Bradley and Harper [Bra88] developed a **linear theory** for ion-induced ripple formation on amorphous targets according to which the smoothing is caused by thermally activated self diffusion acting most effectively on short distances. Note: although smaller wavelengths of the periodic structures with high aspect ratios are favored concerning their amplitude's amplification, self diffusion is effective as well. Periodic structures are formed if roughening outweighs smoothing for a range of wavelengths. The observed structure wavelength is the one with the highest amplitude gain while accounting the smoothing effects present. Bradley and Harper also emphasized the importance of the local surface curvature R for the sputter yield. [Bra88] Thus, for the calculation of the sputter yield at one point, the introduced energy at the surrounding surface points has to be integrated. Referring to Figure 2.4, this means that for the calculation of the sputter yield at point C, the introduced ion energies of all points O have to be taken into account. For simplification, the following assumptions were made: The coordinate system has its origin in C and its z direction along the local surface normal. The x axis lies in the plane of incidence and for y, no surface dependency is assumed, leaving a two dimensional problem. Furthermore, the

curvature of the surface is supposed to be much larger than the depth (a) and the range (α, β) of the deposited energy distribution. This assumption allows an approximation concerning the change of the surface's curvature amplitude h for $|x| \lesssim a$:

$$h(x) \approx -\frac{1}{2}\frac{x^2}{R}. \tag{2.3}$$

With ϑ being the angle between incident ion beam and surface normal, the flux in point O (x, h(x)) satisfies $f[\cos\vartheta - \left(\frac{x}{R}\right)\sin\vartheta]$, considered as first order in $\frac{x}{R}$. It is now possible to calculate an erosion rate $\nu(\vartheta, R)$ in first order at $\frac{a}{R}$ using an ion fluence Θ, the particle density n in the target, and the sputter yield $S_0(\vartheta)$ for a flat surface [Bra88]:

$$\nu(\vartheta, R) = \frac{\Theta}{n}S_0(\vartheta)\left(\cos\vartheta + \Gamma_x(\vartheta)\frac{a}{R}\right). \tag{2.4}$$

Note, that the influence of the curvature on the erosion time is accommodated by Γ_x, for which the following relation with the according coefficients that are dependent on the introduced energy's distribution can be found:

$$\Gamma_x(\vartheta) := \frac{A}{B_1}\sin\vartheta - \frac{B_2}{2B_1}\left(1 + \frac{A^2}{B_1}\right)\cos\vartheta - \frac{AC}{B_1^2}\left(3 + \frac{A^2}{B_1}\right)\cos\vartheta \text{ with} \tag{2.5}$$

$$A = \left(\frac{a}{\alpha}\right)^2\sin\vartheta, \tag{2.6}$$

$$B_1 = \left(\frac{a}{\alpha}\right)^2\sin^2\vartheta + \left(\frac{a}{\beta}\right)^2\cos^2\vartheta, \tag{2.7}$$

$$B_2 = \left(\frac{a}{\alpha}\right)^2\cos\vartheta, \text{ and} \tag{2.8}$$

$$C = \frac{1}{2}\left[\left(\frac{a}{\beta}\right)^2 - \left(\frac{a}{\alpha}\right)^2\right]\sin\vartheta\cos\vartheta. \tag{2.9}$$

These coefficients are positive for $0 < \vartheta < \frac{\pi}{2}$. Assuming a negative curvature (valley), the term $\Gamma_x(\vartheta)\frac{a}{R}$ in equation (2.4) becomes positive, whereas it remains negative for positive curvatures (hills). Consequently, erosion takes place faster for valleys than for hills. Considering the corresponding coefficient for the y direction

$$\Gamma_y = -\frac{\beta^2}{a^2}\cos\vartheta\left(\frac{B_2}{2} + \frac{AC}{B_1}\right), \tag{2.10}$$

the erosion rate can be generalized as

$$\nu(\vartheta, R_x, R_y) = \frac{\Theta}{n} S_0(\vartheta) \left(\cos\vartheta + \Gamma_x(\vartheta)\frac{a}{R_x} - \Gamma_y(\vartheta)\frac{a}{R_y} \right). \tag{2.11}$$

As the chosen coordination system does not necessarily equal the laboratory system, an approximation for the microscopic incident angle seems appropriate, including the macroscopic incidence angle Φ and the local slope of the surface $\frac{\partial h}{\partial x}$:

$$\vartheta \approx \Phi + \frac{\partial h}{\partial x}. \tag{2.12}$$

Consideration must also be given to the surface self-diffusion that can be regarded as counterpart of the surface roughening. In the 1950's, Mullins and Herring [Mul57,Her50] developed a suitable theory in which the divergence in the material current $\vec{j}(x, y, t)$ contributes to the surface velocity:

$$\frac{\partial h}{\partial t} = \text{div}\vec{j}. \tag{2.13}$$

The material current on the other hand is proportional to the surface potential $\mu(x, y, t)$, for small surface curvatures:

$$\text{div}\vec{j} \sim \text{grad}\mu. \tag{2.14}$$

Moreover, $\mu \sim \frac{1}{R} \approx \frac{\partial^2 h}{\partial x^2}$ applies, which leads to the final expression concerning the self diffusion,

$$\frac{\partial h}{\partial t} = -B\nabla^2(\nabla^2 h). \tag{2.15}$$

In conclusion, the following differential equation for the change of the surface height can be found:

$$\frac{\partial h}{\partial t} = -\nu_0(\Phi) + \nu_0'(\Phi)\frac{\partial h}{\partial x} + \frac{\Theta a}{n}S_0(\Phi)\left(\Gamma_x(\Phi)\frac{\partial^2 h}{\partial x^2} + \Gamma_y(\Phi)\frac{\partial^2 h}{\partial y^2}\right) - B\nabla^2(\nabla^2 h). \tag{2.16}$$

As already mentioned, perturbations with different wavelengths develop independently from each other, allowing a decomposition of the surface profile in its periodic contribu-

tions. When using the ansatz

$$h(x, y, t) = -\nu_0(\vartheta)t + A\exp(i(k_x x + k_y y - \omega t) + r_k t) \tag{2.17}$$

with real values for the wavevectors k_x, k_y, the frequency ω and the growth coefficient r_k, the following solution can be found:

$$\omega = -\nu_0'(\vartheta)k_x. \tag{2.18}$$

Thereby, the growth coefficient r_k is given by:

$$r_k = -\frac{\Theta a}{n}S_0(\vartheta)(\Gamma_x k_x^2 + \Gamma_y k_y^2) - B(k_x^1 + k_y^2)^2. \tag{2.19}$$

Naturally, the wave vector k with the highest growth coefficient dominates the surface morphology resulting in a ripple structure with $\lambda = \frac{2\pi}{k}$. Another important characteristic of the created structure is its orientation, which mainly depends on the relation between Γ_x and Γ_y. Figure 2.5a shows their dependency on the irradiation angle. For this particular example, SRIM[1] simulations have been done for xenon ions hitting TiO_2 with an ion energy of 10 keV. [Fra09] The direction of the wave vector k is determined by the Γ that has the higher value. Both Γ_x and Γ_y have two interception points ($\vartheta = 0$ and $\vartheta = \vartheta_c$) for which no direction dominance is expected. If the incident ion beam angle ϑ is smaller than a critical angle ϑ_c, the referring $\Gamma_x(\vartheta)$ is also smaller than $\Gamma_y(\vartheta)$. Hence, the wave vector in x direction dominates ($\vec{k} = k_x \vec{e}_x$), resulting into ripple structures perpendicular to the ion beam. In case of ϑ being higher than ϑ_c, the same applies for the y direction ($\vec{k} = k_y \vec{e}_y$), resulting into ripple structures parallel to the ion beam, as is illustrated in Figure 2.5b.
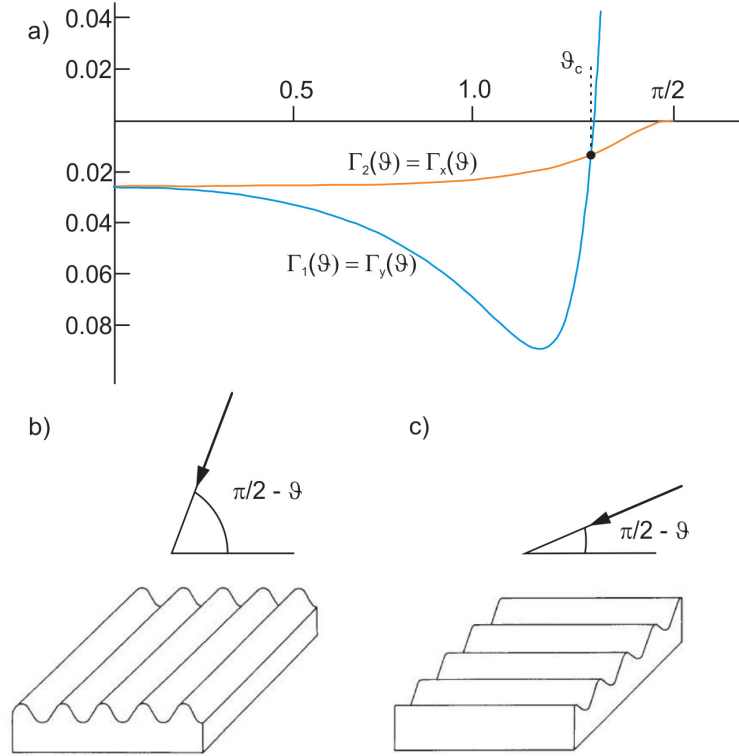
---

[1]www.srim.org

Figure 2.5: *a) Results of the SRIM calculation for TiO_2 irradiated with 10 keV xenon ions under varied ion beam angles.(after M. C. Fravventura [Fra09]) For $0 < \vartheta < \frac{\pi}{2}$, Γ_x and Γ_y remain negative leading to a faster development of surface disturbances with a positive curvature (hills). Their orientation is governed by the Γ-term that is more negative (higher absolute value). b + c) Resulting ripple orientations. For small ion beam angles the ripples are orientated parallel to the ion beam direction, whereas for larger ion beam angles, the orientation turns perpendicular.(after Bradley et al. [Bra88])*

Considering the above, it is possible to express the wavelength as:

$$\lambda = 2\pi\sqrt{\frac{2nB}{\Theta a S_0(\vartheta)|\Gamma_{x,y}|}}, \tag{2.20}$$

where $\Gamma_{x,y}$, S_0 and the average penetration depth a depend on the ion's energy. For the latter, the following approximation was presented by Sigmund [Sig69]:

$$a \sim \epsilon^{2m}. \tag{2.21}$$

The exponent $m = m(\epsilon)$ develops rather slowly, ranging from 0 for low ion energies to 1 for high energies. Within the low ion energy range of this work, m can be considered as constant. Furthermore, Sigmund states that $m \approx \frac{1}{3}$ for ion energies in the range of keV. The range (α, β) of the energy distribution is also dependent on the penetration depth a.

The sputter yield incorporates the mentioned dependencies:

$$S_0 \sim \frac{\epsilon a}{\alpha \beta} \sim \epsilon^{1-2m}. \tag{2.22}$$

The energy dependencies cancel each other out for $a \sim \alpha \sim \beta$, leading to

$$\lambda \sim \sqrt{\frac{1}{aS_0}} \sim \epsilon^{-\frac{1}{2}}. \tag{2.23}$$

In conclusion, and according to Bradley and Harper, the wavelength of the created ripple structure decreases for increasing ion energies. Although their theory was experimentally confirmed by many studies, some experiments caused a critical calling into question of the theory's boundaries. For instance, the linear theory predicts unlimited exponential growth of the ripple amplitude but a saturation was observed. [Vaj96,Cha01] Some studies showed other orientations than parallel or perpendicular to the incident ion beam direction. [Kop97] Studies by Umbach [Umb01] and MacLaren [Mac92] et al. gave evidence for a critical temperature, below which the ripple wavelength is independent of the temperature. These discrepancies finally lead to a **non-linear extension** by Makeev, Cuerno and Barabasi (MCB) in 2002. [Mak02] Including also higher derivations with respect to h

$$\nu(\vartheta) = \frac{\Theta}{n} S_0(\vartheta)(\cos\vartheta + \Gamma_{20}\Delta_{20} + \Gamma_{02}\Delta_{02} + \Gamma_{30}\Delta_{30} + \Gamma_{21}\Delta_{21} + \Gamma_{40}\Delta_{40} + \Gamma_{22}\Delta_{22} + \Gamma_{04}\Delta_{04}), \tag{2.24}$$

with

$$\Delta_{nm} = \frac{a^{n+m+1}}{n!m!} \frac{\partial^{n+m}}{\partial^n x \partial^m y}, \tag{2.25}$$

leads to $\Gamma_{20}\Delta_{20} = \Gamma_x \frac{a}{R}$ and $\Gamma_{02}\Delta_{02} = \Gamma_y \frac{a}{R}$. According to the MCB model, all parameters Γ_{nm} depend on the energy distribution parameters (a, α, β) and the macroscopic incident ion angle ϑ. In addition to the thermally activated surface self diffusion that was already considered in the linear model, the fluctuations of the ion beam were now taken into account in terms of noise $\eta(x, y, t)$. The average of the noise is expected to be zero ($\langle \eta(x, y, t) \rangle = 0$). The remaining terms $\Gamma_{40}\Delta_{40}$, $\Gamma_{22}\Delta_{22}$ and $\Gamma_{04}\Delta_{04}$ behave like a ion-induced effective surface diffusion. Along the lines of thermally activated surface

diffuion, MCB introduced a surface constant D. [Mak97] According to their findings, the linear model is confirmed for $D << B$ and short erosion times. For longer time periods, non-linear effects occur, leading either to a stabilization of the ripple wavelength or to the appearance of differently orientated structures or surface winkling. For $D >> B$, additional wavelengths appear parallel or perpendicular to the incident ion beam:

$$\lambda = 2\pi \sqrt{\frac{2nD}{\Theta a S_0(\vartheta)|\Gamma_{x,y}|}}.$$ (2.26)

This relation leads with $D \sim \frac{\epsilon a^4}{\alpha \beta}$ for $\frac{a}{\alpha} = const.$ and $\frac{a}{\beta} = const.$ to the energy dependency

$$\lambda \sim a \sim \epsilon^{2m}.$$ (2.27)

Consequently, there is a completely different wavelength dependency on the energy for small temperatures (causing negligible thermally activated surface self diffusion). In the non-linear mode, the wavelength increases with increasing ion energy.

It needs to be mentioned that, next to the non-linear effects described by MCB, shadowing effects can lead to a dependency of the wavelength on the applied fluence or to a saturation of the ripples' amplitude. Carter et al. [Car99] observed that as soon as the local surface curvature exceeds the microscopic incident ion angle, the ions are hindered in hitting also the ripple valleys, which leads to a terrace-like flattening of the originally sinus-shaped ripples. The maximum tilting angle of a sinus-shaped surface depends on the ripple wavelength and the ripple amplitude A

$$\alpha_{max} = \arctan\left(2\pi\frac{A}{\lambda}\right).$$ (2.28)

Thus, shadowing effects are very likely for ripple structures with small wavelength but high amplitudes.

However, within the last five years, new interpretations concerning ripple formation were established. Molecular dynamic simulations by Kalyanasundaram et al. [Kal08] suggest that mass redistribution induced by ion beam irradiation is the determining factor, not ion-beam erosion due to sputtering. Madi et al. [Mad11] support this view. They split the curvature coefficient $S_X(\Theta)$, which determines the linear instability or stability of an ion

beam-eroded surface, into an erosive component $S_X^{erosive}(\Theta)$ (Bradley-Harper model) and a mass redistribution component $S_X^{redist.}(\Theta)$ (Carter-Vishnyakov model [Car96]). They showed that the erosive contribution to an instability, that is essential for the formation of a surface curvature, is negligible. According to their work, the prediction of the Bradley-Harper model is of the wrong sign and predicts too small a magnitude. Moreover, they show that the topographic instabilities are caused by atomic redistributions due to the ion impact. However, Madi et al. also point out the possibility that erosion is of some importance at higher ion energies, as their study only dealt with an ion energy of 1 keV. Hofsäss et al. [Hof13a] support the importance of mass redistribution by according studies for energies up to 10 keV. W. Möller [Möl14] recently developed the new program TRI3DYN, which enables the simulation of the ripple formation process. His study confirms the importance of mass redistribution for ripples formation by showing that periodic ripple pattern evolve when there is no sputtering, and that the caused lack of surface erosion increases the wavelength. He shows that the roughness and wavelength increase significantly due to redeposition processes. Note, these simulations were carried out for low energy (250 eV) ion irradiation and thus, do not exclude any influence of sputtering for higher ion energies that are mostly used in this thesis. This alleged energy dependency was investigated in detail by H. Hofsäss. [Hof14] He suggests that curvature-dependent erosion has an effect on pattern formation but not for low energies. For these low ion energies, he claims the domination of mass redistribution. Additionally, Hofsäss et al. [Hof13c] observed ion beam-induced pattern formation on silicon under normal ion incidence and with metal atom co-deposition, contradicting the curvature dependency established by the Bradley-Harper model, as well as Bradley's recent extension [Bra12] of this very model. The observed pattern formation strongly varied for different metals, which is not explainable only by collision cascade effects (such as sputtering or mass transport). Certain metals (Fe, W, Mo, Ni) caused a phase separation within the irradiated silicon and triggered the formation of ripples. The stronger the metals' ability to form a silicon-rich silicide ($MeSi_2$), the more pronounced was the observed ripple pattern. The formation and the propagation of ripples under ion beam irradiation is vividly debated [Hof13b, Bra13], which only emphasizes that there is still plenty of room for discussions and need for experimental evidence in order to unambiguously understand the origin and process of ripple formation.

2.3   Human Plasma Fibrinogen

A general understanding of the biocompatibility can be gained by investigating a substrate's interface with simply structured soft matter such as cells, bacteria or proteins. The glycoprotein human plasma fibrinogen (HPF) is well know for its importance for the blood coagulation process. [Sch57] It is generated in the liver of vertebrates and then introduced to the blood plasma. In case of blood coagulation, HPF is transformed into fibrin by the enzyme thrombin and calcium. This fibrinogen-fibrin conversion is explained in more detail by Scheraga and Laskowski. [Sch57] The fibrin creates a mesh that interacts with other cellular elements of the blood (such as platelets). Thus, a thrombus is formed that seals the wound.

Next to its undoubted function in the human body, another asset of HPF is the fact that its structure is well understood. [Doo84, Cac00, Hal59] Most notably, HPF has an amphiphilic character that causes its hydrophobic and hydrophilic parts to be attracted to hydrophobic and hydrophilic surfaces, respectively, assuming different conformations. As can be seen in Figure 2.6a, the structure of HPF consists of two hydrophobic domains, E and D, which are built up of individual amino acids. At the outer ends of the protein are carboxyl groups (α chains) with a hydrophilic character. [Fen95] Hence, it is possible for HPF to undergo conformational changes depending on the environmental conditions.
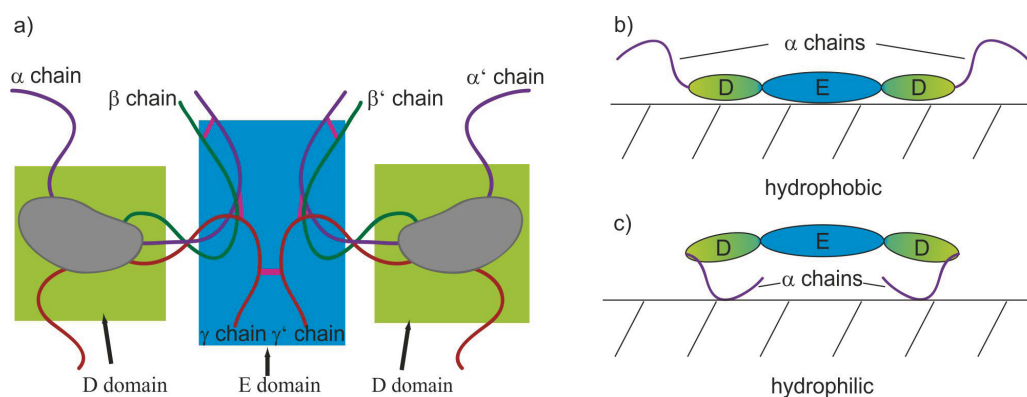

Figure 2.6: *Schematic sketch of the HPF molecule. a) The hydrophobic E and D domains consist of amino acids; whereas, its hydrophilic α chains at the outer ends are based on carboxyl groups. This ambiphilic structural allows a conformational change after the adoption on a material. b) On hydrophobic surfaces, the hydrophobic domains D and E preferentially adsorb, which results in a stretched conformation. c) The hydrophilic α chains are more attracted to hydrophilic surfaces. The chains interfold for the latter case in order to improve the connection to the surface, leading to a rather globular structure.*

According to the experimental findings by Marchin and Berrie [Mar03], the hydrophobic domains preferentially adsorb on hydrophobic surfaces. Owing to the ambition of each domain to connect with the surface, HPF finally adsorbs in a stretched formation as illustrated in Figure 2.6b, enabling the α chains to interact with each other assuming two or more proteins are close enough. On hydrophilic surfaces, the attraction of the hydrophilic α chains to the surface dominates. The α chains fold underneath the E and D domains resulting in a more globular conformation (see Figure 2.6c). HPF consists of 3410 amino acids in total and when surface-bonded, it has a length of 46 - 49 nm and a height of about 0.3 - 2.5 nm. The exact dimensions depend on the protein conformation on different substrates and under different environmental conditions. [Cac00, Mar03, Agn04, Sit99, Kee08] Former studies mostly investigated the adsorption of HPF and a variety of other proteins [Vie09, Kim03] on flat substrates such as commercially pure Ti with a natural TiO_2 layer on top [Kee08], TiO_2 [Cac00], graphite [Mar03, Agn04, Ta98], mica [Mar03, Sit99, Kee08], ultra-high molecular weight polyethylene [Kel11], Si [OV98, Tun05] or SiO_2 [Jun03]. In most cases, these investigations concentrated on the adsorption of single proteins in air and/or under aqueous conditions. These works come to the general conclusion that the adsorption behavior is mainly given by the chemistry of the surface. For instance, Agnhihotri et al. [Agn04] investigated time-dependent changes in orientation HPF underwent on hydrophobic HOPG and hydrophilic mica. According to their findings, HPF is kinetically more active on hydrophilic surfaces than on hydrophobic surfaces, which results in a stronger adsorption on the latter. Cacciafesta et al. [Cac00] observed single HPF molecules on TiO_2, where the protein adsorbed in trinodular conformation.

Cai et al. [Cai06] gave evidence that the surface roughness has hardly any effect on the protein adsorption. In contrast to this, another study by Rasmusson et al. [Ras94] links the formation of HPF to the curvature of the investigated surface. Thus, the influence of the surface morphology on the nanoscale seems to be minor as deduced from the previous studies for protein absorption. It was recently shown that osteoblasts demonstrate an enhanced response on ion beam irradiated, rippled titanium surfaces pointing to an effect of the ripple pattern on the cell attachment process. [Rie11]

3 Experimental Techniques

3.1 Mass Separated Ion Beam Deposition

One possible way to synthesize hydrogen-free carbon layers with a high sp^3 content is mass separated ion beam deposition (MSIBD), which was established in the 1980s by several groups. [Kas87, Ish87, Miy84] This technique requires an ion acceleration unit. For this work, the low energy ion accelerator Mr. Jim Stringer was used. The setup is depicted in Figure 3.1. Within a Penning ion source, the gas is ionized by applying a negative voltage of about 2 kV resulting in a discharge current within the source of 1 - 5 mA. For the synthesis of carbon layers, carbon dioxide (CO_2) was the gas of choice as it is easily manageable and provides a sufficient yield of carbon ions. The positively charged ions were extracted from the source, because of a positive acceleration voltage to ground of 30 kV. An electrostatic Einzel lens focuses the ion beam before it enters the 90° separation magnet that follows. As it is well known, a magnetic field acting on a moving particle of a certain mass and charge causes a perpendicularly orientated Lorentz force. Due to the different masses and charges of the ions contained within the beam, the ion beam elements are spatially separated. A steerer that consists of two sets of parallel electrodes follows after the separation magnet in order to position the ion beam. The slit that follows makes it possible to chose a defined fraction of the ion beam. By mounting a Faraday Cup behind that slit and varying the magnet field, it is possible to analyze the beam's composition and by doing that to find the required magnet parameters to obtain an ion beam that consists of only carbon ions. For the work at hand, an ion beam containing only $^{12}C^+$ ions was used. When the Faraday cup is moved out of the beam line, the ion beam enters another Einzel lens that focuses the beam into a second steerer, which straightens and positions the beam in x and y direction. The quadrupole lens that follows refines the beam profile. Before reaching the deposition chamber, the beam is swept by a beam sweeper with frequencies up to 1.1 kHz. Another Faraday cup that can be moved into the beam line allows a re-check of the ion current before entering the deposition chamber. To achieve the required low ion energies of about 100 eV (see chapter 2.1.2), a deceleration of the ions is necessary. This is realized by applying the initial high voltage to the deposition chamber. Now, the ions can only enter the deposition chamber when a negative voltage is applied to the substrate itself. A simple ring electrode serves as

defocusing lens, which broadens the ion beam and forces secondary electrons that might be emitted from the sample back into the very same. An electron lens at the end of the beam line fulfils the same purpose concerning the secondary electrons that originate from the beam line's walls. The ion current on the sample is directly measured and monitored by a current integrator. A more detailed illustration of the deposition chamber and the applied potentials is presented in chapter 4.1 (Figure 4.1).
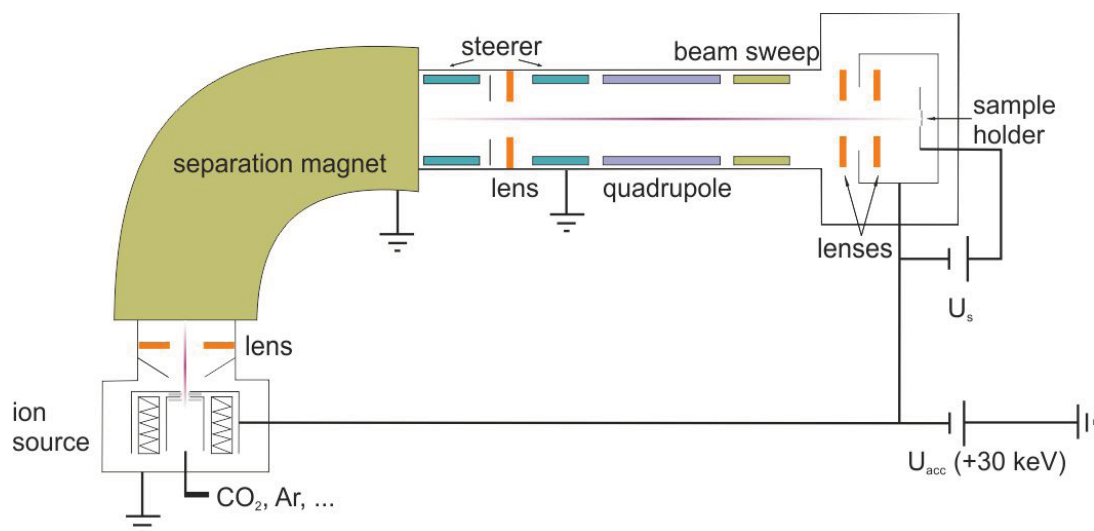

Figure 3.1: *Schematic setup of Mr. Jim Stringer. A Penning ion source ionizes the CO_2 and by applying U_{acc} = +30 kV the positively charged ions are extracted from the source. An Einzel lens focuses the ion beam onto the entrance of the 90° sector magnet that spatially separates the ion beam elements/isotopes. The following slit allows a sharp separation of the different ions assuring a pure $^{12}C^+$ beam after passing. Electromagnetic elements such as another Einzel lens, a quadrupole lens, steerer and a beam sweep enable a homogeneous scanning of the ion beam over an adequate substrate. Shortly before entering the deposition chamber, the ions are decelerated to their desired deposition energy that is usually in the range of 100 eV, by applying a negative voltage, relative to the acceleration voltage, on the sample holder (U_S = - 100 V).*

3.2 Ion Beam Implantation

In order to investigate the surface-related behavior of HPF on doped substrates, ion implantations were carried out with the aim to position dopants close to the surface. This can be done by choosing relatively low ion energies in the range of 20 keV down to a couple hundreds of eV. The same accelerator Mr. Jim Stringer was also used for this purpose. By grounding the deposition chamber and the referring power supplies, it is possible to provide ion energies up to 30 keV. For implantations with ions having less than 3 keV, the usual setup (see Figure 3.1), including deceleration, could be used as its deposition unit supplies these energies. Additionally, another ion implanter (ROMEO, manufactured

by High Voltage Engineering Europa B.V.[1]) was used providing ion energies up to 400 keV. The ions, that are extracted from a hot filament source, are mass separated by a 90° sector magnet. Integrated ion beam optics along the acceleration line assure a precise confinement of the ion beam on the sample. A 7° target setup inhibits channelling effects. Because of technical circumstances, neither Mr. Jim Stringer nor ROMEO provide ion energies between 3 and 10 keV, which are of interest for ripple formation experiments. A Low Energy Ion impLAnter (LEILA) from Colutron[2] was used for this purpose. LEILA has a hot filament source as well. The mass-charge selection is done by means of a Wien filter. A beam sweeper provides a homogeneous coverage of the sample holder. The latter can be altered concerning its orientation towards the ion beam.

3.3   Protein Adsorption

The standard procedure for the protein adsorption was conducted as follows. The samples were cleaned with ethanol and dried with compressed air and stored in an oven at 37°C in order to adjust the samples' temperature necessary for the adsorption itself. This was done to avoid triggering of actions due to temperature differences between the investigated surface and the adsorbate (here, the HPF molecule). HPF was available as lyophilized[3] powder from Calbiochem[4]. First, 1 mg of the powder was dissolved in 1 ml phosphate buffered saline (PBS) solution to obtain a stock solution, which was also heated to 37°C, for 30 minutes. The PBS was purchased from Biochrom[5] and contained no Ca^{2+} or Mg^{2+}. Second, the stock solution with a concentration of $c_{start} = 1$ mg/ml was diluted to a concentration of $c_{final} = 10$ μg/ml. The necessary values concerning the PBS solution V_{BPS} and stock solution V_{HPF} were determined by:

$$V_{BPS} = V_{HPF} \cdot \left(\frac{c_{start}}{c_{final}} - 1 \right).$$
(3.1)

This final HPF solution was heated as well. Finally, a droplet of 1 ml HPF solution was added to each sample. The samples were stored for two hours at 37°C to allow the proteins to adsorb. This temperature was chosen as it matches human body temperature.

---

[1]www.highvoltage.com

[2]www.colutron.de

[3]freeze-dried

[4]EMD Millipore Corp., Billerica, MA, USA, www.millipore.com

[5]Biochrome AG, Leonorenstr. 2-6, 12247 Berlin, www.biochrom.de

Afterwards, the samples were carefully rinsed with PBS solution and tridistilled water, prior to softly drying perpendicular to the surface in order to avoid accidental removal of the adsorbed proteins. Care was taken that the AFM investigations of the samples took place within 24 hours after the adsorption to assure the proteins' stability.

3.4   Characterization Techniques

Characterization of synthesized ta-C layers is rather challenging due to their electronic properties. With increasing sp^3 content, the conductivity of the layer decreases. Consequently, characterization techniques that are based on electron interactions with the substrate, such as transmission electron microscopy (TEM) or scanning electron microscopy (SEM), are not unrestrictedly suitable as they cause charging of the samples. Raman spectroscopy for instance offers a way to investigate ta-C optically. For this purpose, a laser beam is focused on the surface of the layer. The photons are inelastically scattered within the substrate and afterwards collected by a detector (e.g. CCD camera). The energetic loss originates from vibrations, rotations or phonons which are characteristic for each bonding-type and -partners. Hence, an analysis of the samples' structural properties is possible.

The Raman measurements presented in this work were mostly performed at the Institute of Physical Chemistry in close cooperation with Marcel Wille [Wil11], with the help of Stephan Stöckel and Dr. Nicolae Tarcea. Excitation in the visible (VIS) range was done with the 532 nm line of a Nd:YAG laser (Coherent, Inc.). The laser power amounts to 2 mW that is focussed on a diameter of approximately 1 μm. The spectral resolution did not exceed 7 cm^{-1}. For ultraviolet (UV) Raman spectroscopy, excitation was done with the frequency doubled emission of the 488 nm argon laser (Innova 300C MotorFred by Coherent, Inc.) resulting in a 244 nm line that offers a resolution of 5 cm^{-1}. In both cases (VIS and UV), the scattered light was analyzed with a LabRam HR 800 spectrometer (HORIBA Jobin Yvon GmbH) and the spectra were taken with a CCD camera (Symphony by HORIBA Jobin Yvon GmbH).

Another possibility to gather information on ta-C is using X-rays as interacting probe. The highly energetic photons penetrate through the surface into the material. Usually, the energy is sufficient to enable the excited core level electrons to overcome work function and leave the material with a kinetic energy that is characteristic for each bonding-type

and -partner. The electrons are collected and analyzed by a energy-separating spectrometer. X-ray photoelectron spectroscopy (XPS) has been performed using a Quantum 2000 (PHI Co., Chanhassen, MN, USA) spectrometer with a focused monochromatic Al K-alpha source (1486.7eV) for excitation. Detection was carried out 45° to the surface normal. This was done in close cooperation with Ralf Wagner and Mike Mühlstädt of the Institute of Materials Science and Technology (IMT, FSU Jena). XPS is rather surface sensitive as the range of the emitted electrons is too little in order to be detected when they originate from deeper than 10 nm underneath the surface. Because the upper monolayers of every ta-C layer are expected to contain a higher sp^2 content (because of the deposition process) than the bulk of the film, [Dav98, Rob93, Rob94] there will be always an underestimation of the average sp^3 content.

Contact angle measurements (CAM) have been conducted with a DSA10 drop shape analysis system (Krüss GmbH, Hamburg, Germany) to check for a possible change of hydrophilicity. For this purpose, a 5 - 8 μl droplet of Millipore water was carefully put on the sample. The ultrapure Millipore water has a resistance of 18.2 MΩcm at 25 °C and a total organic carbon (TOC) content of less than 10 ppb. A laterally installed camera is focused on the resulting profile. By approximating the droplet's surface by a sphere, the contact angle between droplet and sample can be determined. These measurements were performed at the Institute for Materials Science and Technology (IMT, FSU Jena) in cooperation with Dr. Thomas Keller and Christian Helbing.

For the investigation of the surface's morphology and the adsorption behavior of soft matter on ta-C, a non-destructive, extremely surface-sensitive technique was required. Atomic force microscopy (AFM) was used since energetic radiation, vacuum conditions, and charging would cause serious damage to the proteins. An atomically sharp vibrating tip scans the area of interest. A laser spot is focused on the back of the tip-holder (the cantilever) and reflected on a photo detector. When approaching the surface, the tip's vibration frequency alters, because of attracting or repelling forces such as Van der Waals. This change is detected by the laser reflection and directly plotted, resulting in the amplitude picture. The resulting phase shift is depicted in the phase image. A feedback loop processes the vibrational changes and adjusts the position of the sample in z direction to keep the tip's frequency constant, which can only be realized by adjusting the distance between surface and tip. This in turn is done by a piezoelectric scanner assuring an accuracy of tens of nanometers. The height picture reflects the piezo's movement and

consequently the desired morphological information. The AFM results presented in this work were obtained with a MultiMode AFM by Digital Instruments (Digital Instruments, Santa Barbara, CA, USA) that runs with a Nanoscope IIIa controller and a piezoelectric E Scanner. The latter allows a maximum scan size of 12 μm and a vertical resolution in the subnanometer range. Usually, a Micro Cantilever AC 160TC by Atomic Force that provides a tetrahedral Si tip with a radius of less than 7 nm was used. Moreover, the cantilever is single-side coated with an Al-reflex coating. The referring resonance frequency ranges from 314.5 to 334 kHz and the spring constant varies between 48.9 and 88.8 Nm^{-1}.

4 Ion Beam Modification of Surfaces and their Properties

In this chapter, results will be presented concerning the mass-separated ion beam deposition process of ta-C with the focus on the carbon ions' energy and the resulting sp^3 content. Therefore, according experiments were simulated and subsequently implemented. Afterwards, the synthesized layers were investigated by Raman, AFM, XPS and SEM regarding their roughness, 'diamond-likeness' and film thickness. The Raman and SEM characterization was done in close cooperation with Marcel Wille [Wil11] within the context of his bachelor thesis. Some Raman measurements were carried out during a research visit at the University of Pretoria, South Africa, in collaboration with Dr. Linda Prinsloo.

Ion beam-induced ripples were created on Si and TiO_2. Moreover, tetrahedral amorphous carbon ripples were created by coverage of silicon ripples with a suitable ta-C layer. The influence of the topographical changes on the interface's properties were investigated by XPS, AFM and contact angle measurements. This was done in close cooperation with Stefanie Eckner (bachelor thesis) [Kos11], Jessica Richter (diploma thesis) [Hön10], Maria Fravventura (master thesis) [Fra09] and Alexander von Müller (master thesis) [vM14].

4.1 Mass-Separated Ion Beam Deposition of ta-C

4.1.1 Ion Energy

As discussed in chapter 2.2.1, it is possible to tune the sp^3 content of the ta-C layers when knowing the ions' energy. Therefore, thorough consideration was given to the C^{12} ions' energy *before* they enter the deposition chamber, where they are decelerated to their desired deposition energy. The setup and chosen parameters of the Penning source that was explained earlier (compare with chapter 3.1) determine the ions' initial energy. When the ions enter the deposition chamber, the geometry and potentials of the deceleration unit mainly effect their deposition energy. In Figure 4.1, a sketch presents the deposition chamber's construction as cross section. The ion beam approaches the chamber from the left. Close to the chamber's entrance, an electron lens deflects the secondary electrons from the beam line's walls back into the beam line. Before the ions reach the deposition

chamber, they have an energy of about 30 keV, depending on the initial energy. Because the inner chamber is on the same positive potential (30 kV) as the source, the ions are decelerated. The applied voltage on the sample holder U_s defines their final deposition energy. A broadening of the ion beam is mainly accomplished by another lens, which also serves as barrier potential wall for the secondary electrons and sputtered atoms from the sample. By electrostatically pushing secondary electrons back into the sample, a reliable ion current measurement directly on the sample is possible.
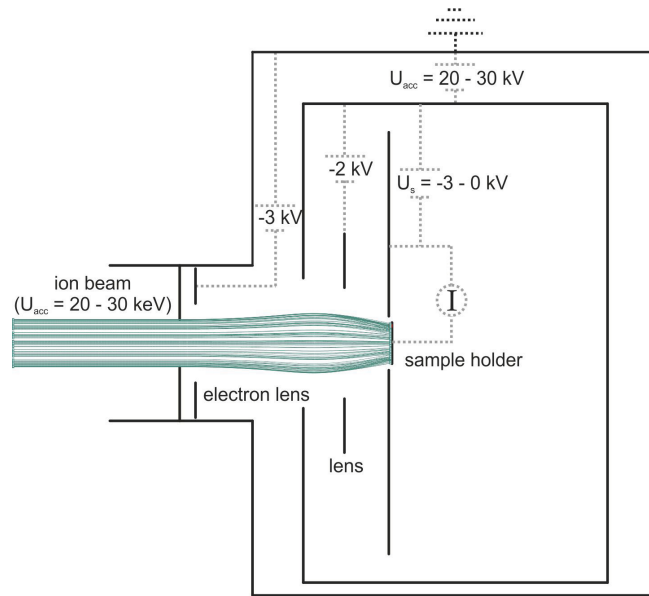
Figure 4.1: *Sketch of the setup within the deposition chamber. The ions (their trajectories taken from the simulation program SIMION are illustrated in cyan) are decelerated down to the desired deposition energy by applying the referring voltage to the sample holder, in respect to the high tension of the acceleration. An electron lens inhibits secondary electrons from the beam line to enter. The defocusing lens broadens the ion beam and suppresses secondary electrons originating from the sample what assures an accurate current measurement on the sample.*

A simulation of the deposition chamber and the electrostatic potentials allows a better understanding of the ion trajectories, which is necessary to optimize the deposition parameters. SIMION-8.0 is a simulation program that calculates potential arrays and resulting ion trajectories by solving the Laplace equation for the potentials that are specified by the user. [Man08] The user must first construct the geometry of the involved devices such as lenses, diaphragms, or deflection plates and assign a potential. Thereby, the user sets the boundary conditions for the solution of the Laplace equation. Additionally, the characteristics of the ion beam have to be defined. That includes next to particle number, mass, charge etc. also the ions' initial energy and their distribution. Attention to precision will

assure the correctness of the simulation. Hence, it is inevitable to determine the energy, the ions have after leaving the ion source.

For this purpose, Holger Stillrich [Sti03] developed a technique within the framework of his diploma thesis. As shown in Figure 4.2a, a cylindrical capacitor is directly installed into the deposition chamber. Both capacitor plates are individually connected to power supplies with a maximum voltage of ± 900 V. The ions (see marking in Figure 4.2a) can only hit the target and consequently be measured as a current, when the electrostatic force F_C equals the centripetal force F_Z. The ions' mass m and their velocity v contribute to their kinetic energy E_{kin}. Considering the radius r of the ions' trajectories within the capacitor, it is possible to calculate the electric field $E(r)$ the ions experience within the capacitor, assuming the ions' charge q is known:

$$F_z = \frac{m \cdot v^2}{r} = \frac{2 \cdot E_{kin}}{r} \overset{!}{=} q \cdot E(r) = F_C. \tag{4.1}$$

The capacitor's potential U_{cap} corresponds to the difference in voltage that is applied to each plate and can be gained by integration over the space between the two plates that have the radius R_2, respectively R_1. Due to the cylindrical geometry, the electric field within the capacitor correlates with r^{-1}. Integration reveals the dependency of the electric field on the capacitor's potential U_{cap} and its geometry:

$$U_{cap} = \int_{R_1}^{R_2} E(r) dr = \int_{R_1}^{R_2} E_0 \cdot \frac{1}{r} dr = E_0 \cdot \ln\left(\frac{R_2}{R_1}\right)$$
$$\curvearrowright E(r) = E_0 \cdot \frac{1}{r} = U_{cap} \cdot \ln\left(\frac{R_2}{R_1}\right) \cdot \frac{1}{r}. \tag{4.2}$$

The construction of the capacitor is such that the radii of the plates relate like Euler's number, so

$$\ln\left(\frac{R_2}{R_1}\right) = \ln\left(\frac{5cm}{1.84cm}\right) = 1. \tag{4.3}$$

Considering this and the assumption made in 5.1, equation 4.2 can be simplified to

$$U_{cap} = \frac{2 \cdot E_{kin}}{q}. \tag{4.4}$$

Apparently, the ions' energy corresponds to half the capacitor's voltage for $q = 1$. A sim-

ulation of the cylindrical capacitor was done to obtain an estimation of the carbon ions'
trajectories within the resulting electric field. Figure 4.2b shows a cross section of the
simulated cylindrical capacitor within the deposition chamber. In black, the ion trajectories are visible. Figure 4.2c shows three-dimensionally the resulting potential array, which
emphasizes its influence on the carbon ions' pathways. The ions' energy distribution was
assumed to be Gaussian with a maximum at 325 eV and a FWHM of 10 eV. A voltage of
± 300 V was applied to the respecting plates. The simulation was done for 1000 carbon
ions. A tenfold repetition of the simulation showed that all ions hit the target and did
not impacted elsewhere within the capacitor for the chosen parameters. The simulation
is very sensitive to slight variations of the involved geometries and ion beam properties
such as beam radius or angle. Hence, small deviations like the fact that the ion's initial
energy does not perfectly match half the capacitor's voltage can be expected.
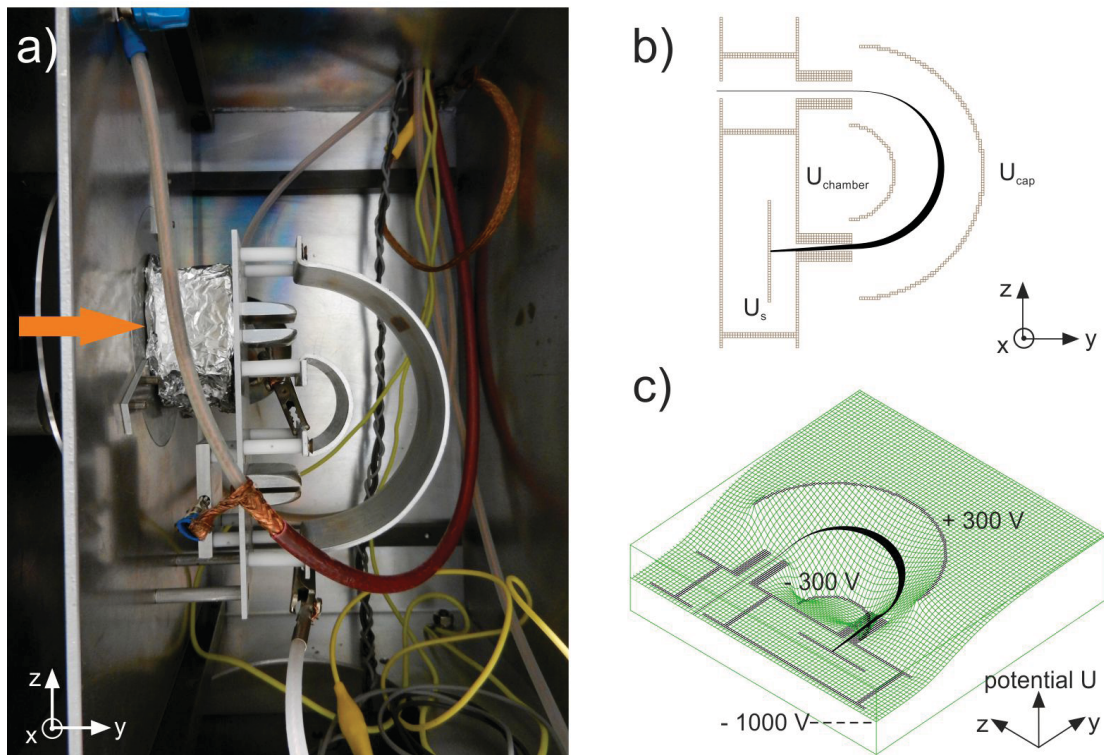
Figure 4.2: *a) Photo of the cylindrical capacitor that was installed into the deposition chamber. The ions enter the capacitor from the -y direction (arrow). b) SIMION simulation of the capacitor within the deposition chamber. The ion trajectories are shown in black. For the shown simulation, an ion energy of 325 eV and a capacitor potential of 600 V was set. c) 3D-illustration of the potentials that result from the simulation shown in b).*

Summarising, the ions' initial energy is measurable by variation of the capacitor's potential. This was done for applied sample voltages between 200 and 1000 V in steps of
100 V, for which the distributions in Figure 4.3a were obtained. Obviously, the ions' en-

ergy distribution is nearly Gaussian with a relatively small width. The current increases with increasing ion energy, which is in good agreement with the general consideration that more ions are attracted by a higher potential otherwise less ions are lost. Note that the increase of the current's amplitude is not perfectly homogeneous. This can be caused by slight variations of the ion current that is extracted from the source. The obtained curve of the ion current for the highest post acceleration (1000 V) shows the strongest inhomogeneity. This might be due to the limit of the power supply being reached. For all applied sample voltages, the maximum ion currents were in the range of nA, whereas the ion current directly in front of the deposition chamber was in the range of some ten μA. This deviation is explainable by the very small entrance slit of the capacitor and the possibility that the ions' energy distribution is originally broader but could not be resolved due to the limitations of the experiment's setup. Consequently, many ions did not hit the target. The curves were fitted, using a Gaussian distribution. The maxima x_c were plotted over the referring applied sample voltages and the respective FWHM was assumed to represent the variations of the maxima. Following the assumptions in [Sti03] and as shown above, the ions' initial energy can be gained by extrapolating the linear fit to $U_S = 0V$ that is shown in Figure 4.3b.
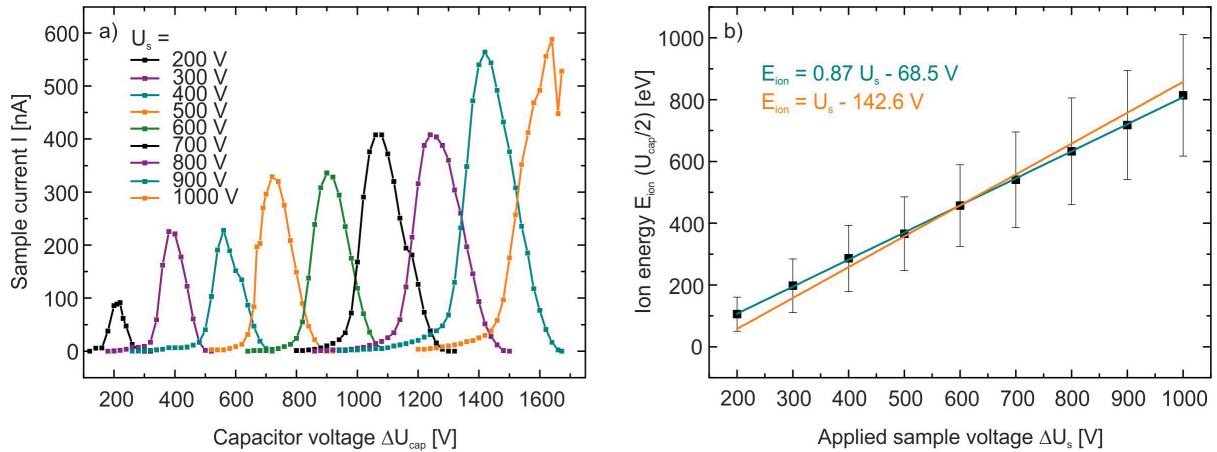
Figure 4.3: *a) Ion current (I) measurements for varied capacitor voltages (ΔU_{cond}). The applied sample voltages (U_{acc}) was set to a fixed voltage between 200 and 1000 V in steps of 100 V. b)Dependency of the ions' energy (E_{ion} that corresponds to $\frac{U_{cap}}{2}$) on the applied sample voltage (U_{acc}). The linear correlation is emphasized by a suitable fit (cyan), according to which the ions' initial energy is about (68.5 ± 2.1) eV. The orange line represents a linear fit with a slope of one resulting in an ion energy of (142.6 ± 2.9) eV.*

Apparently, the ions' initial energy is about (68.5 ± 2.1) eV. Note that the error bars increase with increasing post acceleration. This seems reliable as more ions of different

energies can reach the sample holder when applying higher voltages. Obviously, the best fit (cyan) does not have a slope of one as one would expect. A possible reason is the following: before entering the deposition chamber, the ions have not enough energy to overcome the chamber's potential. When applying a small negative voltage (relative to the accelerator voltage) to the sample holder, only high energetic ions hit the target. Hence, part of the ions' initial Gaussian energy distribution is cut off. An increase of the post acceleration voltage enables also slower ions to contribute to the current measurement. Thus, a bigger part of the initial energy distribution adds to the final energy distribution shifting the centroid with respect to the maximum. In addition, the geometry of the capacitor is also error-prone. Inhomogeneities in the shape can cause perturbations of the electric field between the capacitor plates and influence the ions' trajectories. This influence can be roughly estimated. The relative error of the capacitor voltage is 0.5 %. Assuming a measurement error of 1 mm for the radii of the capacitor's plates, the ion energy has a relative error of ≈ 8 %. Setting the slope of the fit to one and recalculating the fit (orange) gives an initial ion energy of (142.6 ± 2.9) eV. However, more important than the ions' initial energy is the ions' energy distribution. Assuming, that the latter equals the FWHMs of the Gaussian Fits in Figure 4.3b, the distribution ranges from 55 to 197 eV, depending on the applied capacitor voltage.

Due to the general setup and operating mode of a Penning ion source, it can be expected that parameters such as the applied voltage between anode and cathode within the source and the current of the source-surrounding magnet influence the ions' energy since they ought to have an impact on the created plasma from which the ions are extracted. In order to evaluate the influence of these parameters on the ion energy distribution, the values for the source voltage and the magnet current were varied in a range that comprises typical values that were applied for this work. As seen in Figure 4.4a and 4.4b the source magnet current was chosen between 1.4 and 2.0 A and the source voltage was varied between 1.6 to 2.4 kV. For these measurements, the applied sample voltage was always set to 900 V assuring a high enough final ion current within the deposition chamber and the possibility to investigate the peak in it's full width, as can be seen in Figure 4.4. The source magnet current has some effect on the ions' initial energy, which causes a shift (arrow) of the maximum sample current concerning the applied capacitor voltage of about 90 V. This indicates that the ions initial energy can vary about 45 eV, depending on the chosen source magnet current. The FWHM and thus the width of the ion energy distribution

broadens about 40 V (20 eV) with increasing source magnet current. The influence of the source on the ions' initial energy is less when investigating the source voltage. Here, the shift (arrow) is only about 30 V, which corresponds to a shift in energy about 15 eV. Interestingly, the ion energy distribution gets smaller as the FWHM is decreased about 20 V (10 eV). Consequently, a small source magnet current and a high source voltage are useful in order to obtain a small energy distribution.
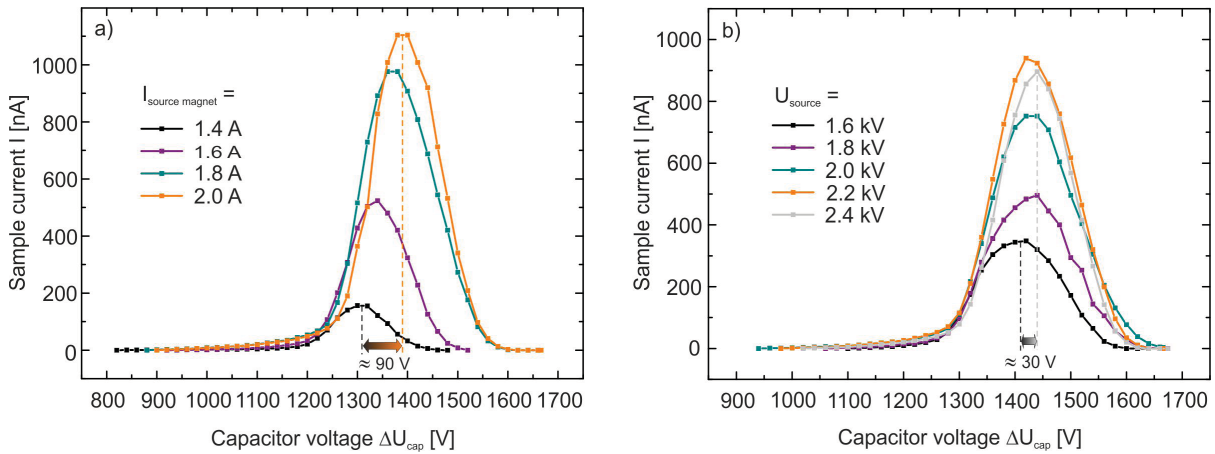

Figure 4.4: *Ion current measurements for a) varied source magnet currents and b) varied source voltages. In both cases the sample voltage was set to 900 V.*

Finally, a close look was taken on the source geometry's influence on the ions' energy by choosing anodes with different lengths. Anode "7" had a length of 39 mm whereas anode "0" was 41 mm long. Instead of using the cylindrical capacitor, the ion current was measured directly on the usual sample holder for this experiment as a function of the sample voltage U_{acc}. The results are presented in Figure 4.5a. Obviously, both sources differ in their ion current. From anode "7" about 30% more ions can be extracted than from anode "0", however, the characteristics of the ion current measurement for both anodes are the same. At low voltages, the ion energy is not high enough to enable the ions (which then only have the energy they obtained during generation in the source) to overcome the deceleration potential of 30 kV. At a certain point the sample voltage is sufficient and the ion current increases strongly. When the sample voltage is even higher, all ions can reach the sample holder. This results in a saturation of the current. Note, significant points on the abscissa vary for both anodes. This is more apparent when considering the first derivative (see Figure 4.5b). As can be learned from the referring maxima±FWHMs, the majority of the ions has an initial energy of (107.9 ± 45.4) eV (anode "7"), respectively (193.3 ± 32.3) eV (anode "0"). Considering the above, anode "7" seems most favorable

when interested in a higher ion output. Anode "0" should be preferred when a small ion energy distribution is desired. Depending on which ion source anode is chosen, a post acceleration of about 100, respectively 200 V has to be applied to obtain ions with a deposition energy of 100 eV, which is in the range of the results that were received from the experiments with the cylindrical capacitor.
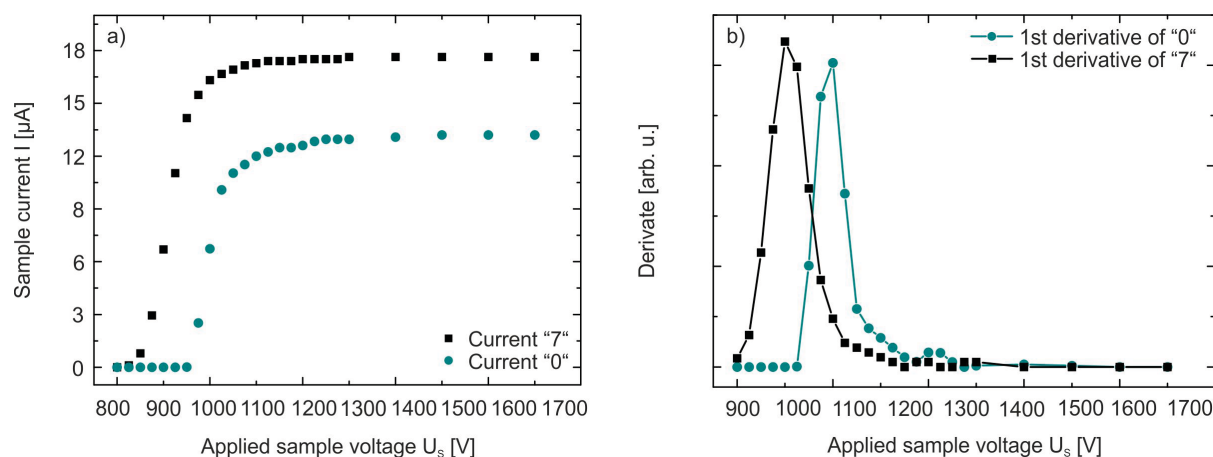

Figure 4.5: *a) Ion current measurements for different source anodes. b) First derivative of the current measurements.*

In conclusion, the ions' initial energy was determined using two different techniques. The first includes use of a cylindrical capacitor, whereas the second does not require any changes in the setup. Both techniques come to the same result concerning the ions' initial energy, which can be assumed to be about 100-200 eV. Results can vary because the exact condition within the source can differ due to the diversity of parameters being significant. To assure reproducibility, the maximum of the first derivative is searched for at the beginning of every deposition process. When the referring voltage is determined, the required acceleration is added to obtain the desired deposition energy. This technique is used in the following experiments as it is effective and easily practicable.

4.1.2 Synthesis and Characterization of ta-C Thin Films

All ta-C samples were grown on top of n-type Si substrates, as Si properties are thoroughly investigated; conductive if doped, easily affordable and sufficiently smooth for the subsequent biological experiments. The Si substrates were cleaned with ethanol and subsequently dried with compressed air. An additional sputter step with argon ions was done prior to the deposition process to assure the substrate was free of any contaminations. These Ar ions had an energy of about 3 keV and a total ion fluency of $5 \cdot 10^{15} cm^{-2}$ was

applied. TRIM[1] calculations showed that this fluency is enough to sputter off at least two monolayers of silicon. Argon was chosen because being a noble gas minimizes any possible incorporation. The actual carbon deposition process followed directly after the sputtering without breaking vacuum. Usually, the necessary deposition parameters were chosen in a way to center the ion beam spot on the substrate first and than to widen it, before the beam was swept over the sample. Sweeping was done to achieve a homogeneous coverage of the sample. Moreover, it is possible to tune the thickness of the ta-C layer by varying the integrated charge of the carbon ions on the silicon substrate. A set of ta-C layers made of different carbon charges ranging from 60 to 476 mC/cm^2 (corresponds to 100 to 800 mC on the entire sample area) was assembled. The typical ion current on the sample was about 6 μA/cm^{-2}. Thus, the deposition time ranged between 3 - 21 h.

The **film thickness** was investigated in order to determine the minimum amount of deposited ions for a workable layer thickness for the bioexperiments. The grown ta-C samples were covered with approximately 10 nm gold and broken afterwards. The cross section was investigated by a high-resolution scanning electron microscopy (SEM). The SEM operated with electron energies of 2 - 5 kV and the electron current was set to 86 pA. One representative SEM micrograph can be seen in Figure 4.6a. The strong contrast between the single layers of Si/Si-C/ta-C/Au made it possible to define the boundaries of the ta-C layers (blue markings), in order to determine its thickness. The purple markings illustrate the area of densification and Si/C mixing, that takes place in the early stages of film growth. According to the suplantation model, the first impinging carbon ions only form a dense Si-C interface layer. A certain fluence is necessary for this interface to be saturated before a pure ta-C film grows. Table 4.1 contains the deposited charges, the referring ion fluencies and the resulting ta-C film thickness and the referring errors, which originate from multiple thickness measurements per taken SEM image. Note, the values for the charges (100 - 800 mC) above referred to the absolute charges deposited on the entire sample area. The standard sample size was (1.2 x 1.4) cm^2. Of course, special care was taken about the homogeneity of the ta-C layers. Nevertheless, slight variations of the film thickness over the sample can not be excluded. Figure 4.6b illustrates the correlation between deposited charge and obtained film thickness. As expected, the dependency has a linear character. The interception point of the fit with the abscissa is slightly positive as the first ions only cause a densification of the film. A charge of at least

---

[1]www.srim.org

$\approx$ 30 mC/sample area ($\approx 1.1 \cdot 10^{17} cm^{-2}$) is necessary in order to achieve a measurable film thickness.

Table 4.1: *Dependency of the ta-C layer thickness on the deposited carbon charge, respectively the deposited ion fluency.*

charge/sample area [mC]	fluency [$\cdot 10^{18}$ cm^{-2}]	thickness [nm]
100	0.37	15 ± 2
200	0.74	52 ± 5
300	1.11	77 ± 3
400	1.49	95 ± 12
600	2.23	134 ± 5
800	2.97	194 ± 21
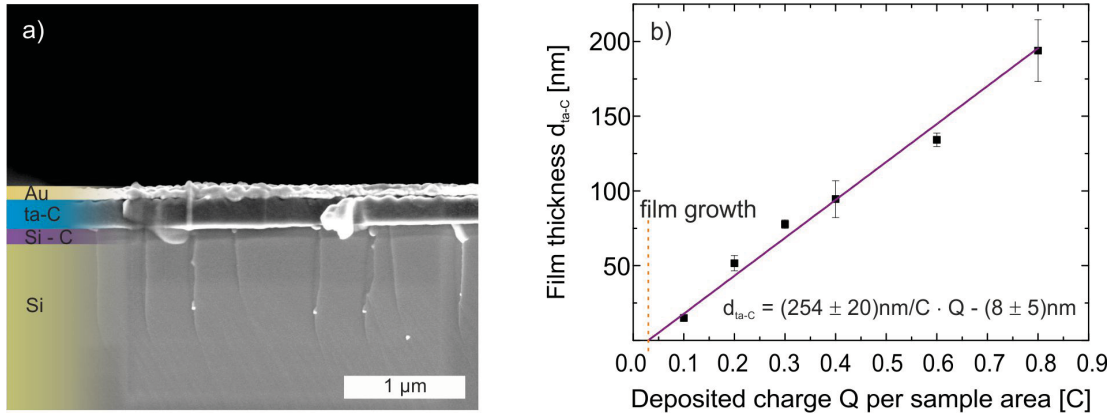
Figure 4.6: *a) SEM picture of the cross section of the Si/Si-C/ta-C/Au interface. The blue markings illustrate the ta-C layer which has a thickness of 194 $\pm$ 21 nm. b) Correlation of the layer thickness and the deposited charge on a standard sample area of (1.2 x 1.4) cm^2.*

The findings above show that a deposited fluence of $7.4 \cdot 10^{17} cm^{-2}$ is sufficient to obtain a $\approx$ 50 nm thick ta-C layer. This makes it possible to obtain a layer thickness that can be produced in a reasonable amount of time (6-8h) using an ion flux of about 6 μA/cm^{-2}, which is also sufficient for the subsequent biological experiments.

Although knowing the film thickness of our samples is important, the most crucial property of the ta-C layers is their **sp^3 content**. As was discussed in chapter 2.1.2, determining the sp^3 content is anything but easy and unambiguous. Within this work, XPS was used to determine the sp^3 content. A set of ta-C layers was synthesized with different deposition energies, ranging from 100 to 1100 eV. The charge of carbon ions that were deposited on the entire sample area was about 200 mC, which equals roughly $7.4 \cdot 10^{17} cm^{-2}$ and a film thickness of $\approx$ 50 nm. Additionally, highly ordered pyrolytic graphite (HOPG) with a sp^2 hybridized carbon network was investigated via XPS as comparison to the ta-C layers. A survey spectrum was taken of all samples, of which examples are shown for HOPG (a) and

for one ta-C layer (b) in Figure 4.7. The C 1s peaks that is characteristic for a carbon-based sample is clearly dominant around a binding energy of 284 eV. [Mou92,Yam10] The survey spectra also show peaks around 531 eV and 23 eV that can be assigned to O 1s and O 2s, respectively. [Mou92] Additional peaks are visible at 99.5 eV and 160 eV, representing the binding energies of Si 2p and Si 2s electrons. Those peaks apparently originate from surface contaminations, as the same peaks disappear in the HOPG spectra (see inset of Figure 4.7a) *after* re-cleaning. Although these peaks appear in the ta-C spectra, the correlation with the Si substrate can be excluded because their intensities equal the ones of the unclean HOPG. Moreover, it is impossible to measure a Si related signal through a 50 nm thick ta-C layer. It is more likely that these silicon peaks originate from surface contaminations, as the samples were split after the deposition process. Thus, some silicon particles from the substrate might be scattered over the ta-C surface.
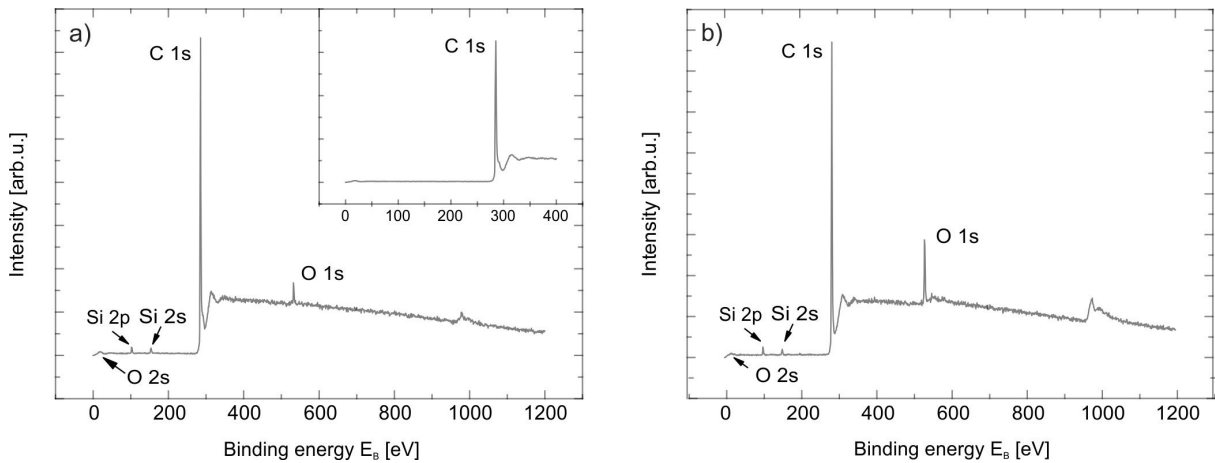
Figure 4.7: *XPS survey spectra of a) HOPG and b) ta-C. The inset of a) shows the enlarged XPS spectrum for small binding energies of a freshly cleaned HOPG sample. The characteristic peaks for C 1s, O 1s, O 2s, Si 2s and Si 2p are marked. Obviously, the Si peaks originate from surface contaminations, as they disappear after cleaning (see inset).*

Studies by Díaz et al. [Día96] and Mérel et al. [Mér98] showed that the sp^3 content can be determined by fitting the C 1s peak assuming its amplitude is a superposition of carbon related lines. Figure 4.8a shows a fit of the strictly sp^2 bound HOPG at 284.4 eV. In case of ta-C, the C 1s peak broadens as demonstrated in Figure 4.8b. A comparison of the referring areas underneath the fit enables the determination of the sp^3 content; however, the choice of the fitting parameters allow a rather subjective range. At the beginning, the Shirley background was subtracted from the measured data. The Shirley background includes a proportional correlation of binding energy and peak intensity. [Shi72] Considering the studies by Díaz [Día96], Mérel [Mér98] and Yamamoto [Yam10], the centers of the sp^2

and sp^3 related lines were set to 284.4 eV and 285.5 eV, respectively. For the fitting of the obtained spectra, the aim was to keep the full width half maximum (FWHM) as small as possible (close to 1 eV). It is also clear from the spectra that there is a third line. This line could have its origin in a C-O bonding that occurs at the surface. According to literature, the referring binding energy varies between 288.2 and 289.6 eV [Boy95, Bha98, Fu05] and thus fits to the measured spectra.
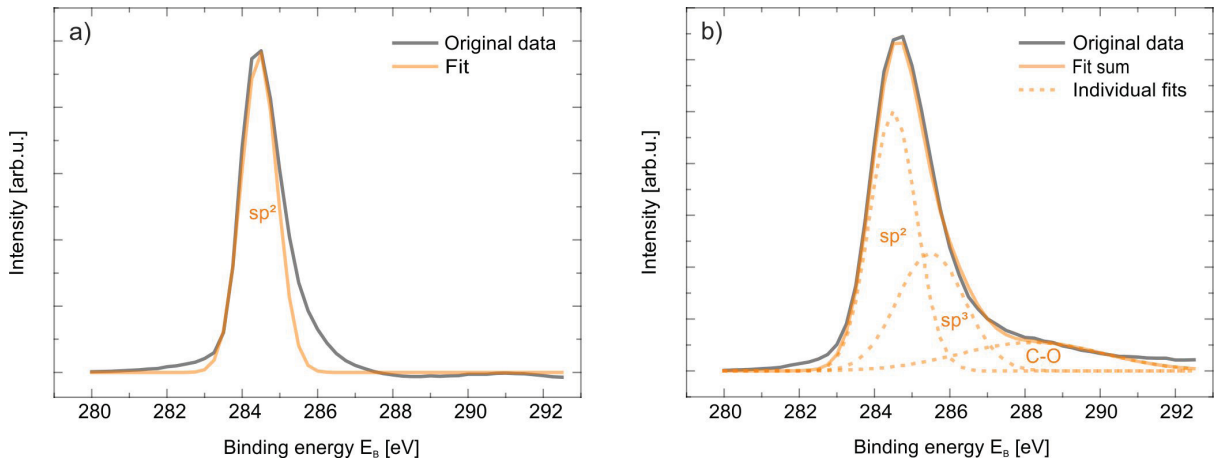

Figure 4.8: *XPS analysis of HOPG (a) and a ta-C layer (b) around the C 1s peak. For HOPG, which is strictly sp^2 bound, the referring fit centers around 284.4 eV. In case of ta-C three peaks can be fitted at 284.4 eV (sp^2 related), 285.5 eV (sp^3 related) and 288.3 eV (C-O related). By comparison of the sp^2 and sp^3 related areas underneath the referring fits, the sp^3 content can be determined.*

Notably, XPS is rather surface sensitive. The average sp^3 content within the film is likely to be higher than the measured one. This assumption is based on the fact that the upper carbon layers are sp^2 rich due to the growth mechanism. [Dav98, Rob93, Rob93] An overview of the investigated samples is given in Table 4.2 The deposition energies are compared with the expected sp^3 content (in reference to Figure 2.3) and the one that resulted from the XPS analysis. Another reason why the determined sp^3 content is some percent less than the expected one [Ron97] is the uncertainty of the deposition energy and the sp^3 content that can be expected. As was shown in chapter 3.1.1, the range of the ions' energy is broad. In addition, the correlation of the sp^3 content dependency on the ion energy in Figure 2.3 that was the base for the actually chosen ion energies is imprecise. The same sp^3 content can be achieved by applying a broad range of energies. These uncertainties clearly add to the inaccuracies in Table 4.2.

Table 4.2: *Results of the XPS analysis for* sp^3 *content determination of ta-C films. The deposition energies and their referring expected* sp^3 *contents were compared with the* sp^3 *content that was determined by evaluating the C 1s peak.*

sample	E_{ion} [eV]	expected sp^3 [Ron97] [%]	determined sp^3 [%]
HOPG	/	0	0
S121217 12C1100 Si	1150 ± 45	30 - 50	40 ± 20
S121211 12C550 Si	518 ± 45	50 - 70	67 ± 18
S130116 12C100 Si	280 ± 32	60 - 80	34 ± 9
S130108 12C100 Si	86 ± 32	70 - 80	36 ± 2

Another possibility to determine the sp^3 content is Raman spectroscopy, as was explained in chapter 2.1.2.

Raman measurements were performed in the VIS and UV spectra using a 532 nm and a 244 nm laser line, respectively. Figure 4.9 shows the spectra obtained for HOPG (a), ta-C layers with varied ion deposition energies (b) and polycrystalline diamond (c). The excitation line was in the VIS (532 nm). Relatively sharp peaks were obtained for HOPG and diamond at (1579.1 ± 16.3) cm^{-1} and (1330.9 ± 3.9) cm^{-1}, respectively. Note, these two spectra were measured at a different Raman setups. In case of the ta-C layers, a broad peek between 1200 and 1700 cm^{-1} appeared, originating from the two overlapping D (≈ 1400 cm^{-1}) and G (≈ 1580 cm^{-1}) modes. Additionally, peaks that can be related to Si were observed around 518 and 1035 cm^{-1}. The obtained data can be evaluated in a variety of ways because of the numerous methods presented in literature. Ferrari and Robertson, [Fer00] for instance, focus on the intensities' relation $\frac{I(D)}{I(G)}$ between the G and D peak, but according to Lifshitz, [Lif99] this techniques lacks the physical basis to determine the sp^3 content from it. Prawer et al. [Pra96] describe in their work the possibility to focus on the position of the G peak, as it correlates with the sp^2 content of the samples. Finally, one can fit a Breit-Wigner-Fano function, which is defined as:

$$I(\omega) = \frac{I_0 \left[\frac{2(\omega - \omega_0)}{q \cdot \Gamma} \right]^2}{1 + \left[\frac{2(\omega - \omega_0)}{\Gamma} \right]^2} + (a \cdot \omega + b), \tag{4.5}$$

on the rather broad peak between 1200 and 1700 cm^{-1}. I_0 corresponds to the height of the spectrum, Γ is its FWHM, ω_0 is the central position and q is its skewness factor. By determining the latter, it is possible to quantify the sp^3 content. According to works by several groups, [Pra96, Gil00, Fer00] the sp^3 content is higher, the more negative q is.
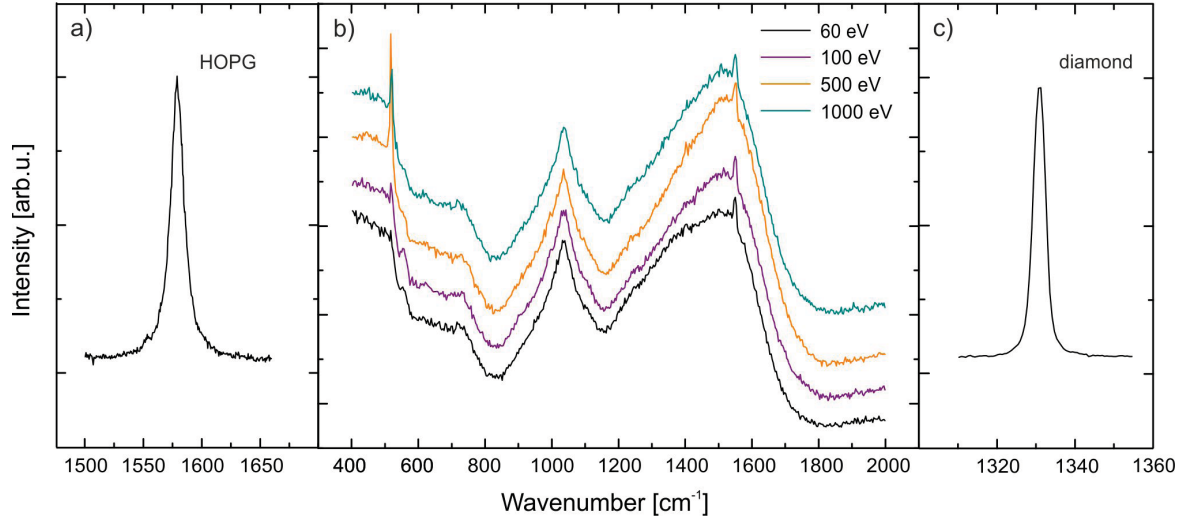
Figure 4.9: *Raman measurements of HOPG (a), ta-C layers that were synthesized with varied ion deposition energies (b) and polycrystalline diamond (c). The excitation line was in the VIS range (532 nm). The HOPG and diamond related peaks were found around 1580 cm^{-1} and 1331 cm^{-1}, respectively. For the ta-C layers a broad peak ranging from 1200 to 1700 cm^{-1} was observed.*

The evaluation of the referring q factors showed, that the highest sp^3 content of 60 - 80% was found for the samples that were synthesized with 100 and 500 eV carbon ions. Their q factor went below q $\approx$ -8. The sample produced with 60 eV ions had the lowest sp^3 content with 30 - 40% based on a q factor of q $\approx$ -4. For the sample that was synthesized with 1000 eV ions, a q factor of q $\approx$ -5.5 was determined, which equals a sp^3 content of 50-60%. These results are summarized in Table 4.3.

Table 4.3: *Determination of the sp^3 content of ta-C layers that were synthesized with varied ion energies via Raman spectroscopy. The excitation was in the VIS (532 nm).*

sample	E$_{ion}$ [eV]	expected sp^3 [%]	determined sp^3	q factor
S110620 12C1100 Si	1000 $\pm$ 45	30 - 50	50 - 60	- 5.5
S110616 12C550 Si	500 $\pm$ 45	50 - 70	60 - 80	- 8.0
S110615 12C100 Si	100 $\pm$ 32	60 - 80	60 - 80	- 8.0
S110614 12C100 Si	60 $\pm$ 32	70 - 80	30 - 40	- 4.2

Note, Raman measurements in the VIS only offer an indirect determination of the sp^3 contents as the applied energy is not sufficient to excite the C-C vibration of the sp^3 phase. [Gil97] Hence, similar investigations were carried out using a UV excitation line (244 nm). Theoretically, a direct determination of the sp^3 content would be possible as UV radiation is energetic enough for the required excitation. Unfortunately, the according T peak around 1100 cm^{-1} overlaps with the second order peak of silicon around 1050 cm^{-1}, that originates from the substrate. Therefore, the q factor was determined

again. The evaluation of the spectra (not shown here) showed that the highest sp^3 content was obtained for the ta-C layer that was synthesized with 500 eV carbon ions.

As mentioned in the introduction, ta-C layers are desired to have rather smooth surfaces. Studies by Lifshitz et al. [Lif96,Lif95] and Peng et al. [Pen01] indicate that the **surface roughness** strongly depends on the energy of the carbon ions. Interestingly, rough surfaces are expected to occur for small deposition energies (surface growth); whereas higher deposition energies cause rather smooth surfaces (subsurface growth). For this thesis, a surface roughness of less than 1 nm was favorable for the biological experiments. After the deposition of carbon ions with varied ion energies, the obtained ta-C samples were cleaned with compressed air and investigated via AFM directly after deposition. Figure 4.10a shows the height picture of a ta-C layer that was deposited with ≈100 eV carbon ions. A surface of carbon layers that results from ≈1150 eV carbon ions is shown in Figure 4.10b. By choosing the same scale for both AFM height pictures, it becomes very clear that the surface is much smoother for higher deposition energies, which is in agreement with Lifshitz et al. [Lif95]
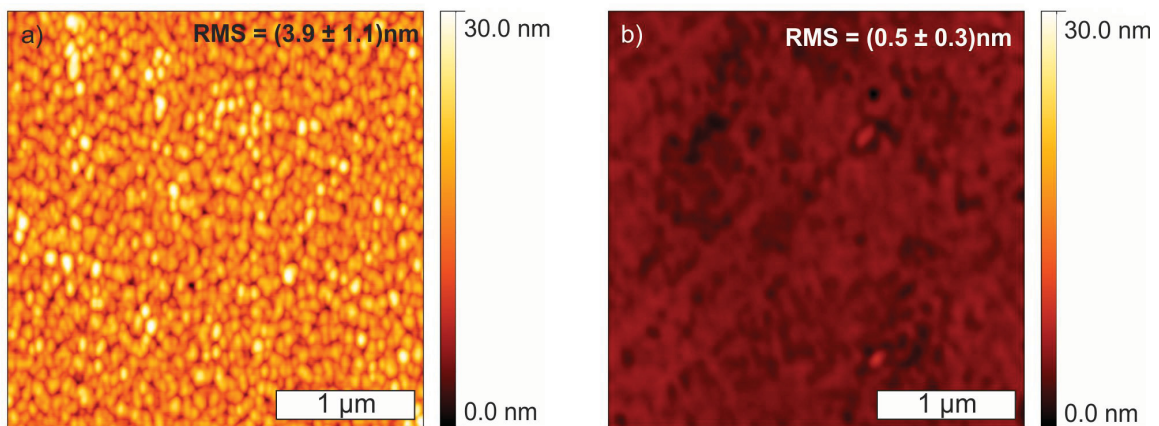
Figure 4.10: *AFM height pictures of a ta-C layers that were synthesized with a) less energetic carbon ions (around 100 eV) and b) more energetic ones (around 1150 eV). The scale was chosen to be the same to emphasize the differences in height.*

A set of samples with different deposition energies was investigated concerning their surface roughness RMS. The roughness was measured on at least three different positions on the sample surface. Each investigated spot had a scan size of (1x1) μm^2. The average roughness was calculated and its standard deviation was interpreted as error. Its dependency on the carbon ions' deposition energy is illustrated in Figure 4.11. The surface roughness decreases from almost 4 nm to less than 0.5 nm with increasing deposition en-

ergy. There is a threshold value of approximately 500 eV for which the surface roughness
falls below 1 nm. The roughness values saturate for higher ion energies, which can be
explained by solely subsurface growth.
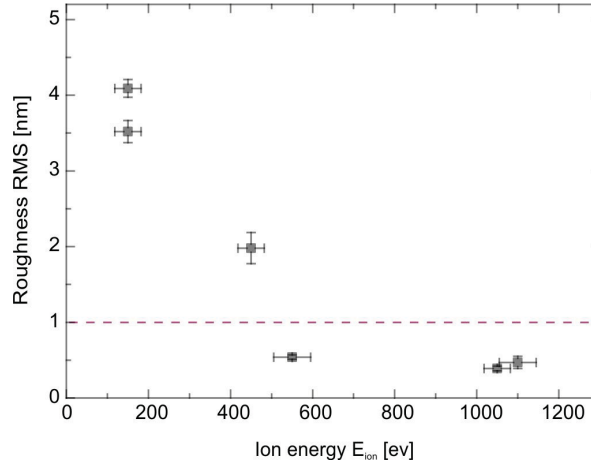
Figure 4.11: *Dependency of the surface roughness of deposited carbon films on the carbon ions'
deposition energy. Clearly, with increasing deposition energy, the surface roughness decreases.*

The focus of this section was on the influence of the deposition energy, as it has the
biggest impact on the ta-C properties. This is underlined by the investigation of the
films' sp^3 content and surface roughness. In conclusion, a layer synthesized with a carbon
ion energy of about 500 eV seems to be the best ta-C layer that can be obtained with the
ion accelerator Mr. Stringer as its sp^3 content is expected to exceed 70 % and its surface
is sufficiently smooth (less than 1nm). Moreover, a fluence of $7.4 \cdot 10^{17} cm^{-2}$ causes a film
thickness of about 50 nm assuring a workable ta-C nanolayer.

4.2   Formation of Rippled Surfaces Using Ion Beams

4.2.1   Ripples on Si and TiO$_2$

Rippled surfaces were created on rutile TiO$_2$ and Si using ion beam erosion for the purpose
of investigating the influence of the topography changes on a material's biocompatibility.
Both investigated materials were single crystalline and had a <100> orientation. The
samples were irradiated with xenon ions. Xenon ions were selected due to the fact that
they exclude any doping effects on the substrate. Usually, noble gas atoms do not form
bonds and mostly diffuse out rapidly after irradiation at room temperature. The referring
ion energies ranged from 5 - 20 keV, which enable to vary the wavelength of the created

ripples as explained in more detail in chapter 2.2.3. We used the low ion energy implanter LEILA for energies up to 10 keV and ROMEO for energies higher than 10 keV. Typically, ion fluences of 10^{16} ions/cm^2 (fluxes of 1 μA/cm^2) were applied and the angle between the surface and the incident ion beam was 70 - 72°. These parameters comply well with known values from literature to obtain ripples. [Zha09]

After the irradiation process, the samples were investigated via AFM. Figure 4.12 shows a height map (a) of a Si sample that was irradiated with an ion energy of 7 keV, under an incident ion angle of 70°. The ion fluence was 10^{16} ions/cm^2. A regular structure occurs with a preferential direction perpendicular to the applied ion beam. The black line marks the position of the cross section that is presented in b). Although the wavelength of the shown ripples is in the range of 50 nm, their amplitude does not exceed 4 nm. Hence, the ripple topography is relatively flat.
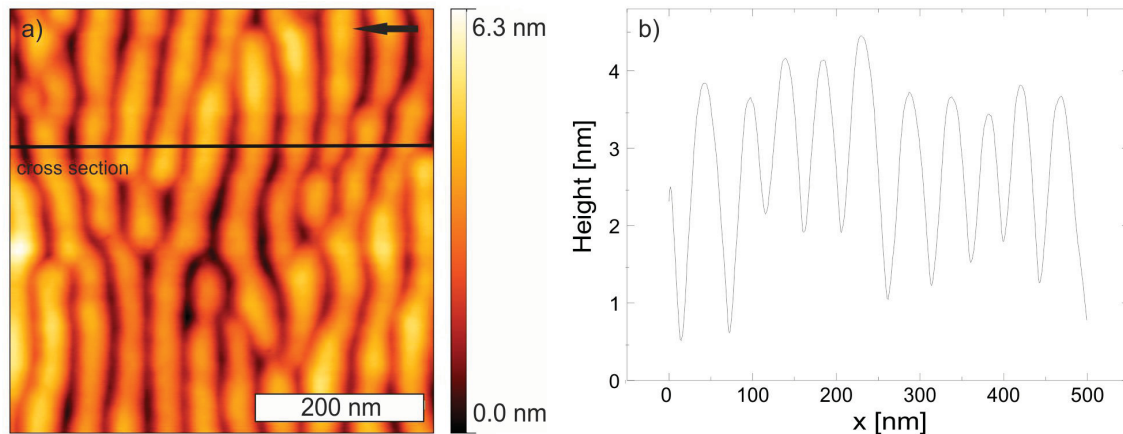
Figure 4.12: *AFM analysis of Si that was irradiated with 7 keV xenon ions under an incident ion angle of 70°. a) shows the hight picture with the position of the cross section that is to be seen in b). The arrow in a) indicates the ion beam direction.*

The wavelengths of all samples were determined by fast Fourier transformation (FFT) of the obtained height pictures and are plotted as a function of the ion energy in Figure 4.13. The according fits emphasize a power law dependency for Si and TiO$_2$: the ripple wavelength λ increases with increasing ion energy ϵ. Roughly, the dependency corresponds to $\lambda \sim \epsilon^{2m}$. An exponent m of 0.5 ± 0.05 could be obtained for the Si samples, as showed in Figure 4.13a. This result is well in agreement with experimental data obtained from irradiation of silicon with argon ions by Chini et al. [Chi09] For TiO$_2$, a value of 0.65 ± 0.15 was obtained for the exponent m. This value is above the generally assumed one of m = 0.3, but well within the boundaries of $0 \leq m \leq 1$. [Sig69] It is possible, that redeposition processes during the sputter process lead to a coarsening of the ripple wavelength

over irradiation time [Kel10, Yew05] and consequently cause the observed discrepancy.
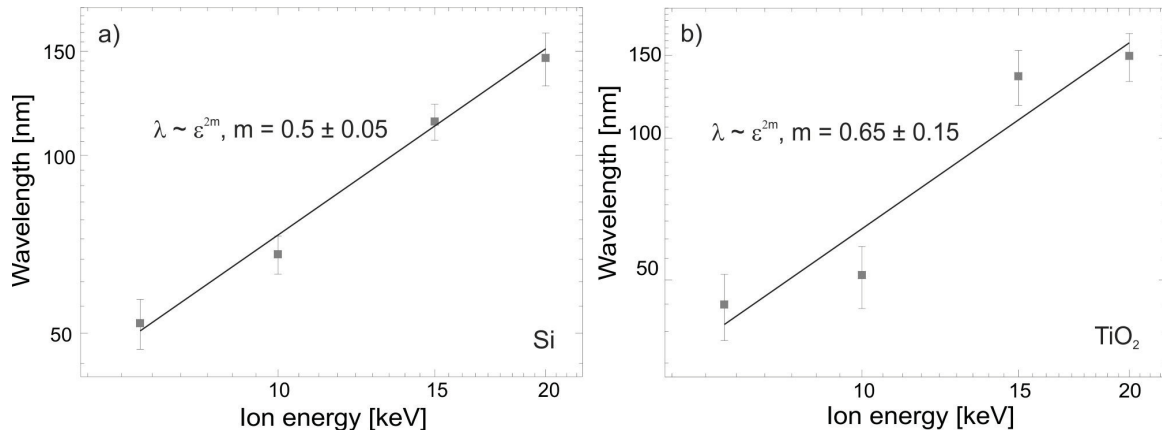
Figure 4.13: *Dependency of the obtained wavelengths on the applied ion energies for Si (a) and TiO$_2$ (b). For both substrates, the wavelengths increase considerably with increasing ion energy. The referring fits emphasize the power law dependency for which the according exponents m have been calculated.*

A 5 μl droplet of water was put onto the sample surfaces for contact angle measurements (CAM). The resulting contact angles between sample and droplet were investigated visually from the side by approximating the shape of the droplet by a sphere (see Appendix). The measured contact angles for rippled Si and TiO$_2$ surfaces are given in Figure 4.14 as a function of reciprocal wavelengths. For reference, contact angle measurements were also carried out for flat Si and TiO$_2$ samples that were irradiated perpendicularly to the surface. Those samples were also irradiated with xenon ions. The ions energy was 20 keV and the fluence was 5· 10^{16} cm^{-2}. This resulted only in an amorphization of the surface but no ripples were created. The results presented in Figure 4.14a reveal that compared to non-irradiated and flat Si, the contact angle increases only marginally from $(84.5 \pm 4.6)°$ to $(85.0 \pm 2.0)°$ for flat, irradiated Si. After changing the topography and thereby increasing the reciprocal wavelength of the created ripples, the contact angle decreases by about 25°. This decrease is ambiguous and merely a trend mostly within the range of error for the rippled Si substrates.

The contact angle θ slightly but not significantly increases from $(60.9 \pm 3.2)°$ to $(65.1 \pm 12.0)°$ after irradiation for flat TiO$_2$ surfaces (see Figure 4.14b). Structured TiO$_2$ samples with different reciprocal wavelengths show an increase of the contact angle, by about 25 - 30°, for high wavelengths (small reciprocal wavelength) indicating an influence of the surface curvature on the surface energy. However, the contact angles remain unchanged within the range of error for small wavelengths (high reciprocal wavelengths).

Therefore, a significant influence of the actual ripple wavelength on the surface chemistry can be excluded.
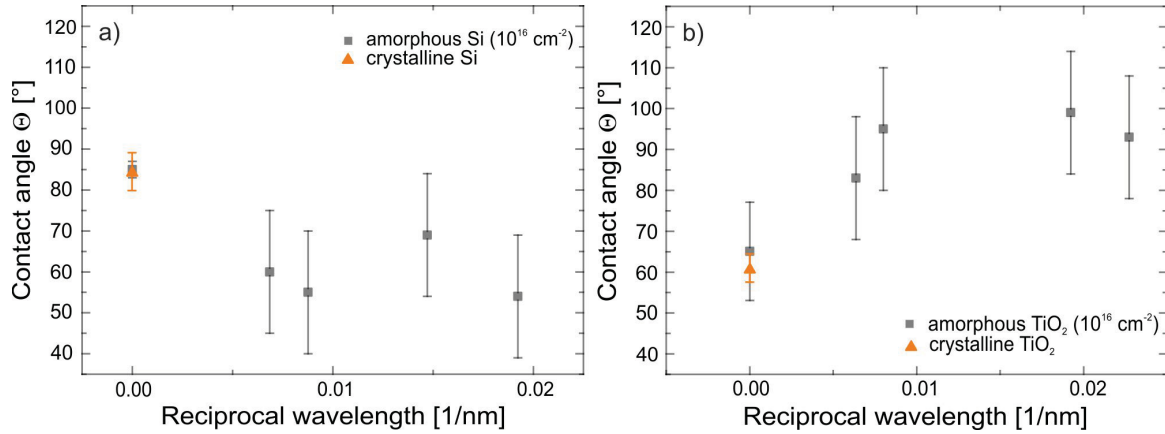
Figure 4.14: *Contact angle measurements for Si (a) and TiO_2 (b) samples. The substrates were either untreated and therefore flat and crystalline (orange triangles) or irradiated (squares). Depending on the angle between sample surface and ion beam, the samples were flat or a ripple structure was created that was equally amorphous. For both substrates, no change in the hydrophobicity can be found for flat samples independent on their structure (crystalline or amorphous). When introducing ripples, changes can be measured but are marginal, mostly within the range of error. No clear wavelength dependency can be seen.*

X-ray photoelectron spectroscopy (XPS) on both non- and xenon-irradiated TiO_2 and Si surfaces was performed to analyze possible stoichiometric changes due to the irradiation process. Note: for all peaks presented, the Shirley background was subtracted from the original data and a Gaussian fit was applied to the lines. The upper row of Figure 4.15 represents the results for the O 1s and the Si 2p peak of flat Si with a native SiO_2 layer before and after the irradiation process. Although the natural SiO_2 layer was sputtered away during ion beam bombardment, a new SiO_2 layer was formed immediately after the irradiation process when venting the implanter and the sample was transported to the XPS system.

The O 1s peak shown in Figure 4.15a is located at a binding energy of about 532.5 eV in case of non-irradiated Si. This correlates well with literature [Nef77]. The peak position shifts only negligibly ($\Delta E < 0.1$ eV) towards higher binding energies after irradiation. Interestingly, a slight increase of oxygen after the irradiation process was found that might be caused by an enhanced oxidation process of Si after the ion bombardment. The observable peak around 99.5 eV (Figure 4.15b) correlates well with the energy for the Si 2p state of non-irradiated Si. [Atz80, Bla90] This peak shifts marginally to 99.2 eV after the irradiation process. At a binding energy of 103.2 eV we found an additional peak

that originates from the respective Si 2p peak of SiO_2. [Mou92, Nef77] Note, it cannot be distinguished between the referring $p_{1/2}$ and the $p_{3/2}$ peaks due to their closeness in binding energy, which could have been resolved only by employing highly monochromatic synchrotron radiation. [Him88] As Si surfaces oxidize quickly in air, the common oxygen features of SiO_2 [Nef77] are observable, irrespective of performing ion irradiation or not. *In-situ* XPS would solve the issue, but was unfortunately not available.

The high resolution ($\Delta E = 0.25$ eV) XPS spectra obtained for flat TiO_2 before and after the irradiation process are presented in the lower row of Figure 4.15. For non-irradiated TiO_2 the O 1s peak was observed at 529.9 eV [Mos78, Yu03], shifting slightly ($\Delta E = 0.3$ eV) to higher binding energies compared to irradiated TiO_2, but this shift is in the range of the resolution limit of the used XPS. In addition, a peak at 532.2 eV, originating from atmospheric OH-groups [Yu03] can be seen. Due to an evaluation of the corresponding peak areas, a slight decrease of the oxygen content was determined for irradiated TiO_2, which is in good agreement with [Nag75]. One can clearly see the Ti $2p_{1/2}$ and Ti $2p_{3/2}$ peaks of TiO_2 at the binding energy of 458.6 eV and 464.3 eV, respectively, that show no change after the irradiation process. In contrast, the untreated TiO_2 samples show an excess of oxygen due to the coverage with adsorbed OH molecules over long periods in atmosphere that is decreased after ion beam irradiation. The irradiated TiO_2 retained perfect stoichiometric surface even after weeks of exposure to air. According to Naguib and Kelley, [Nag75] an amorphization of TiO_2, Si, and SiO_2 is expected for ion fluences higher than 10^{13} ions/cm^2, which was the case in this study. Although a slight decrease of the oxygen content for irradiated TiO_2 can be found, a significant stoichiometric change can be excluded for both Si and TiO_2 by these XPS results. Thus, it can be excluded that further findings presented in this thesis are caused by an altered stoichiometry/surface chemistry.
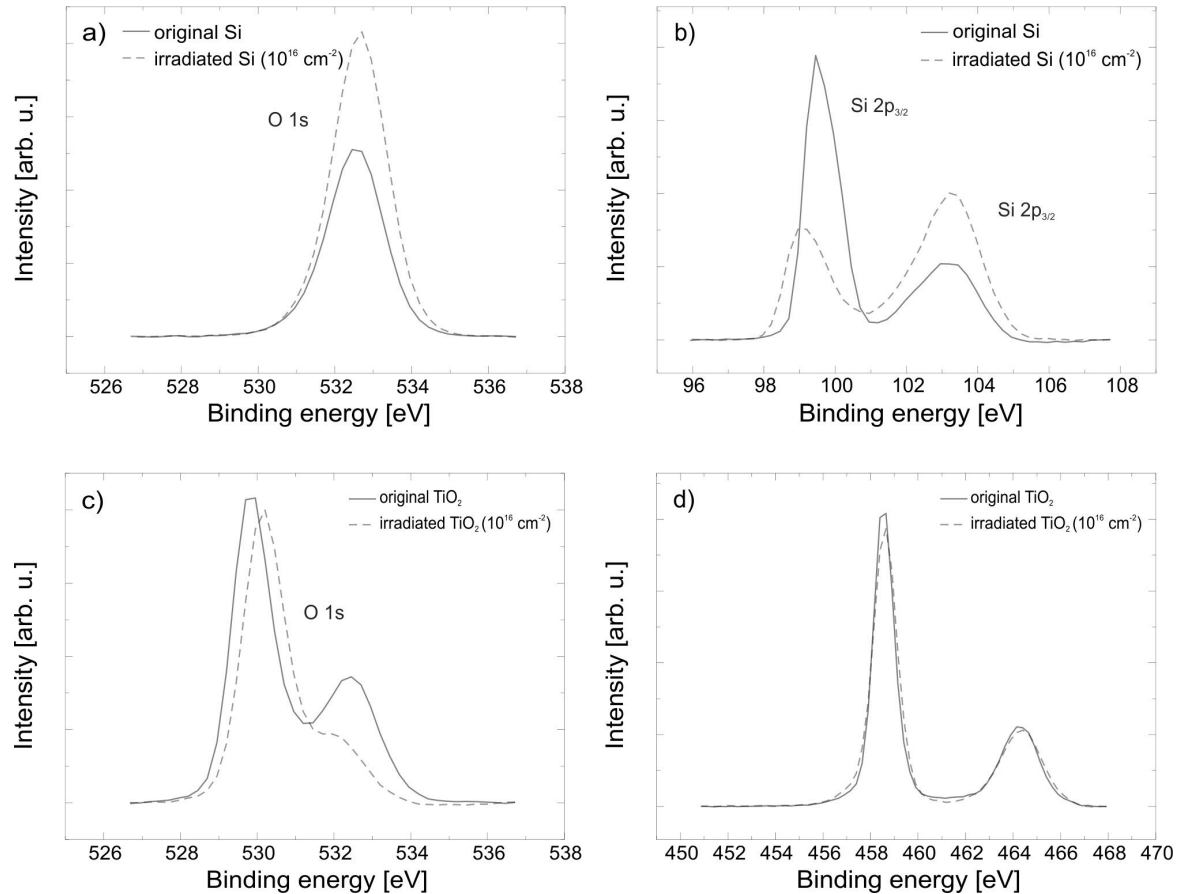
Figure 4.15: *XPS measurements for non-irradiated and irradiated Si (upper row) and TiO₂ (lower row) samples. The Shirley background was subtracted and Gaussian fits were applied. No stoichiometric changes could be seen after irradiation with xenon ions, only a slight variation of the oxygen content was detectable.*

Summarizing, xenon ion irradiation under 70° incidence induces a clear periodic nano-patterned ripple surface structure for both material systems, Si and TiO$_2$. The wavelength of these ripples is tunable through ion energy and the ion irradiation process has negligible effect on the surface stoichiometry/chemistry. The latter was detected by XPS and CAM investigations for flat surfaces. Each set of TiO$_2$ and Si samples exhibits the same surface chemistry before and after the ion irradiation process. However, the ripples have an influence on the hydrophobicity.

4.2.2   Ripples on Diamond Like Carbon

Two paths to synthesize substrates with tunable biocompatibility have been discussed above. Using one approach, the substrates' chemistry was changed by variation of the sp^3 content of ta-C layers on flat surfaces. With an alternate approach, the topography of well known substrates such as Si and TiO$_2$ was changed by introducing ripples to their surfaces. In this subsection, both approaches were combined. For this purpose,

rippled structures were introduced to a silicon substrate by xenon ion irradiation and subsequently covered with a thin ta-C layer. The irradiations were carried out with Mr. Jim Stringer and LEILA (Low Energy Ion ImplAnter). The latter is suitable for irradiations up to 10 keV. The xenon ion energy was varied between 5 and 20 keV, in order to realize different ripple wavelengths. The fluence was set to $\Phi = 6.8 \cdot 10^{16}$ cm^{-2} and the incident ion beam was tilted 70° to the surface normal. The obtained samples were split into two samples, with an area of (5 x 5)mm^2 each. One part of each sample was irradiated with ^{12}C$^+$ ions, that were accelerated to 1200 V. The deposited charge was set to Q = 0.05 mC, which equals a fluence of $\Phi = 1.86 \cdot 10^{17}$ cm^{-2}. Based on the results regarding the film thickness determination presented in chapter 4.1.2, these parameters lead to a film thickness of d $\approx$ 10 nm. This should be thick enough to muster tetrahedral bonding and therefore create a proper ta-C layer, but thin enough to maintain the ripple structure underneath. Afterwards, the covered and uncovered samples were investigated via AFM.

Figure 4.16 shows as example the height pictures and the respective cross sections for a silicon sample that was originally irradiated with xenon ions having an energy of 5 keV. The initially smooth features of the uncovered ripple structure seems to be blurred. Analyzing the sample's topographical characteristics manifests this impression. The original ripple structure had a wavelength of $\lambda = (48.0 \pm 5.1)$ nm and an average amplitude of A $= (4.0 \pm 1.4)$ nm. After depositing a ta-C layer on top, the wavelength slightly increased to $\lambda = (55.0 \pm 6.4)$ nm, which is, however, within the errorbars of the measurements. The average amplitude significantly decreases to A $= (1.2 \pm 0.7)$ nm. Note, the wavelength was determined by calculating the fast Fourier transformation (FFT) for each line of one AFM height picture. The wavelength for each line was then calculated by forming the reciprocal of the 1st order peak. The mean value was determined for each AFM picture and its standard derivation was set to be the wavelength error. Additionally, each sample was measured via AFM on at least three positions. Again, the mean value was calculated for the three averaged wavelengths and their standard derivations. The amplitude was also determined for each line on each AFM picture by first checking for minima and maxima, then calculating the distance between them, averaging the distances for each line and finally forming a mean value for each picture (see Appendix for the Matlab code). The error equals the mean value of the standard derivations of each line. The final values are a mean value for the analysis of three AFM images per sample.
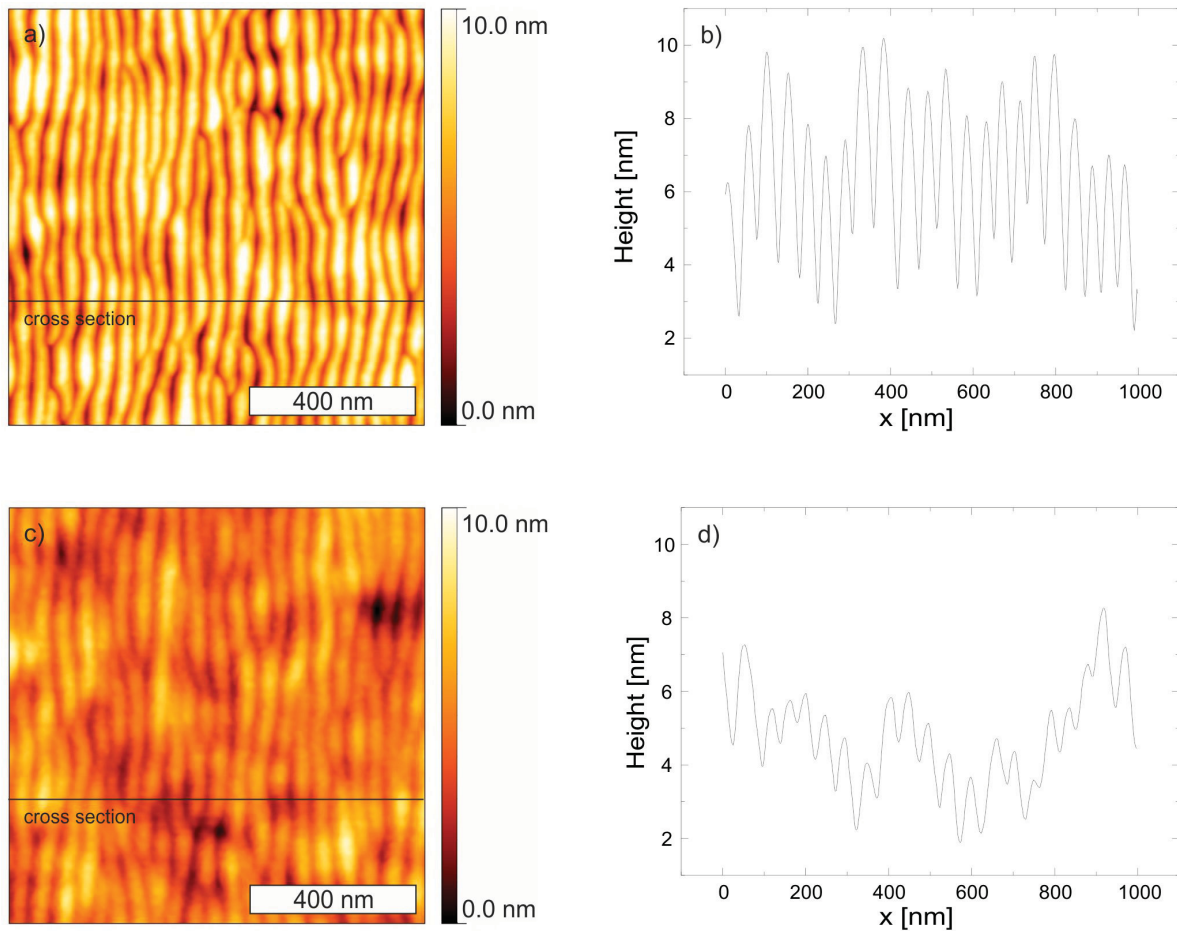
Figure 4.16: *AFM analysis of a ripple structure on a silicon substrate, which was afterwards covered with a ta-C layer. The xenon ion energy was 5 keV, which resulted in a ripple wavelength (for the sample shown in a) of ≈ 44 nm. A cross section taken along the black line (a) is shown in b). The ripples' amplitude was determined to be (4.0 ± 1.4) nm. c) shows the same sample, covered with a ta-C layer. The cross section in d) emphasizes the amplitude's decrease of about 3 nm to (1.2 ± 0.7) nm.*

The analysis of all samples shows no significant changes concerning their wavelength (see Figure 4.17a). Minor discrepancies between the presented data and the referring fit might be explained by re-appearance of ripple creating processes as the samples are locally tilted towards the ion beam due to the ripples. Sputtering and surface erosion might take place causing motion in the surface's features. However, a definite decrease of the ripples' amplitude after ta-C coverage is observed, as illustrated in Figure 4.17b. The diminution is highest for short-wavelength ripples around 45-55 nm and lowest for samples with a wavelength higher than 75 nm. One possible explanation for the decrease is a different sputter yield of each sample due to individual local curvature. The maximum tilting angle of a sinus-shaped surface depends on the ripple wavelength λ and the ripple amplitude A: $\alpha[°] = \arctan\frac{2\pi \cdot A}{\lambda}$. [Car99] Based on that consideration, findings indicate the ripples'

slope is decreased from $(27.5 \pm 10.8)°$ to $(12.8 \pm 7.1)°$ with increasing wavelengths. A TRIDYN simulation for 1 keV C$^+$ ions, a fluency of $\Phi = 1 \cdot 10^{16} \text{cm}^{-2}$ and varied irradiation angles shows that the sputter yield of silicon is only 0.39 atoms/ion for $12.8°$ irradiation angle and 0.53 atoms/ion for $27.5°$. Thus, the difference of the slope angles causes an increase of the sputter yield of about 20%, which is sufficient to have an impact on the diminution degree due to ta-C coverage.
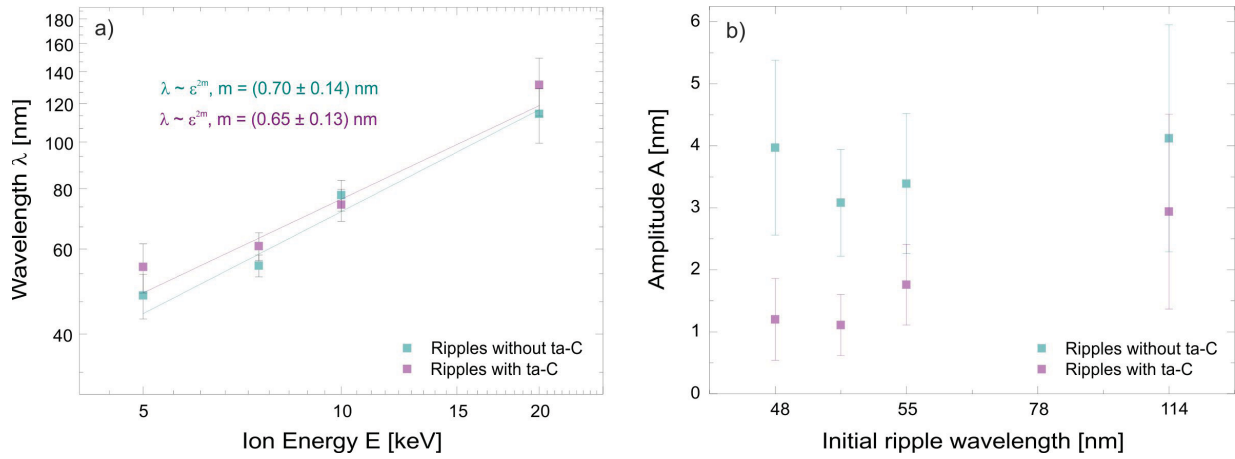
Figure 4.17: *Dependency of the obtained wavelengths (a) and amplitude (b) on the applied ion energies for Si before and after ta-C deposition. Apparently, there is no change in the wavelength. The referring fits emphasize the power law dependency for which the according exponents m have been calculated. The amplitude though, does change. Its decrease seems to depend on the substrate's initial wavelength.*

4.3   Summary and Conclusions

This chapter dealt with ion beam modification of surfaces, in particular, the mass separated ion beam deposition of tetrahedral amorphous carbon layers, the formation of ion beam-induced ripple formations.

The first part concentrated on the optimization of the deposition process. According simulations were carried out and afterwards implemented. A cylindrical capacitor was installed into the deposition chamber in order to determine the ion energy of the irradiating ions. Due to the special correlation between applied capacitor voltage and ion energy, it was possible to measure the ions' initial energy, which was determined to be (142.6 ± 2.9) eV. The presented error refers to the error of the fit. The ion energy distribution ranges between ≈ 20 and ≈ 100 eV. The influence of source parameters such as source voltage and source magnet current was also investigated. Both parameters can cause a shift in the ions' initial energy at the most of about 45 eV. In order to obtain a small energy distribution, the source voltage should be high and the source magnet current small. The influence of different source anodes was also investigated. Depending on the anode, the ions' initial energy can shift about 90 eV. It becomes clear there are many parameters influencing the ions' initial energy and, therefore, influence the sp^3 content of the obtained ta-C layers making it difficult to define a 'perfect' parameter set. Consequently, the applied sample voltage was adjusted by finding the maximum of the first derivative of the ion current on the sample at the beginning of each deposition session and adding the desired acceleration assured an average ion energy of 100 eV.

Ta-C layers, which were synthesized with varied ion energies, were characterized in order to verify the abovementioned procedural method. Therefore, XPS, Raman and AFM measurements were carried out. It was shown that a ta-C layer, which is synthesized with an ion energy of ≈ 500 eV contains a high sp^3 content ($> 70\%$) and is sufficiently smooth (RMS is less than 1nm). Film thickness measurements via SEM revealed that a deposition fluence of $7.4 \cdot 10^{17} cm^{-2}$ causes a film thickness of about 50 nm assuring a workable ta-C nanolayer.

The second part of this chapter focused on the creation of ion beam-induced ripples on Si and TiO$_2$. The wavelength dependency of the ripples on the applied ion energy was investigated via AFM, which confirmed the common power-law dependency. Contact angle measurements were performed in order to investigate the topographical influence on

the hydrophobicity. Silicon becomes slightly more hydrophilic, whereas TiO_2 becomes more hydrophobic when a ripple structure is introduced. No dependency on the ripple wavelength was observed within the ranges of error. XPS measurement support the theory, that no stoichiometric changes are caused by ion irradiation and therefore, will have no influence on the biological behavior of the materials that will be investigated in this thesis.

Finally, silicon ripples with varied wavelengths were covered with a ta-C layer in order to obtain ta-C ripples. AFM measurement showed, that though there was no change concerning the wavelength of the ripples, their amplitude was significantly decreased by carbon ion deposition. TRIDYN simulations proved that the sputter yield of the samples differ, depending on the samples' wavelength; the smaller the wavelength, the steeper the ripples' slope resulting in a higher sputter yield, causing a stronger diminution of the ripples' amplitude.

In conclusion, possibilities are shown in detail how ion beam irradiation is used to synthesize surfaces and tune their properties.

5 Protein Adsorption on Ion Irradiated and Flat Surfaces

This chapter presents results that were obtained concerning the adsorption behavior of HPF on flat surfaces in order to investigate the influence of the surface's chemistry. Well known surfaces such as Si, TiO$_2$ and highly oriented pyrolytic graphite (HOPG) were used to form a general idea of the adsorption process. Adsorption experiments were carried out on ta-C layers, in order to investigate their biocompatibility. Moreover, ta-C layers were doped with Ag and Ti to explore their influence on the adsorption behavior of HPF. The experiments were conducted in cooperation with Dr. Thomas Keller, Dr. Robert Schulze and Ralf Wagner from the Institute of Materials Science and Technology (IMT, Jena), as well as, Alexander von Müller (master thesis) [vM14].

5.1 Si and TiO$_2$

The adsorption behavior of HPF on flat, non-irradiated Si and TiO$_2$ substrates was investigated using a protein solution with a HPF concentration of c = 10 μg/ml. The Si samples were cut from a wafer with (100) orientation. Polished TiO$_2$ samples were ordered from CrysTec GmbH[1], having an orientation in (100) direction, too. Prior to the protein adsorption, AFM measurements were performed to measure the samples' surface roughness (RMS). Referring height images for Si and TiO$_2$ are shown in Figure 5.1a, respectively 5.1b. A RMS value of (0.19 ± 0.05) nm was obtained for plain, untreated Si, and (0.15 ± 0.01) nm for TiO$_2$. Although both samples were rinsed with ethanol and dried with compressed air, the silicon image shows minor pollutions (bright spots) that might originate from the wafer cutting. Because of the small height scaling, measurement-based noise is more visible, as the AFM is extremely sensitive to vibrational perturbations. The adsorption experiments were performed according to standard procedure defined in chapter 2.2. The middle row of Figure 5.1 shows the referring height pictures for Si (c) and TiO$_2$ (d) after the protein adsorption. The proteins homogeneously adsorbed on both substrates and created a dense film. Consequently, the roughness increased for Si to RMS = (0.48 ± 0.02) nm and for TiO$_2$ to RMS = (0.49 ± 0.02) nm. Agglomerations are

---

[1]Köpernicker Str. 325, 12555 Berlin, Germany, www.crystek.de

visible atop both HPF layers. Taking a closer look at the height images, a globular conformation of the adsorbed proteins can be hypothesized. In order to verify this statement and to investigate single proteins, the experiment was repeated using only a tenth (c = 1 μg/ml) of the initial HPF concentration. The lower row of Figure 5.1 shows the referring height pictures in higher resolution. Single proteins are highlighted and their cross sections (CS) are presented (insets). On silicon (e), slight networking is visible in the background. Networking occurs when the proteins' hydrophobic domains attach to a hydrophobic surface allowing the hydrophilic α chains to interact with each other. Some of this networking is marked within the white rectangle and for one protein, whose trinodular structure is well recognizable, its cross section along the long axis is shown. The marked protein has a length of L $\approx$ 52 nm and a height of H $\approx$ 0.6 nm. The errors of the determined protein's dimensions are assumed to be about 7 nm concerning lateral measurements and about 0.1 nm for vertical height determinations. The large error in horizontal direction is caused by the tip's dimension. In case of TiO$_2$ (f), proteins are marked that seem to adsorb in globular (CS 1) and trinodular (CS 2) conformation. The upper protein has a diameter of L $\approx$ 22 nm and a height of H $\approx$ 1.3 nm. It is slightly bigger than the lower, stretched protein that has a height of H $\approx$ 0.9 nm and a length of L $\approx$ 55 nm. The dimensions measured for the adsorbed proteins fit well with the ones that are presented in literature, indicating that the observed structures are indeed HPF. [Cac00, Mar03, Tun05] In these experiments, TiO$_2$ shows a more hydrophilic character in comparison with silicon, which is in good agreement with contact angle measurements presented in chapter 4.2.1. The measurements showed that TiO$_2$ is slightly more hydrophilic (having a contact angle of $(60.9 \pm 3.2)°$) than Si with its natural oxide layer. The latter exhibited a contact angle of $(84.5 \pm 4.6)°$ and is, therefore, considered to have a hydrophobic character when it comes to protein adsorption. In comparison, the contact angle of silicon and TiO$_2$ samples irradiated with 20 keV xenon ions and a fluence of $5 \cdot 10^{16}$ cm^{-2} did not change within the range of error, as shown in chapter 4.2.1. For silicon it was $(85.0 \pm 2.0)°$ and $(65.1 \pm 12.0)°$ for TiO$_2$. This lack of change in the contact angles reflects in the adsorption of HPF on both irradiated substrates; the HPF molecules form a dense film with only little networking (see Appendix). Thus, the adsorption of HPF on both substrates is not governed by ion beam-induced amorphization.

The fact that proteins in a globular conformation are observed more often on more hydrophilic surfaces than on hydrophobic ones is in agreement with the work of Marchin

and Berrie. [Mar03] Tunc et al. [Tun05] observed HPF that adsorbs in a globular conformation on 'hydrophobic' silicon, but their specially treated silicon samples had a much lower contact angle of $(27.7 \pm 3.1)°$ than the one investigated within this work.
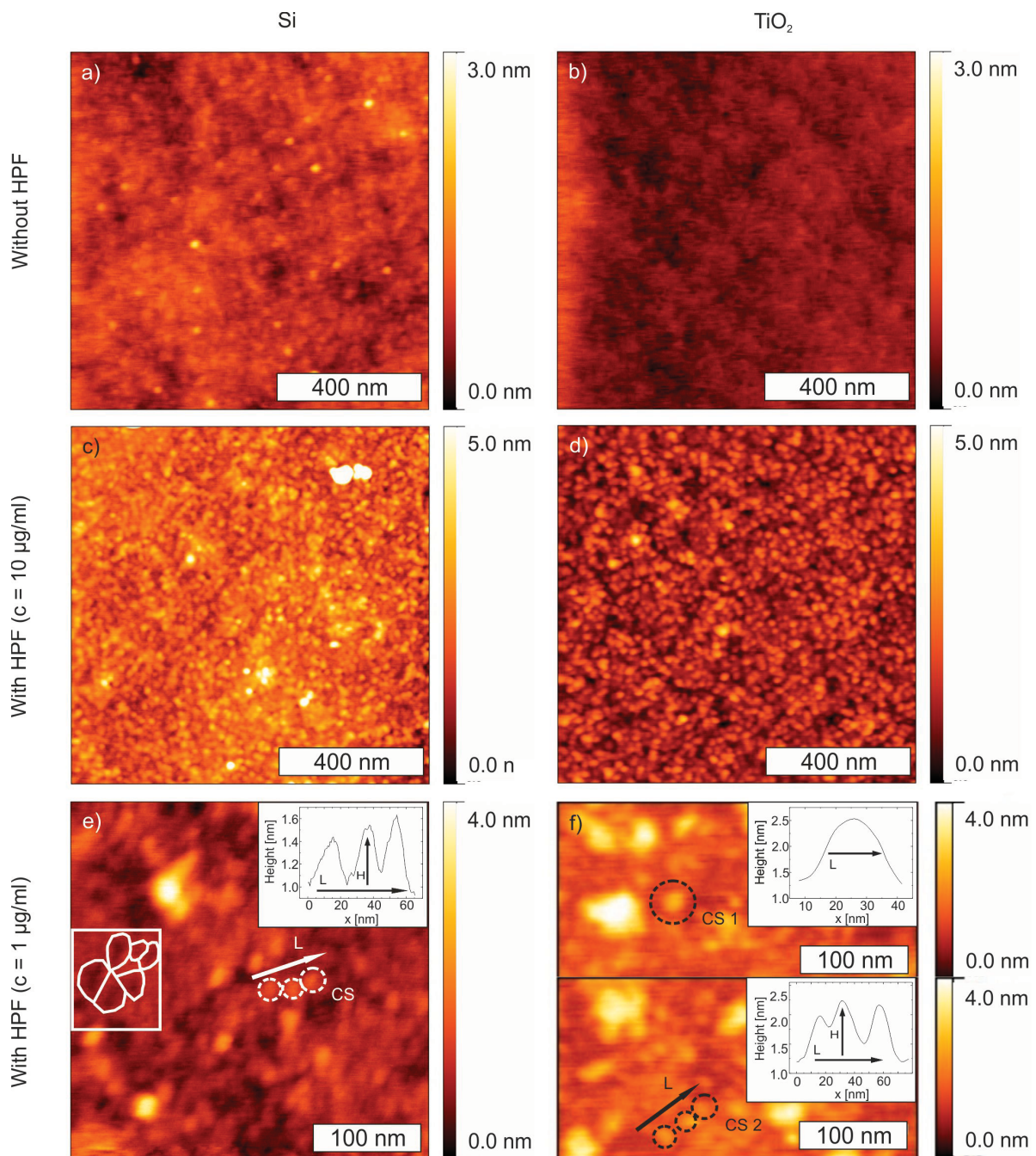
Figure 5.1: *AFM analysis of plain, untreated Si and TiO$_2$ substrates before (a, b) and after (c - f) protein adsorption. The protein concentration was set to c = 10 µg/ml (middle row) and to c = 1 µg/ml (lower row), respectively. Single proteins are highlighted and their cross sections (CS) are presented in the referring insets.*

5.2 HOPG and ta-C

In order to evaluate the influence of the sp^3 content of ta-C on the adsorption behavior of HPF, adsorption experiments were performed on strictly sp^2 bound highly ordered/oriented pyrolytic graphite (HOPG), as reference system. Figure 5.2a shows an according AFM height picture before protein adsorption. Due to the rather weak Van der Waals bonding between the single, covalently bonded graphene sheets, a terrace structure is created when the surface is cleaned with scotch tape. One of these steps was investigated in more detail, seen in Figure 5.2b. The step height (inset) is about h = 0.27 nm, which is slightly smaller than the value of h = 0.35 nm resulting from similar measurements. [Lui09] The discrepancy can originate from the scotch tape cleaning process or too strong an AFM force during this particular measurement. Because of this, special care was taken concerning the applied force during the following AFM measurements.

The HPF solution had a protein concentration of c = 10 μg/ml and was added onto the cleaned HOPG. Figure 5.2c represents the obtained AFM picture. A coarsely meshed net structure is created by the HPF molecules. A contact angle of $(97.4 \pm 6.2)°$ was measured for HOPG. Therefore, it is hydrophobic and networking is expected. [Mar03] When decreasing the protein concentration to a tenth c = 1 μg/ml, it is possible to determine single proteins bonding. In Figure 5.2d, one of the single proteins is emphasized and a cross section analysis was performed along and across the protein allowing a determination of the protein's dimensions. The individual nodes of the marked protein are clearly visible in the inset. Several proteins were investigated accordingly. On average, a single HPF molecule has a length of L = (79.4 ± 17.6) nm, a width of W = (24.0 ± 2.0) nm and a height of H = (1.6 ± 0.5) nm. These results are comparable with the ones obtained by Marchin and Berrie (L = (62 ± 9) nm, W = (28 ± 7) nm, H = (1.05 ± 0.13) nm). [Mar03] Their proteins are shorter and broader, possibly due to Marchin and Berrie investigating freestanding proteins, whereas the proteins presented here were positioned closer to each other, allowing interaction. This could lead to a stretching of the proteins and cause difficulties concerning the determination of single proteins' restrictions. Marchin and Berrie themselves claim that the measured height presented in their work is uncharacteristically small due to the applied forces during the AFM investigations.
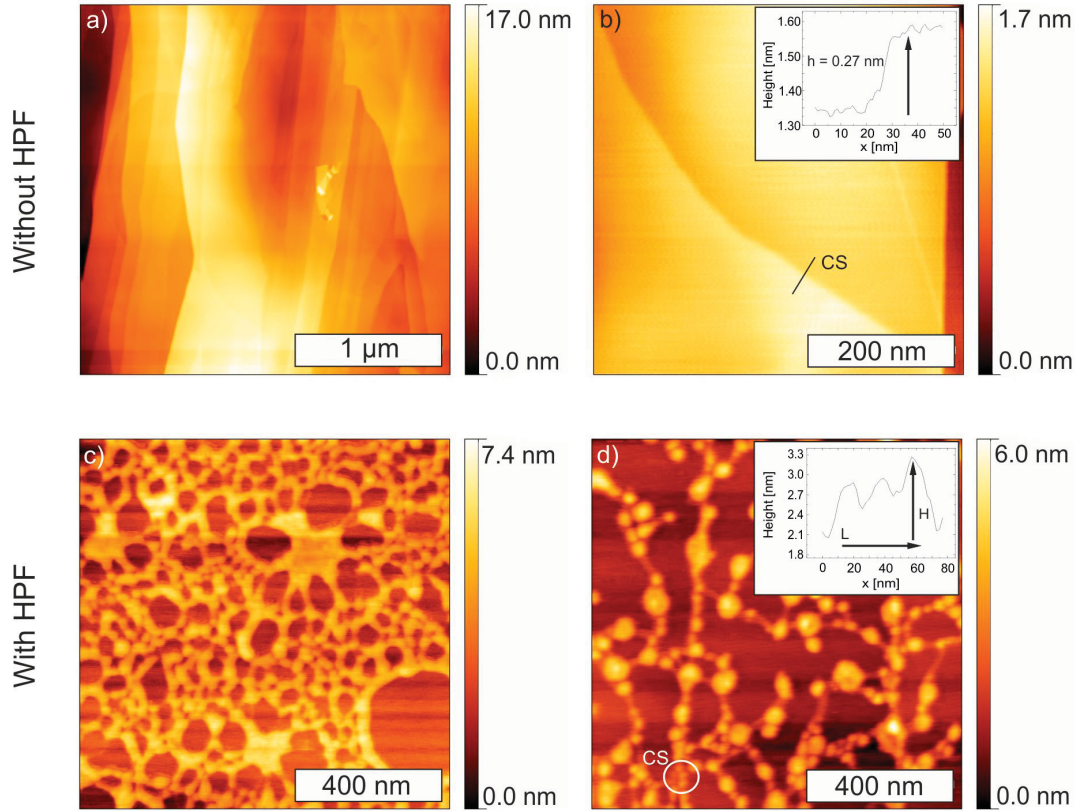
Figure 5.2: *AFM analysis of plain, scotch tape-cleaned HOPG with and without adsorbed HPF. a) The characteristic terrace-like structure is visible on a large-scale height image. b) Zoom in on one step enables a measurement of its hight (inset of b), which equals h = 0.27 nm. c) HPF was adsorbed with a HPF concentration in solution of c = 10 µg/ml resulting in a coarsely meshed net structure due to inter-protein bonding. d) By decreasing the proteins' concentration to c = 1 µg/ml, a cross section analysis (CS) of single proteins along (see inset) and across single proteins was possible. On average, a single HPF molecule has a length of L = 79.4 ± 17.6 nm, a width of W = 24.0 ± 2.0 nm and a height of H = 1.6 ± 0.5 nm.*

With respect to the trinodular structure of HPF, its volume can be determined approximating an ellipsoidal shape:

$$V_{ellipsoid} = \frac{\pi}{6} \cdot l \cdot w \cdot h$$
$$V_{HPF,experiment} = (1600 \pm 1000)nm^3.$$

(5.1)

The obtained volume is almost 50% bigger than the one of V = (1000 ± 500) nm^3 that can be calculated for the free-standing proteins on HOPG from Marchin and Berrie, but with respect to the large errors acceptable, as the applied approximation is rather rough. The protein adsorption on ta-C was investigated next. Samples of different sp^3 contents were prepared by MSIBD (see chapter 4.1) by using different ion energies. The carbon ions' deposition energies were set to 150 eV, 518 eV and 1100 eV. According to the findings from XPS measurements presented in chapter 4.1.2, the sample synthesized with 550 eV

ions has the highest sp^3 content of $\gtrsim 70\%$. The other two samples have a lower sp^3 of $\gtrsim 40\%$. The HPF concentration within the PBS solution was c = 10 $\mu g/ml$. Figure 5.3 shows the obtained AFM height images before (left column) and after (right column) protein adsorption for the different samples. No adsorbed proteins were observed for the sample that was synthesized with 150 eV carbon ions (a + b). The sample with the highest sp^3 content is shown in the middle line. Here, proteins and their trinodular conformation are clearly visible. Single proteins were marked and the cross section of one is presented in the inset. The molecule has a length of ≈ 74 nm and a height of ≈ 0.8 nm. As the proteins are positioned very close to each other, it was not possible to determine their specific boundaries and thus, to statistically evaluate their dimensions. The lower line in Figure 5.3 shows the results for the ta-C layer that was synthesized with 1100 eV carbon ions. Interestingly, a dense film of adsorbed HPF molecules is visible, although the layer's sp^3 content should be not significantly different from the one presented in the first line of this figure. Contact angles were also determined for these layers and reveal that the 1100 eV sample is more hydrophilic with a contact angle of $(70.2 \pm 0.6)°$ in comparison to the 150 eV layer that has a contact angle of $(79.0 \pm 1.1)°$. This might explain small differences in the conformation but not why there are no proteins to be seen on the 150 eV layer. Consequently, the question arises whether this is an effect of the surfaces' topographies. It is obvious from the height images before protein adsorption, that the layers' roughness vary immensely. The sample produced with the lowest ion energy has a roughness of RMS = (3.4 ± 0.9) nm before (a) and RMS = (3.5 ± 0.5) nm after (b) the adsorption process. The 518 eV sample (c) is much smoother and has a roughness of RMS = (0.54 ± 0.03) nm, which is increased to RMS = (0.79 ± 0.24) nm (d). The roughness of the last sample almost triples from a very smooth RMS = (0.20 ± 0.03) nm to RMS = (0.56 ± 0.05) nm, shown in (e) and (f). In the presented case, the adsorption density inversely correlates with the surfaces' initial roughness. Cai et al. [Cai06] excluded this effect in their work, but their surface roughness ranged from ≈ 2 nm to ≈ 20 nm and was investigated on titanium. Thus, these different results are no contradiction. The influence of the surface topography will be studied in more detail later in this work (see chapter 6).
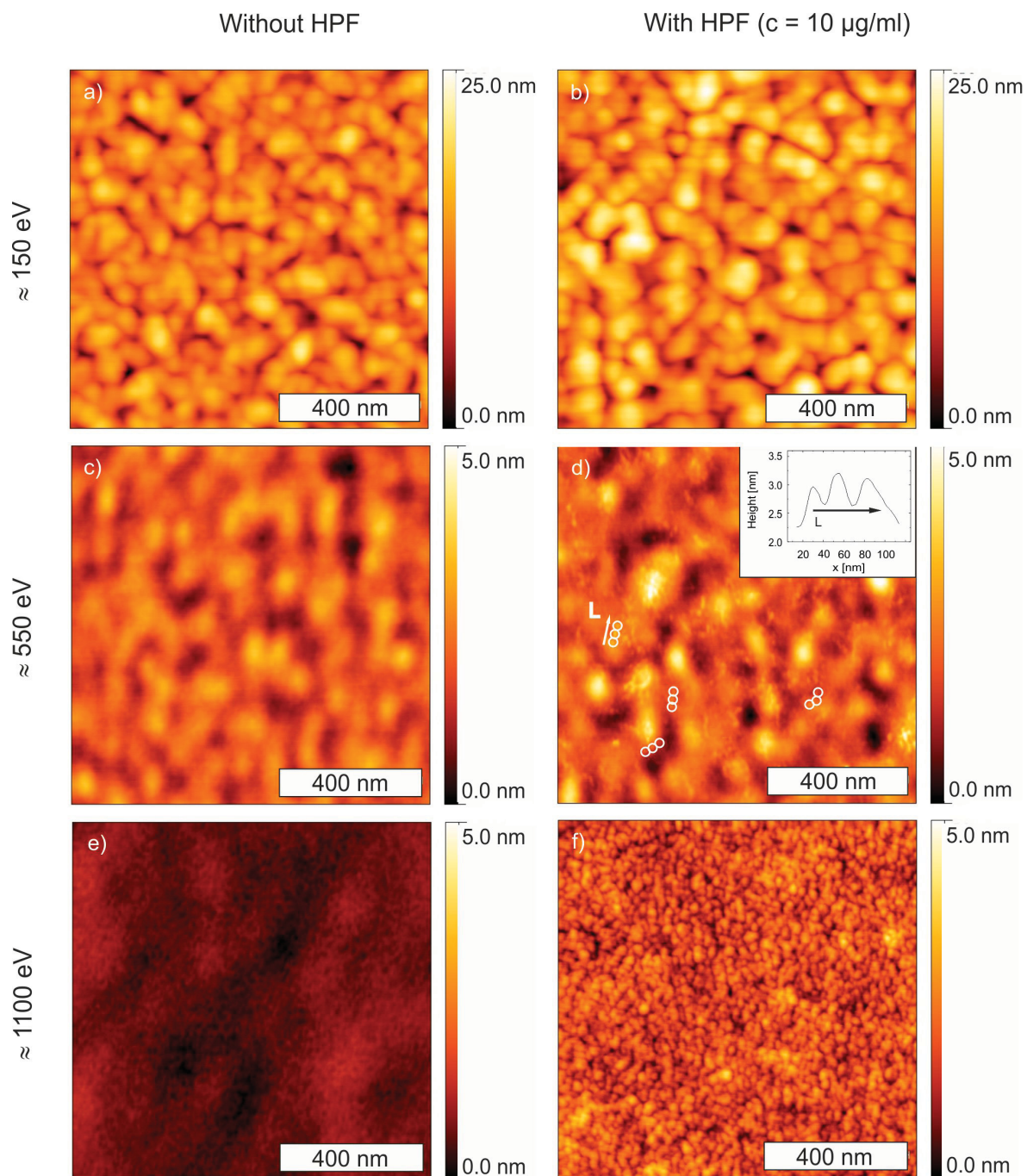
Figure 5.3: *AFM analysis of ta-C layers with varied sp^3 content before (left row) and after (right row) protein adsorption. The protein concentration was $c = 10 \, \mu g/ml$. No proteins were observed for the layer that was synthesized with the lowest ion energy of 150 eV (a + b). Some proteins that adsorbed in a trinodular conformation are marked white for the sample with the highest sp^3 content (c + d). The protein's dimension (inset) were measured to be $L \approx 74 \, nm$ and $H \approx 0.8 \, nm$. e + f) The ta-C layer was synthesized with 1100 eV carbon ions. The adsorbed HPF molecules form a dense film.*

In order to verify that no proteins adsorbed on the 150 eV ta-C layer, the adsorption experiment was repeated with a reduced HPF concentration of $c = 1 \, \mu g/ml$. A comparison of before and after protein adsorption is presented in Figure 5.4. The upper two rows

show the height and amplitude images for the ta-C substrate before and after the protein adsorption. The surface itself is rough (RMS = (1.8 ± 0.2) nm) and no adsorbed HPF molecules are visible. Only when observing the phase images (bottom row) as well, can proteins be detected on the right column (Figure 5.4e and the referring zoom in Figure 5.5a) as bright, roundish spots. The phase image basically represents the phase shift between the initial oscillation of the AFM tip and the changed one due to the interaction of the tip with the surface. The interaction with soft matter is different than the one with hard matter, which enables a differentiation between the proteins and the substrate. Additionally, this kind of AFM picture does not rely on the response of the piezo crystal. It is free of referring shifts and consequently higher in resolution as the height picture for instance. This observation emphasizes how crucial the choice of investigation method is.

Without HPF

With HPF (c = 1µg/ml)
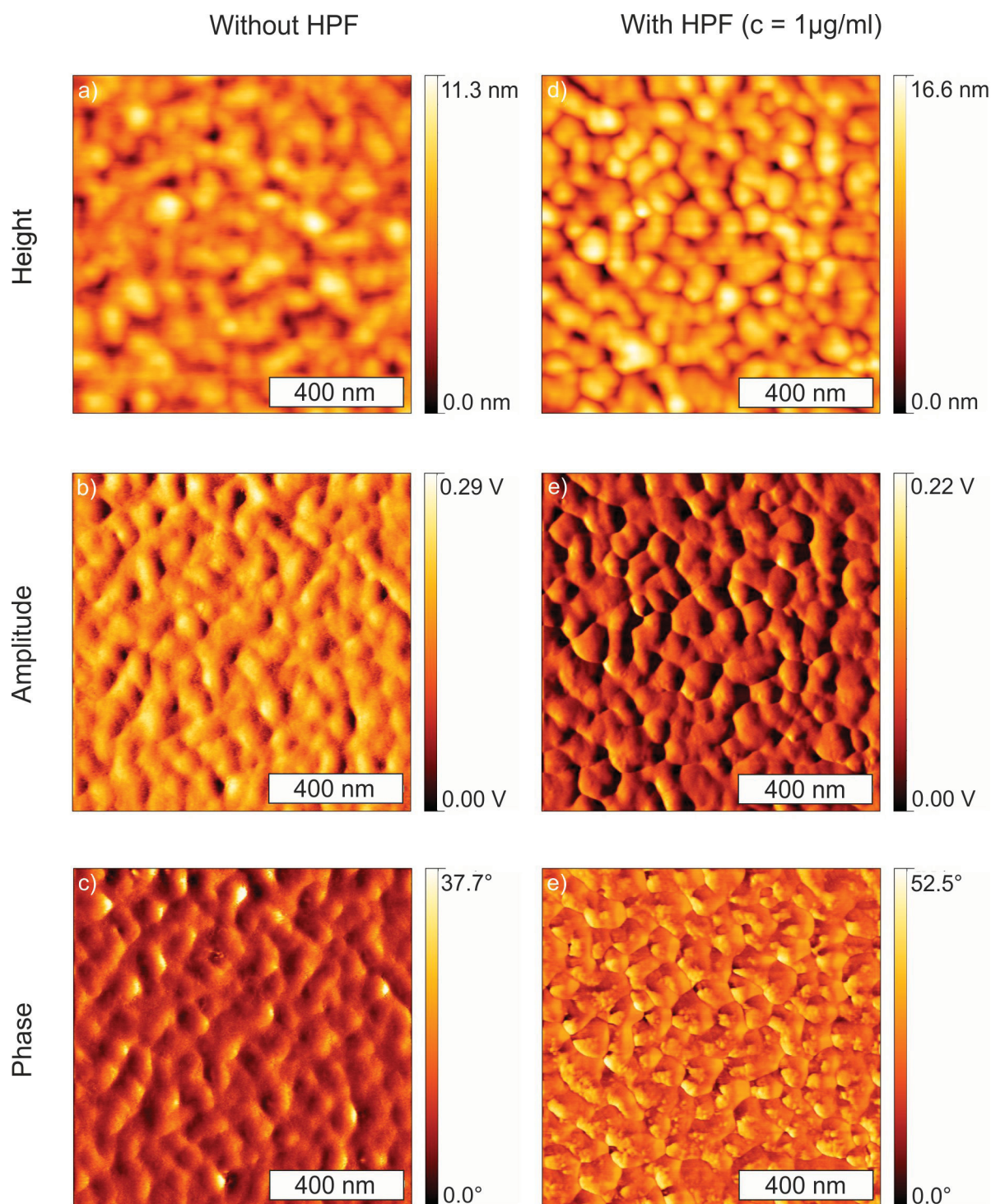
Figure 5.4: *AFM analysis of a ta-C layer before (left column) and after (right column) the protein adsorption. The sp^3 content should be about 80% based on the deposition energy of 150 eV. The protein concentration was only c = 1 µg/ml, in order to investigate single proteins. Three different kinds of AFM picture were recorded: the height image (a+d), the amplitude image (b+e) and the phase image (c+e). Here, only the latter allows the detection of adsorbed HPF molecules (see also zoom in Figure 5.5).*

A closer look was taken on the phase image of ta-C after the protein adsorption. Figure 5.5a shows an according zoom. A single HPF molecule was marked (Figure 5.5a) and investigated more closely. The upper graph shows the cross section along the long side of the protein body. The three characteristic nodes are clearly visible. Although it is not possible to determine the protein's height based on the phase image data, its length can be measured. The observed length of L = 65.2 ± 2.0 nm matches very well with the one of L = 62 ± 9 nm presented by Marchin and Berrie for HPF adsorbed on a hydrophobic substrate. [Mar03] Apparently, this ta-C layer exhibits a hydrophobic surface character as can be concluded not only by the protein's length but also its trinodular conformation. This hydrophobic character is in agreement with the presented contact angle measurements in chapter 4.2.1. As on a hydrophilic surface, a globular conformation is expected, which is clearly not the case. The lower graph of Figure 5.5b shows the cross section taken across the HPF molecule. The width was defined to correspond with the FWHM of the Gaussian fit, which is W = 11.6 ± 0.9 nm. This value is two times smaller than the expected one of about W = 24 nm, that was found for the proteins adsorbed on HOPG. The rough underground might cause this difference. As the height-scaling in the phase imaging is not linear, FWHM values might change. The reduced protein concentration allowed distinguishing between single proteins. The presented values were averaged by measuring three different proteins.
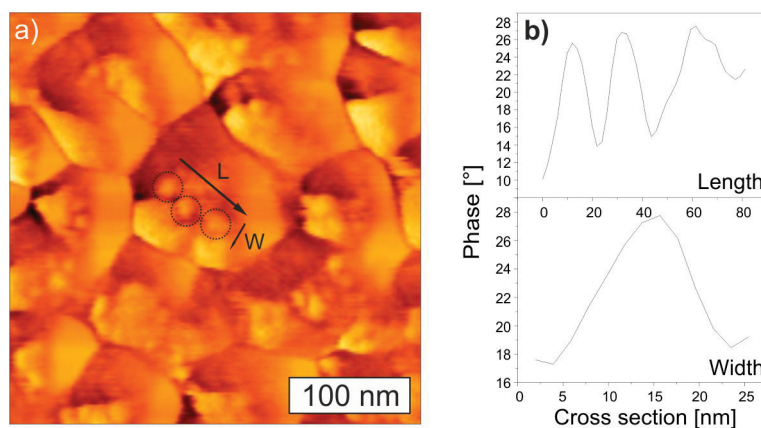
Figure 5.5: *AFM analysis of a single HPF molecule on a ta-C layer. As the set carbon ion energy was about 150 eV. The protein concentration was c = 1 µg/ml. a) Zoom in on the phase image of Figure 5.4f. One protein is marked and the directions of the referring cross sections are indicated. b) The graphs for the cross sections along (upper image) and across (lower image) the protein body. The three characteristic nodes are clearly visible. The protein's dimension were measured to be L = 65.2 ± 2.0 nm and W = 11.6 ± 0.9 nm.*

5.3 Doping Effects

As was shown in chapter 2.1.3, doping is a powerful tool to tune the biocompatibility of substrates. The importance is emphasized by a vast quantity of published papers that deal with this matter. [And06, Che09a, Liu08, Lia12] Initially, the topic might seem to be exhausted. Closer investigation discloses a weak point in most of the publications. In many cases the doping was done during film growth via radio frequency magnetron sputtering and the dopant's concentration was only controlled by the dopant-containing gas flow. [Lia12] In those cases, information about the dopant concentration in the ta-C layer could only be provided by additional investigations such as XPS analysis. [Lia12, Liu08, Che09a] By implanting substrates via ion beam implantation with a current measurement setup on the sample, as was done for this work, it is possible to precisely tune the number of ions hitting the target. Also, the mentioned studies lack in information concerning the concentration distribution of the dopants. [Che09a, Lia12, Liu08] Since the surface chemistry is supposed to have a major influence on the adsorption behavior of biologically relevant molecules, it is crucial how closely to the surface and how broadly in depth the dopants are distributed. Ion implantation allows a precise control of the ions' penetration depth. The ions' distribution can be obtained from according simulations that take the ions' energy and the applied fluence into account. Finaly, and most importantly, as a result of the deposition process, many groups cannot exclude any hydrogen incorporation into their films. [Che09b, Sri12, Wen02] As hydrogen is hardly measurable, it is not clear if the observed effects might be caused by a varying hydrogen content. For the work at hand, the mass selection ensures that only hydrogen-free amorphous carbon was investigated.

Prior to the doping itself and the subsequent HPF adsorption, simulations were performed to determine the required ion energies considering the target's composition, the ion's species and the desired implantation depth and dopant concentration within the substrate. Although simulation programs such as TRIM (part of the SRIM package 'Stopping and Rang of Ions in Matter' by James Ziegler [Zie85]) provide a quick calculation of the implantation profile, their calculated sputter yields are only valid for small fluencies. As sputter effects can have an impact when it comes to low ion energy implantation with high fluence, a dynamic simulation program, such as TRIDYN [Möl84, Möl88] is more adequate; it factors possible sputtering and dynamically conforms the implantation pro-

file, accordingly. Simulations were carried out concerning doping with Ag ions because Ag is well know to have a toxic character when interacting with biological material. Lok et al. [Lok06] believe the toxicity of Ag on cells to originate from a depletion of the intercellular ATP [2] levels. They also claim that it makes a significant difference whether Ag nanoparticles or ions are used, as nanoparticles have a lower effective antibacterial concentration. However, Ismail et al. [Ism07] argue that Ag is antibacterial because it blocks microbial DNA.

Naturally, the implanted Ag ions should be relatively close to the ta-C surface to have an effect on the biological material. In order to determine the required ion energy, the TRIDYN simulation parameters were chosen as follows. The ta-C layer had a density of $\rho_{ta-C} = 3$ g/cm^3 and a thickness of $d_{ta-C} = 15$ nm. The fluence was set to $\Phi_{Ag} = 7.75 \cdot 10^{14}$ cm^{-2}. The simulations were carried out for 10 000 Ag$^+$ ions with varied ion energies in the range of 1 to 10 keV. Figure 5.6a shows the obtained implantation profiles. For an Ag ion energy of 10 keV, the implantation distribution has its maximum in a depth of (8.9 ± 3.7) nm. With decreasing ion energy, the maximum of the dopant's concentration moves closer to the surface. For 3 keV Ag ions, the implantation maximum is in a depth of (4.8 ± 1.8) nm and in a depth of (2.9 ± 1.0) nm for 1 keV Ag ions, respectively. The width of the implantation profile is governed by straggling. Hence, the ion distribution gets sharper for lower ion energies. In order to experimentally verify the correlation of ion energy and implantation depth, XPS measurements were carried out. Figure 5.6b illustrates the different penetration depths of Ag that was implanted with the simulated energies of 1, 3 and 10 keV by means of the obtained intensities that were obtained for the Ag 3d peaks. The binding energy of the Ag $3d_{3/2}$ peak is ≈ 368 eV. The referring peak for Ag $3d_{1/2}$ was found around 374 eV. These binding energies are in good agreement with literature values of 368.3 eV for the Ag $3d_{3/2}$ peak and 374.4 eV for the Ag $3d_{1/2}$. [Mou92] Evidently, the intensities of both peaks decrease significantly with increasing ion energy. As XPS is rather surface sensitive, the Ag signal gets weaker the deeper into the material the Ag is deposited. Consequently, the Ag peaks for Ag ions that were implanted with an ion energy of 10 keV are hardly visible, because their implantation range of (8.9 ± 3.7) nm is beyond the depth resolution of XPS. In general, it is favorable to choose an ion energy that assures the dopant is close enough to the surface to effect surface related interactions but located deep enough in the substrate to

---

[2]Adenosine triphosphate (ATP) is a common energy supplier in each cell. By enzyme-caused cracking of the phospate bondings of ATP, energy is released.

not be rinsed/rubbed/scratched off easily. Hence, for Ag ions, an ion energy of 1 keV is appropriate.
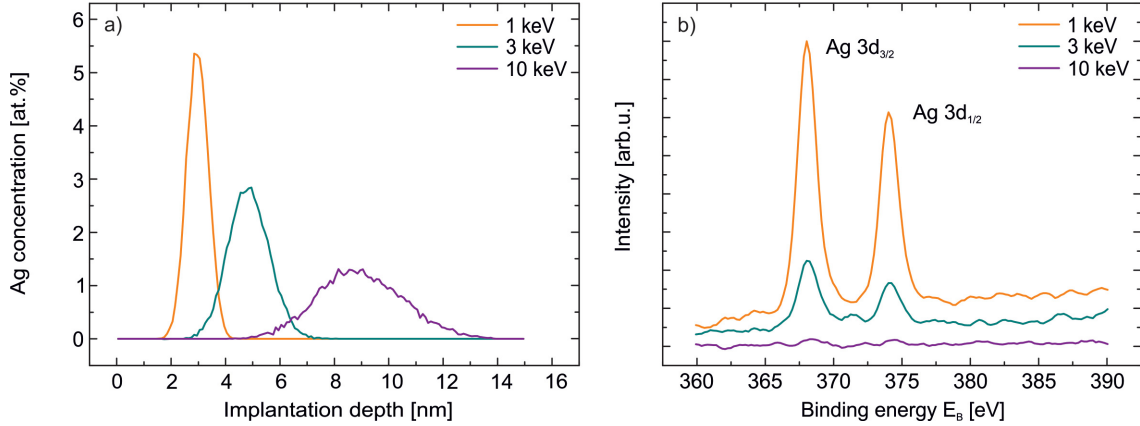
Figure 5.6: *a) TRIDYN simulation for Ag^+ irradiation of a ta-C layer with a fluence of $\Phi_{Ag} = 7.75 \cdot 10^{14}$ cm^{-2}. The ion energies varied between 1, 3, and 10 keV. The smaller the ion energy, the closer the ions are implanted to the surface and the sharper is their distribution within the target. b) XPS measurements show referring Ag 3d peaks at a binding energy of $\approx$ 368 eV and $\approx$ 374 eV. The smaller the ion energy, the more intense the Ag signal becomes and consequently, the closer to the surface the silver is located.*

Next, TRIDYN simulations were performed to determine the dopant's concentration that results from different ion fluencies. For this purpose, the Ag^+ implantation energy was set to 1 keV. The ta-C layer was assumed to have a density of $\rho_{ta-C} = 3$ g/cm^3 and a thickness of $d_{ta-C} = 6$ nm. Figure 5.7 shows the obtained implantation profiles. There is an increase of the Ag concentration with increasing fluence. Table 5.1 shows the Ag concentration with the referring maximum's position and FWHM of the ions' ranges for varied fluencies. The ion fluence has no effect on the implantation depth, showing that sputtering is not significant. The FWHM increase about 28 % when comparing the smallest and the highest fluence, which shows that ion beam mixing is significant and that using TRIDYN instead of TRIM is more accurate.

Table 5.1: *Implantation depth and width ($d_{Ag}\pm$ FWHM) and dependency of the silver concentration in this depth (c_{Ag} in d_{Ag}) and integrated over the entire profile on the deposited fluency Φ_{Ag}.*

Φ_{Ag} [cm^{-2}]	$d_{Ag} \pm$ FWHM [nm]	c_{Ag} in d_{Ag} [at.%]	c_{Ag}, integrated [at.%]
$1.3 \cdot 10^{14}$	3.0 ± 0.8	1.0	0.9
$6.5 \cdot 10^{14}$	3.0 ± 0.9	4.6	4.6
$1.3 \cdot 10^{15}$	3.0 ± 1.1	8.5	9.6
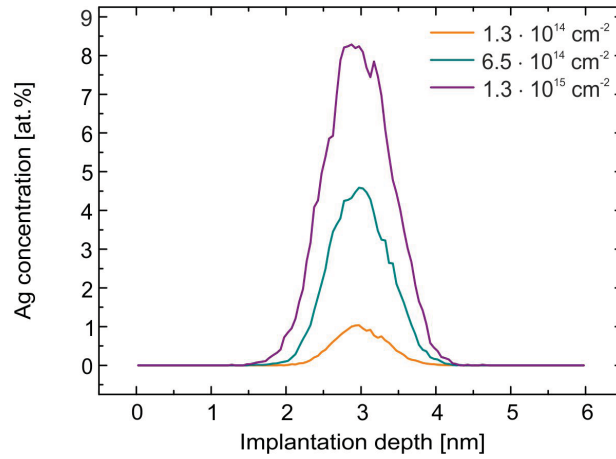
Figure 5.7: *TRIDYN simulaion for 1 keV Ag$^+$ implantation with varied fluencies that resulted in tunable Ag concentrations within the material (here: ta-C).*

The implantation profile that results from ion implantation depends on the ion energy, ion fluence, and on the ion mass and charge, which contribute to the interaction behavior within in a material. Additional simulation studies for four different dopants (N, F, Ti and Ag) were performed. The chosen dopants are suspected to influence the biocompatibility of the substrates in which they are implanted, as was shown in many studies. [Che09a,Che09b,Sri12,Has07] The simulations were carried out for singly charged ions with an energy of 1 keV. The same assumptions as presented above were made for the ta-C layer ($\rho_{ta-C} = 3$ g/cm^3 and $d_{ta-C} = 6$ nm). Figure 5.8 shows the obtained implantation profiles for the referring TRIDYN (a) and TRIM (b) simulation. In comparison, both simulation programs provide the same profiles: Due to their differences concerning their scattering cross section, the lighter, smaller dopants N and F cause a much broader ion distribution than the heavier and bigger dopants Ti and Ag. Note, although silver is by far the heaviest ion within this simulations, its penetration depth is about 1 nm higher than the ones of the other dopants. Usually, lighter ions penetrate deeper into the target material because their electronic energy loss is smaller than the one of heavier ions. But electronic energy loss has only little influence for small ion energies around 1 keV, which is the case here. Nuclear energy loss dominates when implanting with this small ion energies. Hence, lighter ions are scattered within the first nm of the target material. Figure 5.8 reveals how important the choosing of the simulation program is. As the applied irradiation energy is rather small in comparison to commonly used implantations, that range in the higher keV to MeV regime, surface sputtering is a key factor when investigating the implantation profile. TRIDYN takes sputtering into account, meaning the simulation is dynamical. TRIM does not. As a consequence, the penetration depth of a dopant shifts.

Table 5.2 discloses the maximum of the dopants' implantation depths and their FWHM for both simulations. Taking into account the dynamics caused by sputtering shifts the maximum of the implantation profile 0.3 - 0.6 nm closer to the surface. This is crucial in terms of surface physics and biomaterial experiments.
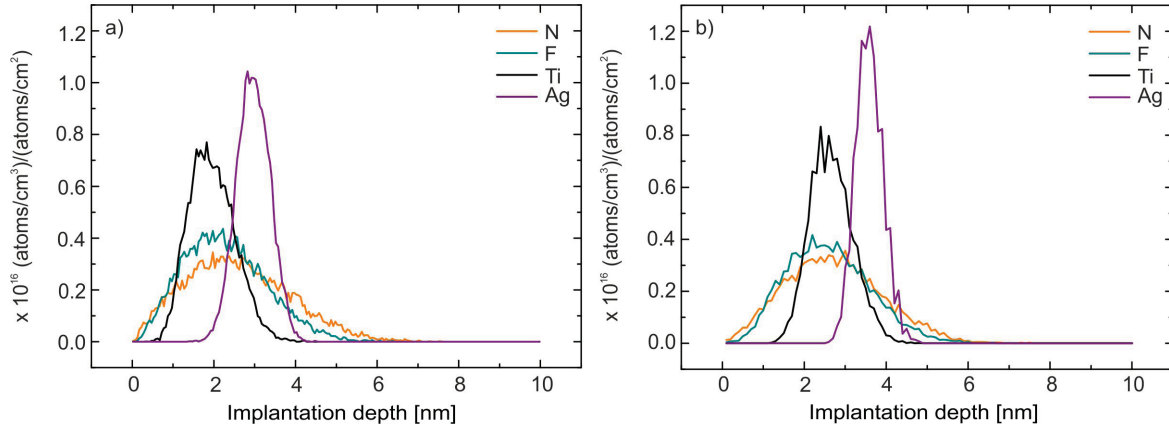
Figure 5.8: *Doping profiles for different singly charged dopants (N, F, Ti and Ag). The dopant ion energy was 1 keV. The TRIDYN (a) and the TRIM (b) calculation were carried out for 10 000 projectiles.*

Table 5.2: *Implantation depth and width (d ± FWHM), for different dopants. The simulations were carried out using TRIDYN and TRIM.*

Dopant	d_{dopant} ± FWHM, TRIDYN [nm]	d_{dopant} ± FWHM, TRIM [nm]
N	2.4 ± 3.2	2.7 ± 1.2
F	2.1 ± 2.4	2.5 ± 1.0
Ti	1.9 ± 1.4	2.6 ± 0.5
Ag	3.0 ± 1.0	3.5 ± 0.2

For the adsorption experiments with Ag ions, a ta-C sample was split into four samples. Three of the samples were subsequently irradiated with 1 keV Ag^+ ions. One sample remained untreated as reference. The fluencies were set to $\Phi_{Ag} = 1.3 \cdot 10^{14}$ cm^{-2}, $\Phi_{Ag} = 6.5 \cdot 10^{14}$ cm^{-2} and $\Phi_{Ag} = 1.3 \cdot 10^{15}$ cm^{-2}. These values correspond to Ag concentrations of about 1.0 at.%, 4.6 at.% and 8.5 at.% in the maximum of the implantation profile. Afterwards, the obtained surfaces were investigated via AFM. The undoped ta-C layer had a roughness of RMS = (0.20 ± 0.03) nm. This does not change for the samples with 1.0 at.% and 4.6 at.% silver. The sample with 8.5 at.% Ag doping is significantly rougher (RMS = (0.49 ± 0.06) nm). Due to the relatively high Ag concentration within the ta-C matrix, nanocluster might form and diffuse towards the surface, [Ger02] which can cause an increased RMS roughness.

Figure 5.9 shows the AFM height pictures of the undoped and doped samples after

the protein adsorption. The protein concentration was c = 10 μg/ml. Obviously, there are no differences to be seen. All samples exhibit a dense HPF film, with some minor gaps. The proteins seem to preferably adsorb in a trinodular conformation. There are few molecules in globular conformation visible (brighter spots), but it is not possible to exclude that they adsorbed on already adsorbed proteins underneath. The roughness (RMS) of all samples HPF-characteristically increased to (0.56 ± 0.05) nm(undoped), (0.59 ± 0.04) nm (1.0 at.% Ag), (0.53 ± 0.04) nm (4.6 at.% Ag) and to (0.67 ± 0.06) nm (8.5 at.% Ag). In conclusion, silver doping of a ta-C layer has no apparent impact on the protein adsorption density in the given experiment. A reduced protein concentration is recommendable to obtain more information about the proteins' conformation. The lack of influence of silver doping on the adsorption of HPF shows that it is possible to have an antibacterial and biocompatible material.

Next to the dopant Ag, works by Andara et al. [And06] and Cheng et al. [Che09b] suggest that Ti might also be a powerful dopant regarding the biocompatiblity, as was explained in detail in chapter 2.1.3.

A ta-C layer was irradiated with 1 keV Ti$^+$ ions. The fluence was $\Phi_{Ti} = 6.5 \cdot 10^{14}$ cm^{-2}, which corresponds to a Ti concentration in the maximum of the implanation profile of about 5 at.%. AFM investigations revealed that the initial roughness of the ta-C layer of RMS $= (0.33 \pm 0.02)$ nm maintained after titanium irradiation (RMS $= (0.33 \pm 0.06)$ nm). Figure 5.10a shows the height image of the Ti doped ta-C layer before protein adsorption. A dense HPF film is visible after protein adsorption (see Figure 5.10b). Its appearance resembles the ones that were obtained for silver doped and undoped ta-C layer, shown in Figure 5.9. The HPF molecules predominantly adsorb in a trinodular conformation, which allows little networking that causes small gaps in the film (dark spots). This behavior is comparable with the one described in chapter 5.1 for the adsorption on TiO$_2$. The roughness of the Ti doped sample increases after protein adsorption to RMS $= (0.57 \pm 0.05)$ nm. Evidently, also the doping of ta-C with Ti has no significant influence on the adsorption behavior of HPF under the given adsorption conditions.
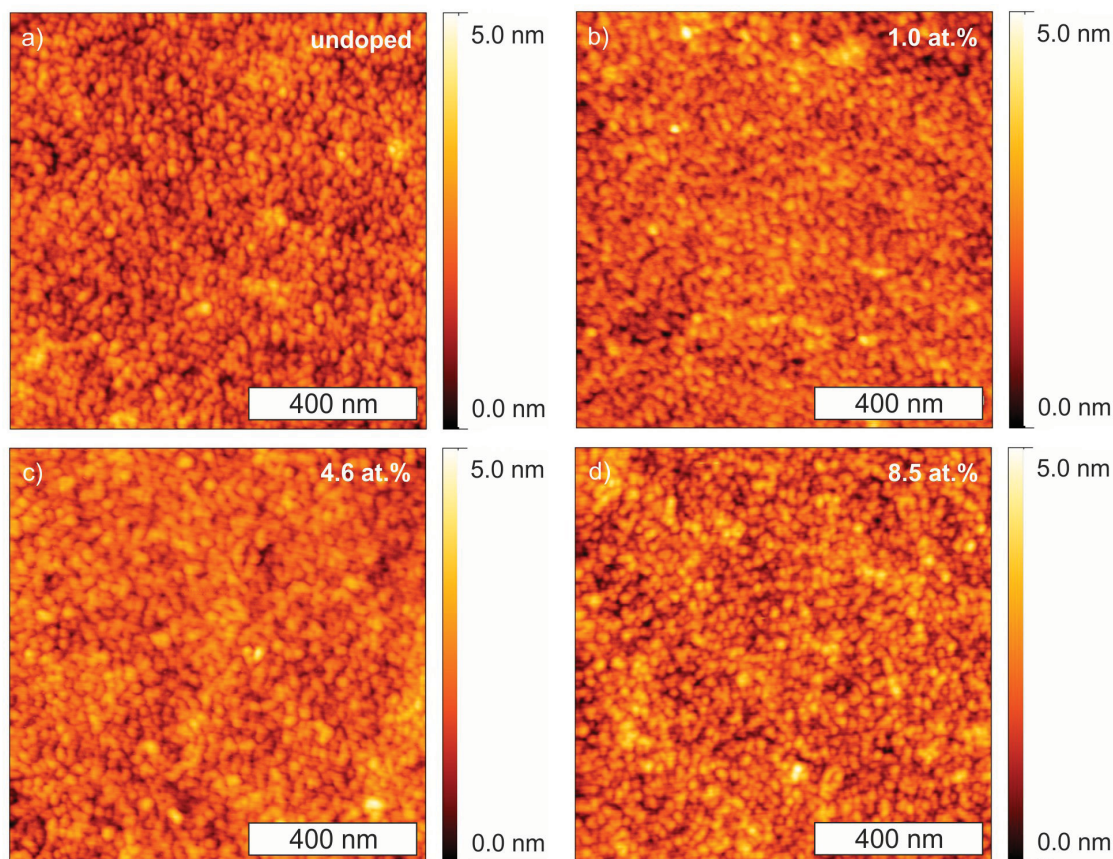
Figure 5.9: *AFM analysis of undoped and doped ta-C layer after protein adsorption. The undoped sample is shown in (a). The remaining samples were doped with 1 at.% (b), 5 at.%(c) and 9 at.% (d) silver ions. The ions' implantation energy was 1 keV. The protein concentration was c = 10 μg/ml.*
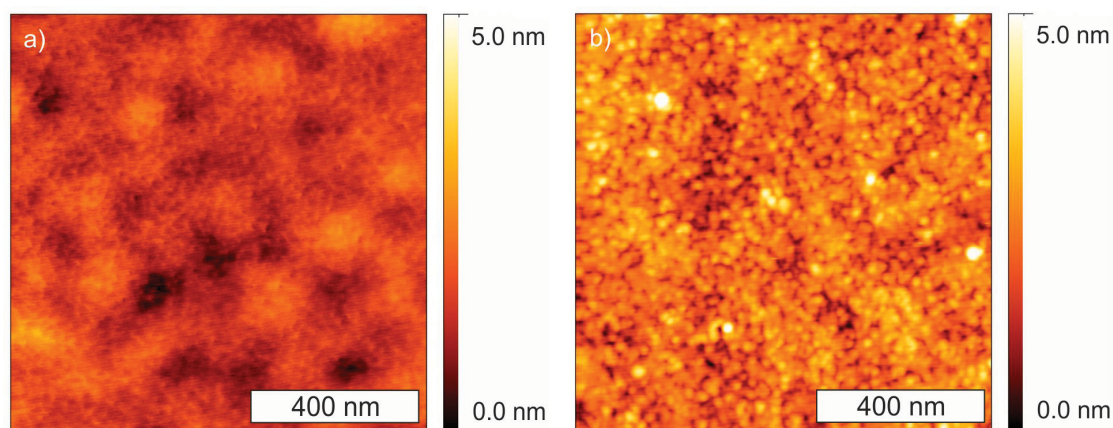
Figure 5.10: *AFM analysis of Ti doped ta-C layer before (a) and after (b) protein adsorption. The titanium concentration was 5 at.% and the dopant layer was in a depth of (1.9 ± 1.4) nm (maximum ± FWHM). The protein concentration was c = 10 μg/ml.*

5.4 Summary and Conclusions

In this chapter, the influence of the surface chemical composition on the adsorption behavior of HPF was investigated.

In the first part of this chapter, protein adsorption experiments were carried out on well known substrates such as Si and TiO_2. The concentration of HPF within the PBS solution was about $c_{HPF} = 10$ μg/ml. It was observed, that HPF forms a dense protein film on both substrates causing an increase of the RMS roughness of $\lesssim 0.2$ nm to $\lesssim 0.5$ nm. A reduction of the HPF concentration to $c_{HPF} = 1$ μg/ml enabled the investigation of single proteins. Molecules that mostly adsorbed in a trinodular structure were observed for silicon. Some networking was visible, indicating that silicon tends towards a hydrophobic character, which was in good agreement with preceding contact angle measurements ($\Theta_{Si} = (84.5 \pm 4.6)°$). TiO_2 revealed a more hydrophilic character ($\Theta_{Ti0_2} = (60.9 \pm 3.2)°$), as proteins in trinodular and globular conformations were observed. The dimensions of single proteins were measured. HPF molecules in trinodular conformation had a length of 50 - 55 nm and a height of 0.6 - 0.9 nm, whereas proteins in globular conformation have a diameter of ≈ 22 nm and a height of ≈ 1.3 nm. Hence, the difference concerning their hydrophobicity was visible in the adsorption behavior of HPF.

The second part concentrated on the influence of the sp^3 content of carbon based substrates. It was shown, that HPF forms coarsely meshed nets on the hydrophobic ($\Theta_{HOPG} = (97.4 \pm 6.2)°$) HOPG. When increasing the sp^3 content up to $\gtrsim 70\%$ (ta-C), a dense film is visible again. This is consistent with a decrease of the contact angle down to ($\Theta_{ta-C} = (70.2 \pm 0.6)°$). Variations concerning the adsorption density were observed concerning different sp^3 contents, but it is not perfectly clear whether this was an effect of the surfaces' chemistry or their topographies, as the investigated samples differ in their roughness. The differences in their roughness originated from the deposition process: different ion energies were necessary to vary the sp^3 content.

The last part of this chapter dealt with the change of the surface chemistry by doping. Simulations were carried out in order to gather information about the implantation profile. The successful implantation of silver ions in ta-C was verified via XPS measurements. Simulations gave information about the fluencies that are necessary to obtain certain dopant concentrations. A direct comparison of TRIM and TRIDYN simulation

for different dopants having the same ion energy emphasized the importance of the simulation program choice. Due to sputtering with low ion energies, the maximum of the implantation profile is shifted about half a nanometer closer to the surface. This shift is crucial for the surface's properties. While TRIDYN simulates the implantation profile dynamically by taking sputter effects into account, TRIM does not. A set of ta-C samples were doped with different concentrations of silver ions according to TRIDYN simulations. The obtained samples were characterized via AFM. No changes in the surface roughness, which was about ≈ 0.2 nm were observed for silver concentrations up to $c_{Ag} = 4.6$ at.%. For higher silver concentrations of $c_{Ag} = 8.5$ at.%, the roughness increased to ≈ 0.5 nm, which might originate from clustering of the dopants within the ta-C matrix. For further experiments, it might be of interest to analyze a cross section lamella of the sample by transmission electron spectroscopy (TEM), in order to look for silver clusters.

Finally, adsorption experiments were carried out on silver doped ta-C layers. On all samples, HPF seemed to form a homogeneous film, independently of the dopant's concentration. Doping of ta-C with 5 at.% titanium in an implantation depth of ≈ 2 nm also had no significant influence on the adsorption behavior of HPF.

In summary, different surface chemistries have an effect on the adsorption behavior of HPF, as was shown for silicon, titanium dioxide and HOPG. Nevertheless, chemical changes of the surface caused by ion beam radiation such as a variation of the sp^3 content of ta-C layers or doping seem to have no major impact, at least not within the boundaries of the performed experiments. Surface roughness appears to have greater influence on the adsorption behavior of proteins.

6 Protein Adsorption on Rippled Surfaces

After investigating the influence of a surface's chemistry on the adsorption behavior of HPF, this chapter describes investigations on its dependency on the surface's topography. For this purpose, ripple structures with varied wavelengths were created on silicon, titanium dioxide and, for the first time, tetrahedral amorphous carbon via low energy (less than 20 keV) ion beam irradiation. The experiments were done in cooperation with Jessica Richter (diploma thesis) [Hön10], Maria Fravventura (master thesis) [Fra09], Stefanie Eckner (bachelor thesis) [Kos11], Alexander von Müller (master thesis) [vM14] and Dr. Thomas Keller, Christian Helbing, as well as Dr. Robert Schulze from the Institute of Materials Science and Technology (IMT), FSU Jena. Parts of this work are published in Sommerfeld et al. [Som12]

6.1 Silicon

The protein adsorption was carried out according to the procedure presented in chapter 3.2. The HPF concentration was 10 μg/ml, which was sufficient for a full surface coverage. In Figure 6.1 an overview is given for Si with varying ripple wavelengths, after the adsorption process. On the left side, the AFM height images give information concerning the possible conformation of the proteins. The continuous lines through the images indicate the position of the cross section measurements, to be seen on the right side of Figure 6.1. By comparison with Figure 4.12, it becomes clear that the backbones of the ripples have an irregular shape, which is caused by the adsorbed proteins. For ripple structures with long wavelengths ($\lambda = 146$ nm), as shown in Figure 6.1(a, b), a globular conformation of the adsorbed proteins is observed. This is comparable to the situation for flat surfaces that was presented in chapter 5.1. Consequently, surface pattern, which appear smooth when compared to the size of the proteins have no influence on the adsorption behavior. However, significant changes appear when the ripple wavelength approximates to the range of the protein's size. When the wavelength is as low as $\lambda \approx 68$ nm (see Figures 6.1(c, d)), the fibrinogen molecules adsorbed in a stretched conformation, apparently parallel to the orientation of the ripples. A perpendicular orientation of HPF to the ripple backbones on Si arises when the ripple wavelength is decreased even more down to $\lambda \approx 52$ nm (Figure 6.1(e, f)).
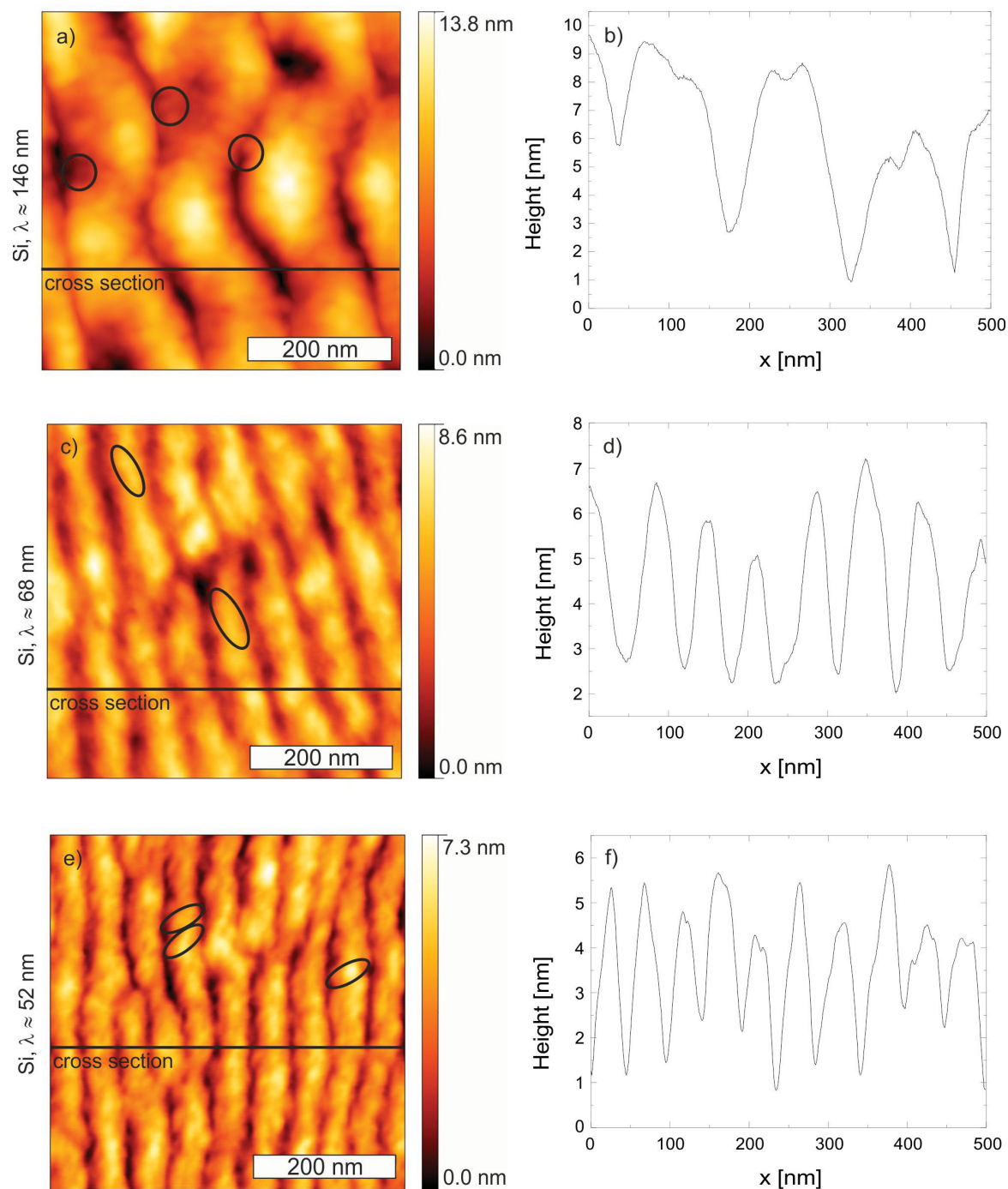
Figure 6.1: *AFM analysis of rippled Si with varying wavelengths after protein absorption (left column) and the corresponding cross sections (right column) along the continuous line. HPF adsorbed in a globular conformation for long ($\lambda = 146$ nm) wavelength Si ripples (a+b). For a shorter wavelength ($\lambda = 68$ nm) of the Si ripples, HPF adsorbed in a stretched conformation along the ripple backbones (c+d). For the shortest wavelength investigated ($\lambda = 52$ nm), the HPF still adsorbed in stretched conformation but with an orientation across the ripple backbones (e+f).*

Particular attention should be given to the selective place of adsorption on the rippled structures. In the case of protein attachment only in the valleys or spread over the entire area, a decrease or no change at all of the amplitude should have occurred, but this was

not the case. Apparently, the proteins solely adsorbed on top of the hills, not in the valley. In fact, an increase of about 1.1 - 1.6 nm of the ripple amplitudes was detected in Figure 6.1a, which is in the range of the proteins' height (compare with chapter 2.3).

As mentioned above, the used HPF concentration was sufficient for a full surface coverage. Thus, the molecules can connect with each other, as shown for the flat substrates in chapter 5.1. In the case of Si, end-to-end interactions of the proteins lead to weakly bonded protein networks. When introducing a nanostructure on a surface, the protein networks cannot muster stable bindings. These findings indicate that the adsorption of single proteins on ripple structures with long wavelengths ($\lambda > 100$ nm) basically relies on the surface chemistry. This is plausible as the aspect ratio (wavelength/amplitude) is rather large and therefore comparable with flat surfaces. The experiments showed a globular conformation of HPF molecules on Si with long wavelengths (see Figure 6.2, left side) with folded α chains underneath the domains. These investigations concur with the work of Tunc et al. on SiO_2 [Tun05]. The theoretical findings for the adsorption of synthetic oligomers, [Mel10] suggest that the adhesion of the proteins on the nano-rippled surfaces might be decreased when a curvature appears that is within the size of the protein. Hence, it can be presumed that by increasing the surface curvature (smaller wavelength) for Si, the adsorption energy is decreased. Therefore, it is energetically favorable for the proteins to stretch. By doing this, the contact area between substrate and protein is increased assuring adsorption. This theory agrees with the findings by Rasmusson et al. [Ras94] and Roach et al. [Roa06] for the adsorption of HPF on polymer nanostructures and silica nanospheres. The latter for instance showed that fibrinogen actually wraps itself around surfaces that are curved in the nanometer-scale.

The dependency of the orientation of the proteins on the ripple wavelength can be explained as follows: for large wavelengths, the adsorption takes place along the ripple backbones (see Figure 6.2, middle). The situation changes when the wavelength is decreased and thus the curvature is increased. In this case, the required optimization of the adsorption energy is only possible by additional protein-protein interaction. This eventually results in an alignment of the proteins across the ripple backbones, which increases the contact area between neighboring proteins, as is illustrated in Figure 6.2 (right side). Protein-protein interaction leading to an increased surface coverage is also described in [Roa05].

In order to explain the observation that proteins adsorbed only on the ridges of the rip-

ples, one can propose the following model: Due to the experimental process, proteins approach the range of the surface potential of the backbones first and start to adsorb there. According to Siegismund et al. [Sie10], the migration probability for directions combining HPF molecules is higher than that for isolating molecules. Thus, adjacent proteins adsorb around the backbones leading to coverage on top of the ripple backbones only.
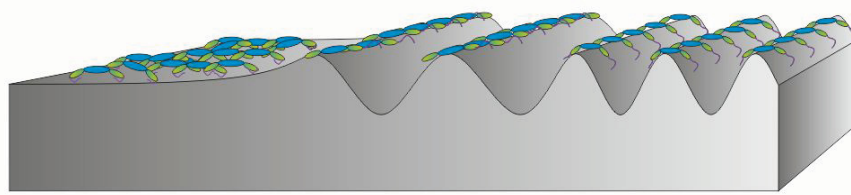
Figure 6.2: *Sketch of the possible formation HPF can engage on a rippled surface for varied wavelength. The adsorption of single proteins on ripple structures with long wavelengths (λ > 100 nm, left side of the image) basically relies on the surface chemistry. The proteins adsorb in a stretched formation when the surface curvature increases (λ < 100 nm, right side of the image). Their orientation on the backbones of the ripples changes from parallel to perpendicular for the smallest wavelengths which are in the range of the protein's diameter. Note, the height is not to scale!*

For a more precise analysis a new set of rippled silicon samples was synthesized and the adsorption experiments were repeated. Figure 6.3 shows a detailed study of one of the samples before and after protein adsorption.

The sample was irradiated with 5 keV xenon ions, 70° tilted towards the ion beam direction. The fluence was $6.8 \cdot 10^{16}$ cm^{-2}. Figure 6.3a shows the referring height picture before the adsorption experiments. The created ripples have sharp features and their wavelength was determined to be λ = (48.0 ± 5.1) nm. The amplitude was A = (4.0 ± 1.4) nm. After the protein adsorption, the height image (b) shows, that the ripples are homogeneously covered with HPF molecules. The ripples' features are slightly blurred and zooming into the picture makes it possible to see individual proteins (see inset). The proteins' orientation seems to be perpendicular to the one of the ripples, which is emphasized by determining the dimensions of single proteins (elliptical marking within the inset of b). On average, the marked proteins have a length of ≈ 53 nm and a width of ≈ 29 nm, which fits well with the results presented in chapter 5 for single proteins on flat silicon. The error of these measurements is in the range of the tip's dimension, which is about 7 nm. Cross sections across the ripples were taken along the horizontal lines and are presented in Figure 6.3c and d.
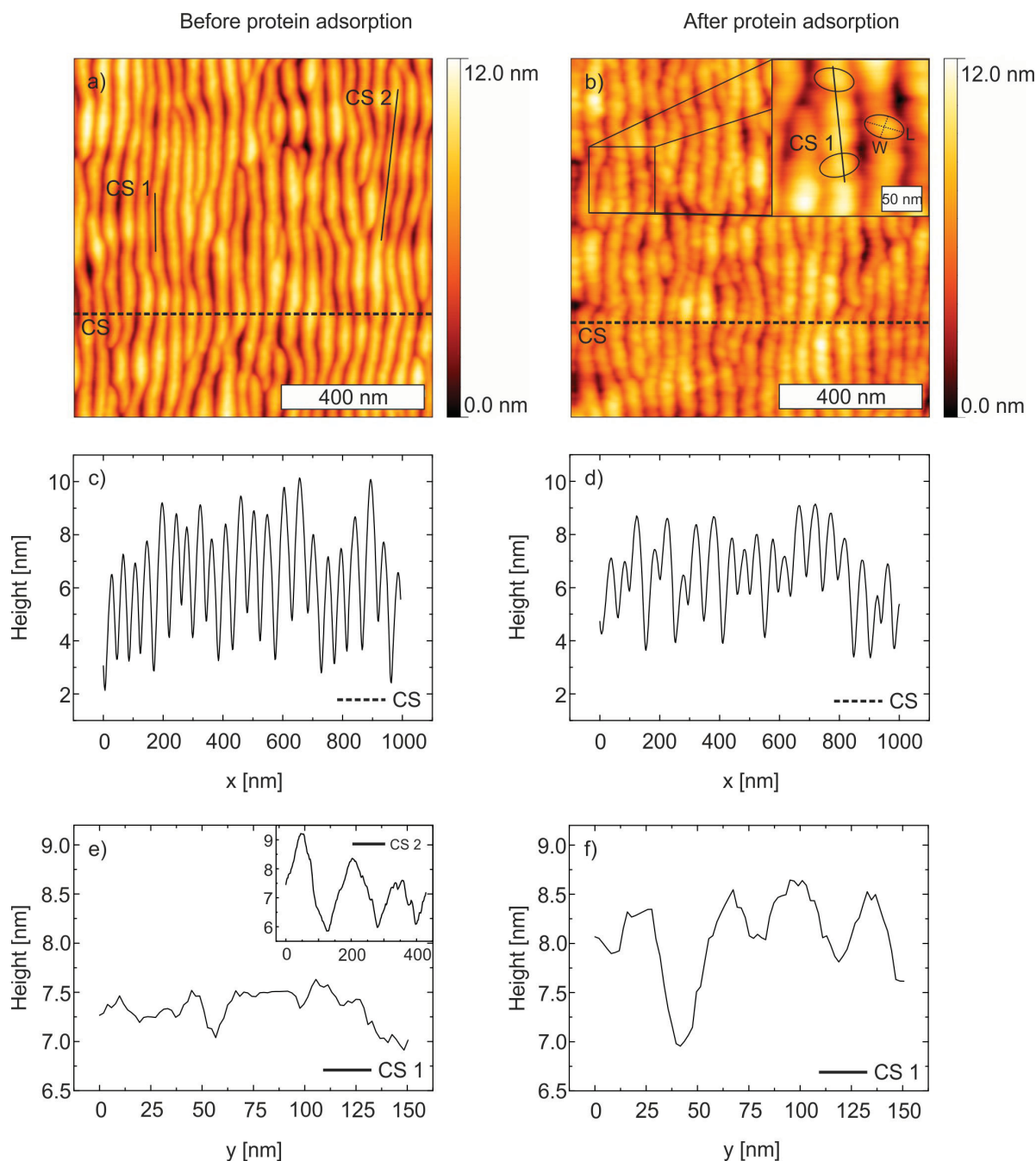
Figure 6.3: *AFM height pictures (a + b) of rippled silicon before and after proteins adsorption show a clear difference in appearance. The zoom shown in the inset emphasizes some proteins by an ellipse. Their length along the long axis correlates well with the dimension of single HPF molecule (see chapter 5). Cross sections were taken across (c and d) and along (e and f) the ripples, in order to show the difference before and after the protein adsorption.*

It is apparent that the amplitude of the ripples is decreased to A = (1.7 ± 0.8) nm after the protein adsorption. This seems to be in contradiction with the results presented in Figure 6.1, but does not necessarily mean that proteins exclusively adsorbed in the valleys. On the contrary, the wavelength of this sample is smaller than the one shown above. This leads to a very dense packing of the proteins, which made it impossible for the tip to actu-

ally reach the valleys of the ripples, causing a decrease of the amplitude. This assumption is emphasized by an apparent increase of the wavelength to $\lambda^* = (57.0 \pm 5.8)$ nm[1], which is possible by overlapping of proteins. Additionally, cross sections were taken along the ripples (e and f). Before the protein adsorption, the ripple backbones are rough but do not show any periodic patterns that can be associated with proteins. Note, when investigating a longer distances (inset of e), bigger pattern become apparent showing inhomogeneity along single ripples, which were not noticed before. Figure 6.3f shows a cross section along a ripple (see according marking in b) after the protein adsorption. In comparison to e) periodic patterns with horizontal dimensions (20 - 30 nm) are visible. They match the proteins very well. The height cannot be related to the height of the proteins because it is not possible to distinguish between the top of the layer and the bottom of a protein. Nevertheless, this detailed AFM analysis supports the suggested model of the perpendicular orientation of the HPF molecules on surface curvatures, which have equal dimensions.

6.2 Titanium Dioxide

Figure 6.4a shows an AFM height picture of TiO_2 with a ripple wavelength of $\lambda = 125$ nm after the adsorption process. The markings indicate some of the proteins that adsorb in globular conformation. Again, it can be assumed that the α chains attach to the surface and shield the hydrophobic D and E domains, which are piling up on top resulting in a globular assembly of HPF. This concurs with the findings by Van de Keere et al. [Kee08] on (flat) Ti substrates with TiO_2 surfaces. The adsorption behavior of single proteins on rippled TiO_2 with long wavelengths ($\lambda > 100$ nm) equals the one Si shows. When increasing the surface curvature (smaller wavelength of $\lambda \approx 52$ nm), no protein adsorption could be observed (see Figure 6.4b). The HPF height image after the protein adsorption entirely resembles the image before the adsorption process. The lack of adsorbed proteins on rippled TiO_2 with wavelengths in the range of the protein's diameter might be caused by the adsorption energy of TiO_2 being more decreased than the one on rippled Si.

---

[1]This wavelength does not refer to the actual wavelength of the ripples underneath the protein film, but to the number of observed ripples per length.
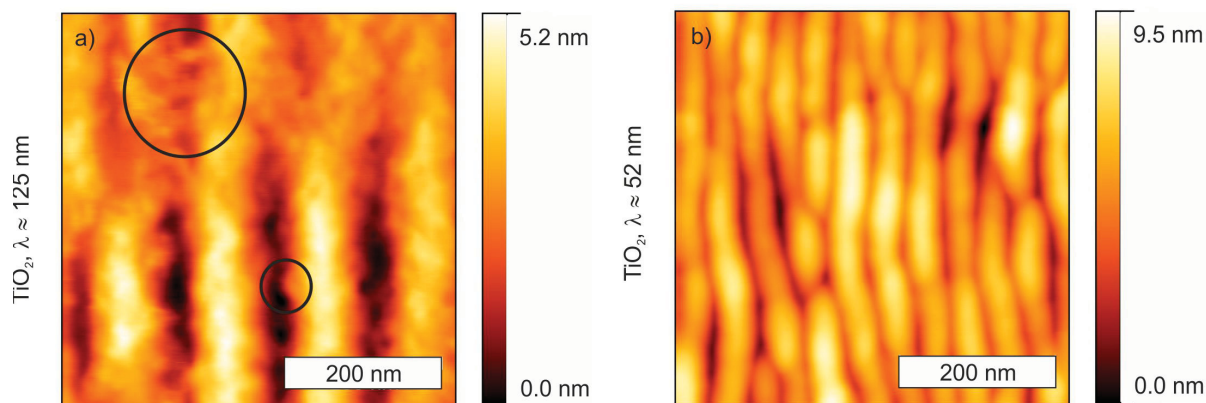
Figure 6.4: *AFM height analysis of rippled TiO$_2$. The proteins adsorb in a globular conformation on long-wavelength ripped TiO$_2$ (a); whereas, no adsorption was observed on ripple structures with short wavelength (b).*

As a consequence, the adsorption behavior of HPF does not seem to rely exclusively on the surface chemistry. A change of the substrate topography has a major impact on the protein attachment to a substrate. This theory is further supported by the fact that an increased water contact angle for TiO$_2$ with short wavelengths was found, which therefore has a more hydrophobic character. According to the findings by other groups, HPF should adsorb more strongly on this hydrophobic surfaces because of the chemistry of the surface. [Sit99, Tun05] Since this was not the case, the lack of observed proteins can be interpreted as a result of the local surface curvature.

6.3 Tetrahedral Amorphous Carbon

As described in chapter 4.2.2., silicon samples were created, and afterwards a thin film (less than 10 nm) of ta-C was deposited onto the ripples. The adsorption experiments were conducted as described before. The concentration of HPF within the PBS solution was 10 μg/ml.

Figure 6.5 shows the AFM height pictures after the protein adsorption for four wavelengths, initially ranging from $\lambda = (55.0 \pm 6.4)$ nm to $\lambda = (131.2 \pm 18.0)$ nm. Apparently, all samples seem to be homogeneously covered with a HPF film. No dependency of the adsorption behavior on the ripple wavelength is visible.
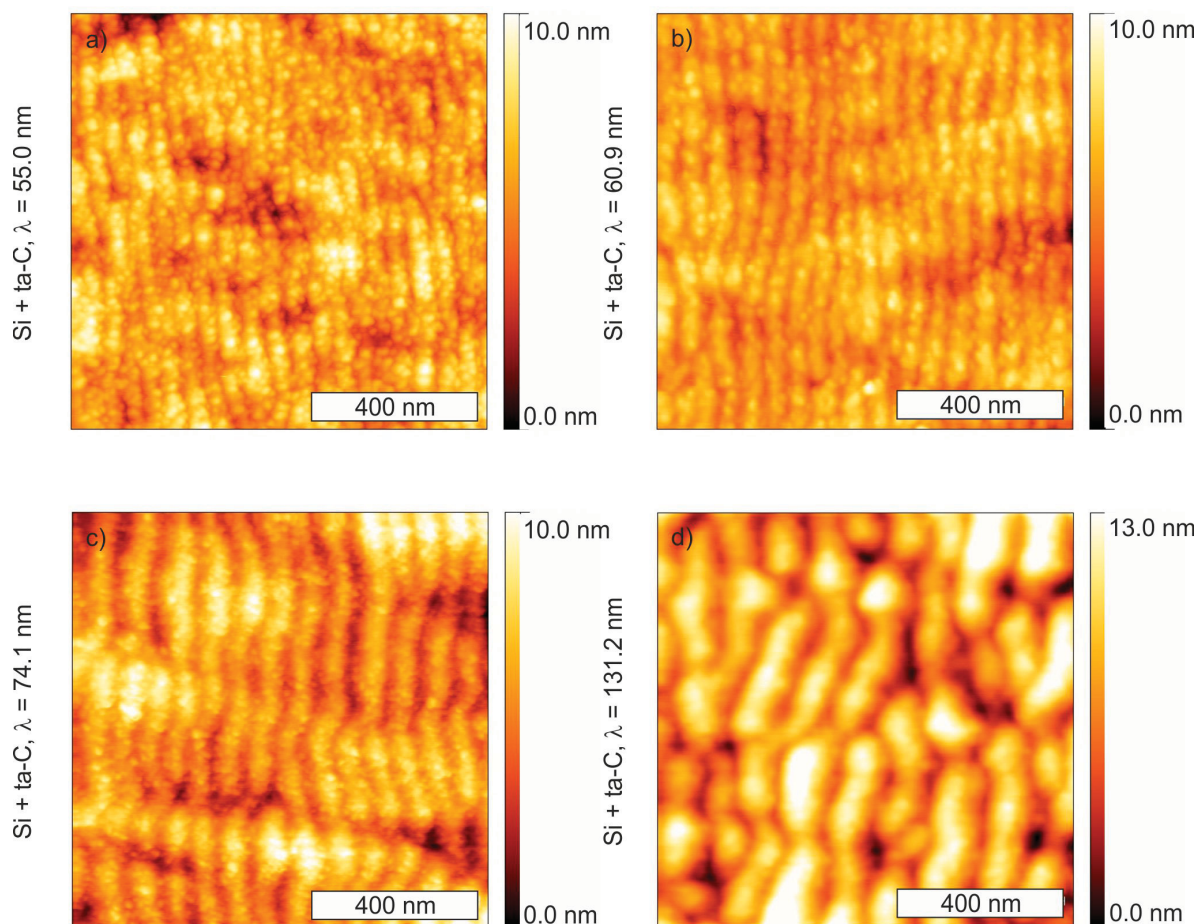
Figure 6.5: *AFM height analysis of rippled silicon, covered with ta-C. The ripple wavelengths ranges from $\lambda = (55.0 \pm 6.4)$ nm (a), over $\lambda = (60.9 \pm 4.0)$ nm (b) and $\lambda = (74.1 \pm 5.7)$ nm (b) to $\lambda = (131.2 \pm 18.0)$ nm (d). The HPF molecules form a homogeneous film on each sample.*

Furthermore, there is no definite change in the ripples' amplitude before and after the protein adsorption, as plotted in Figure 6.6a. It can be deduced that the proteins adsorbed on the hills as well as in the valleys. Figure 6.6b shows that there is also no change in the ripples' wavelength (λ^*). Slight discrepancies might occur due to bridging of some proteins over two ripple backbones, but they are included in the errors. Also, more agglomerations were observed. Both effects could contribute to this minor increase in the wavelength.
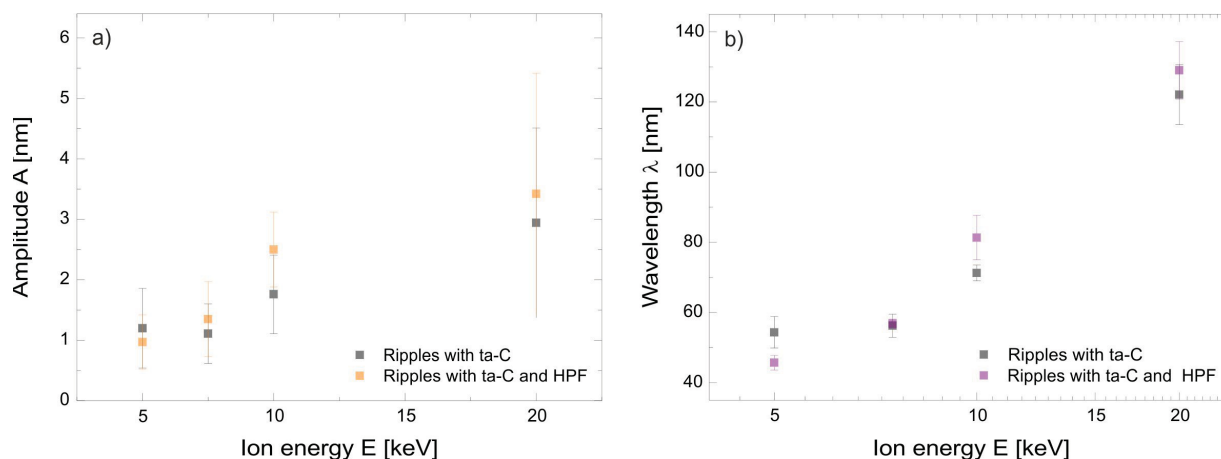
Figure 6.6: *Investigation of the amplitude (a) and wavelength (b) of ta-C ripple structures before and after proteins adsorption. No significant changes could be found for both characteristics.*

A closer look was taken on the sample with the smallest wavelength in order to check for signs of alignment, as is shown in Figure 6.7. The height picture before the protein adsorption is shown in Figure 6.7a. The ripples have less sharp features in comparison to silicon ripples which is caused by the ion beam induced ta-C coverage. The wavelength of the presented sample was $\lambda = (55.0 \pm 6.4)$ nm and the amplitude was A = (1.2 ± 0.7) nm. The according cross section, which is marked within a), is presented in c). In comparison to ripples just on pure silicon, the ta-C covered ripples are less homogeneous concerning their height and local wavelength. After the protein adsorption, the ripples are covered with HPF molecules as is shown in Figure 6.7b. It is apparent that they are less aligned than the ones observed on silicon ripple surfaces. The inset shows a zoom into the AFM image. It is much more difficult to distinguish between different proteins. The domains of two proteins were found and marked accordingly. Unfortunately, the contrast to the underground was too little in order to determine the dimensions of the lower proteins. The upper protein has a length of ≈ 60 nm and a width of ≈ 21 nm. The error of these measurements is in the range of the tip's dimension, which is about 7 nm. Both identified proteins seem to be aligned rather along the ripples, not across, which could be due to the higher wavelength compared to the proteins on the silicon sample with the smallest wavelength. In Figure 6.7d, a cross section taken across the ripples after the protein adsorption is presented. In the case of ta-C ripples, the difference between before and after protein adsorption is not so crucial. The amplitude is only decreased to A = (1.0 ± 0.5) nm after the protein adsorption, which is well within the range of error of the amplitude A = (1.2 ± 0.7) nm before the protein adsorption. One might assume that this is due to the larger wavelength in comparison to the silicon ripples, allowing the

proteins to adsorb also in the valley, but it is also possible that here the HPF film is too dense in order for the AFM tip to reach the valley of the ripples.
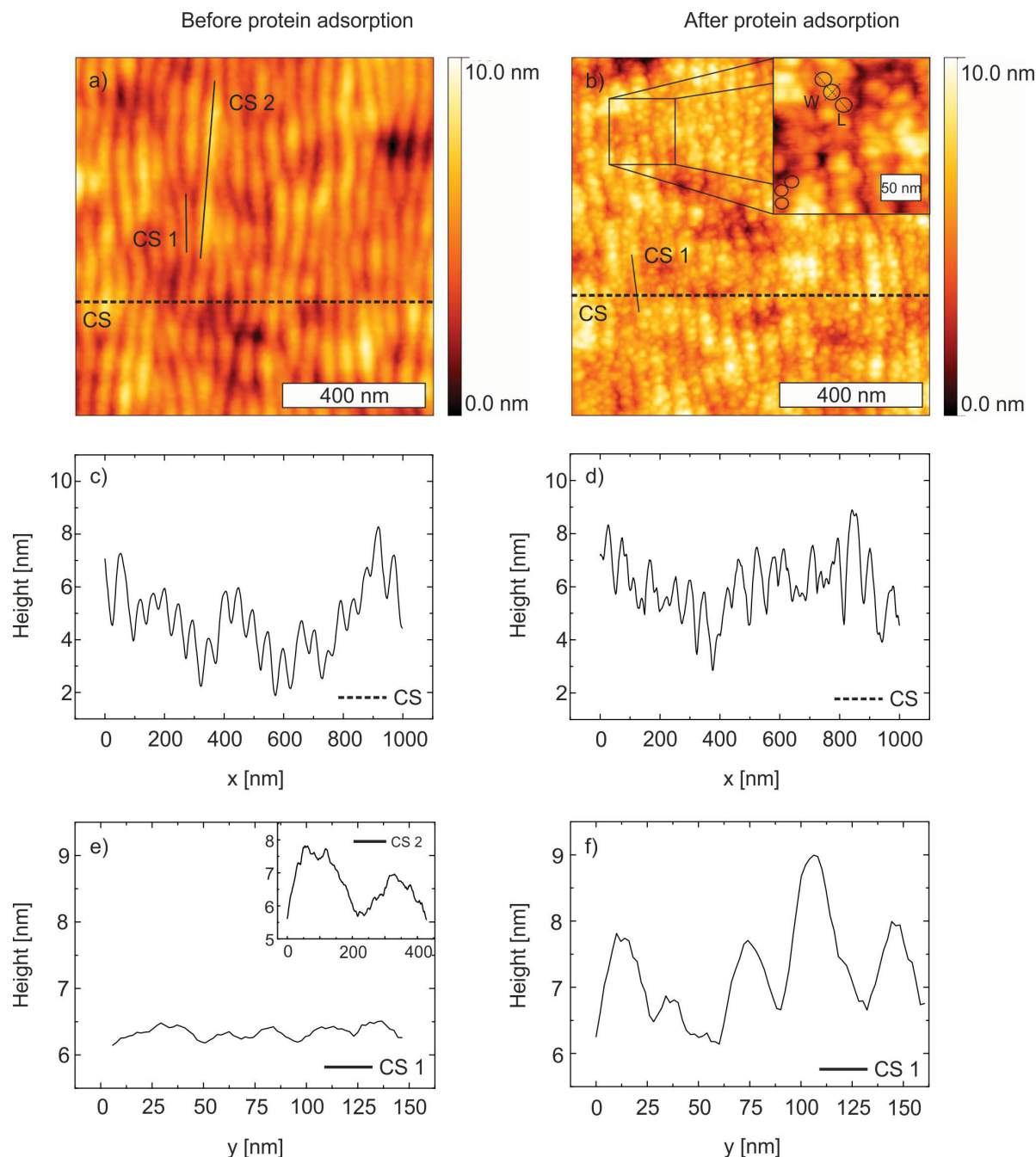
Figure 6.7: *AFM height pictures (a + b) of rippled silicon, covered with ta-C before and after protein adsorption show a clear difference in appearance. The zoom shown in the inset reveals less alignment of single proteins, which makes it difficult to distinguish between individual molecules. Nevertheless, the domains of two proteins were marked. Cross sections were taken across (c and d) and along (e and f) the ripples, in order to emphasize the difference before and after the protein adsorption.*

For the ta-C ripples no change of the wavelength $\lambda^* = (55.0 \pm 8.2)$ nm was observed. Thus, there might be less overlapping of proteins on neighboring ripples. The cross sec-

tions taken along the ripples (e and f) emphasize the difference between before and after the protein adsorption as according periodic patterns are visible only after the adsorption. Regarding rippled ta-C there are also hints that the proposed adsorption model applies because single molecule orientate themselves along the ripple backbones. Note: the majority of the proteins seems to adsorb randomly, which might be caused by the different ripple substrate. This assumption is strengthened when comparing several cross section taken along the ripples of HPF covered silicon and ta-C, as presented in Figure 6.8. The measurements were taken on the samples with the smallest wavelength, presented in Figure 6.3b (Si) and Figure 6.7b (ta-C). The peaks on silicon (a) have an average width of ≈ 35 nm. This is too small to fit the length of a protein. Considering the width of the tip (≈ 7 nm), it might be that the observed width refers to the width of a protein. In this case, one might assume that the proteins are aligned perpendicularly along the ripples. Slight rotation of the HPF towards the ripple edge could contribute to the observed broadening of the width. Figure 6.8b shows three cross sections taken along ta-C ripples with HPF on top. The widths (≈ 13 - 43 nm) and heights of the individual peaks vary quite strongly indicating a less organized adsorption of HPF on ta-C ripples.
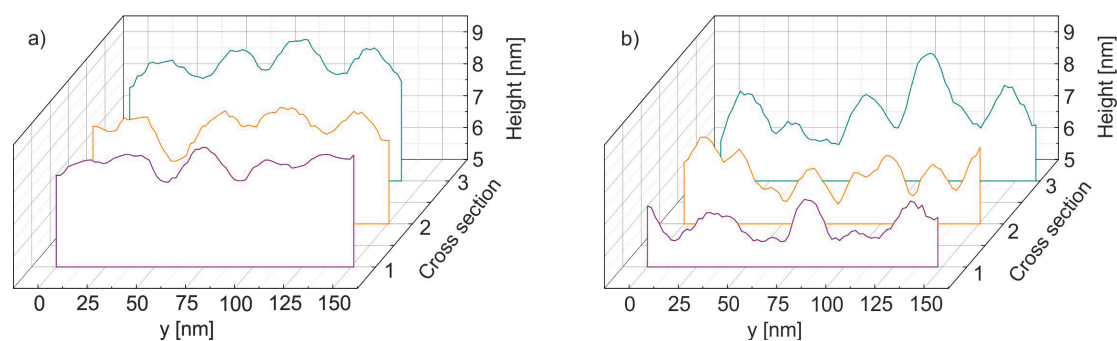
Figure 6.8: *Comparison of three different cross sections taken along silicon (a) and ta-C (b) ripples with adsorbed proteins. The samples with the smallest wavelength were investigated in both cases. The average peak width for the cross sections on Si (a) is ≈ 35 nm. The peak width for the cross sections on TiO_2 (b) ranges between (≈ 13 - 43 nm).*

6.4   Summary and Conclusions

This chapter focused on the influence of a substrate's topography on the adsorption behavior of HPF.

The first part presented results that were obtained from adsorption experiments, carried out on rippled silicon and titanium dioxide surfaces. The ripples' wavelengths ranged from 45 - 146 nm. AFM investigations were performed on rippled silicon after the protein adsorption. The obtained height pictures showed that HPF adsorbs well on rippled silicon. Additionally, cross sections indicate that HPF molecules arrange themselves exclusively on the backbones of the ripples. It appears that structures with diameters far exceeding the dimensions of the investigated molecules have little influence on the adsorption behavior of HPF. They do not differ from untreated, totally flat substrates. However, when the ripple wavelength becomes comparable to the dimension of the protein of interest, an influence is visible. HPF tends to adsorb in such a way that protein-protein interactions are promoted in order to attach to the surface although the adsorption energy is decreased by the increased curvature of the surface. Proteins arrange themselves along/across the ripples. This was verified by a detailed AFM analysis of the sample with the smallest wavelength.

In the case of TiO_2 the adsorption of HPF is not influenced by ripple structures with long wavelengths (≈ 125 nm), but no adsorbed proteins could be found for small wavelengths (≈ 52 nm). Apparently, the surface energy of the rippled TiO_2 with short wavelengths around ≈ 50 nm is reduced in a way that makes it impossible for the HPF molecules to adsorb strongly enough on the surface.

The second part concentrated on the adsorption of HPF on ta-C ripples with wavelengths ranging from 55 - 131 nm. It was shown that the proteins adsorb homogeneously, independently of the ripple wavelength. A detailed AFM analysis of the sample with the smallest wavelength showed there is hardly any alignment of the proteins. In the few cases alignment was observed, it seems to be along the ripples, not across, which might be due to the bigger wavelength in comparison to the silicon ripples. As no change concerning the ripples' amplitude was observed, the HPF molecules seem to adsorb in the valleys as well as on the tops of the ripples.

In conclusion, the results presented in this chapter show that the topography of substrates, such as silicon, titanium dioxide and tetrahedral amorphous carbon, has a significant influ-

ence on the adsorption of human plasma fibrinogen. Together, topography and chemistry of substrates are proven to show a variety of influences for how and if a biologically relevant molecule, such as HPF, adsorbs.

7 Summary and Outlook

The aim of this work was to investigate the influence of ion beam modification of surfaces on the adsorption behavior of biomedically relevant molecules. For this purpose, an ion accelerator, which is able to provide ion energies up to 30 keV and has a mass separation unit, was rebuilt, aligned and optimized. Regarding verification of the quality the obtained surfaces, the first part of this work dealt with ion beam modification of surfaces, in particular, the mass separated ion beam deposition of tetrahedral amorphous carbon (ta-C) layers and the formation of ion beam-induced ripple formations.

The influence of the deposition parameters, such as ion energy and fluence on the sp^3 content of the obtained ta-C layers, was analyzed in detail. XPS, Raman and AFM measurements were carried out in order to determine the layers' sp^3 content and their surface roughness. It was shown that a ta-C layer, which is synthesized with an ion energy of ≈ 500 eV contains a high sp^3 content ($> 70\%$) and is sufficiently smooth (less than 1 nm) for biocompatibility experiments. Also, film thickness measurements via SEM revealed that a deposition fluence of $7.4 \cdot 10^{17} cm^{-2}$ causes a film thickness of about 50 nm assuring a workable ta-C nanolayer.

Ion beam-induced ripples were created on Si and TiO_2 and the wavelength dependency of the ripples on the applied ion energy was investigated via AFM, confirming the common power-law dependency. Contact angle measurements were performed in order to investigate the topographical influence on the hydrophobicity. The following trends were observed: silicon becomes slightly more hydrophilic, whereas TiO_2 becomes more hydrophobic when a ripple structure is introduced. This effect can be attributed to the change of the samples' topography as no significant changes of the hydrophobicity were observed for irradiated, and yet flat silicon and TiO_2 samples in comparison to their un-irradiated, crystalline forms. No dependency on the ripple wavelength was observed within the ranges of error. XPS measurement supported the assumption that no stoichiometric changes are caused by ion irradiation. An influence of the stoichiometry on the measurements can thus be excluded.

Finally, silicon ripples with varied wavelengths were covered with a ta-C layer in order to obtain ta-C ripples. AFM measurements showed, that though there was no change concerning the wavelength of the ripples, their amplitude was significantly decreased by carbon ion deposition. TRIDYN simulations proved that the sputter yield of the samples

differ, depending on the samples' wavelength. The smaller the wavelength, the steeper the ripples' slope and thus, the higher the sputter yield, which caused a stronger diminution of the ripples' amplitude.

The biocompatibility of the surfaces was investigated by performing adsorption experiments with human plasma fibrinogen (HPF). This protein was chosen as it is well known for its ambiphilic character and its importance for the blood coagulation process. Due to the nanometer-sized dimension of a single HPF molecule and its fragility, AFM measurements were carried out for observations.

The second part of this work presented results concerning the adsorption behavior of HPF on flat, but chemically altered surfaces. For reference, adsorption experiments were carried out on silicon and titanium dioxide. The difference concerning their hydrophobicity was visible in the adsorption behavior of HPF. On silicon, the hydrophobic parts of HPF preferably adsorbed on the surface leaving the hydrophilic chains free to interact with each other and thus, forming networks. This networking was not observed on TiO_2, due to its more hydrohilic character. Adsorption experiments on strictly sp^2 bound, hydrophobic HOPG showed coarsely meshed nets of HPF. A dense film was visible on a ta-C layer indicating a more hydrophilic characteristic of the surface. Variations concerning the adsorption density were observed concerning different sp^3 contents, but it is unclear whether this was an effect of the surfaces' chemistry or their topographies as the investigated samples differ in their roughness.

The influence of various dopants on the adsorption behavior was also studied. Before experimentations, simulations were carried out. In order to gather information on the influence of doping effects, the simulation programs TRIM and TRIDYN were used to determine implantation profiles concerning various dopants, ion energies and fluencies. A direct comparison of both programs emphasized the importance of the program choice as TRIDYN simulates dynamically, which means it takes sputter effects into account. Based on the simulations results, extremely flat ta-C layers were doped with different concentrations of silver ions. The successful implantation of silver ions in ta-C was verified via XPS measurements and the obtained samples were characterized via AFM. On all samples, HPF seemed to form a homogeneous film independently of the dopant's concentration. This indicates that the biomedical impact of silver is limited to antibacterial and cytotoxic effects. An influence due to a reduction of the adsorption of proteins, which serve as medium between cells and substrate was not observed. Additional annealing of the

silver doped samples might be of interest as the silver ions might migrate even closer to the surface and, thus, have an influence. Doping of ta-C with titanium had no visible influence on the adsorption behavior of HPF, which experimentally confirmed studies by other groups. Additional oxygen or titanium dioxide ion doping may impact the bio-compatibility.

It would be interesting to investigate the influence of other dopants, such as fluorine and nitrogen. Next to oxygen, these dopants are known to have an influence on cell adsorption. Moreover, the dopants' concentration can be increased, exceeding 10 at.%. In order to determine the degree of coverage and the actual conformation of single proteins, smaller protein concentrations would be useful. Another interesting way to measure coverage would be the use of an oscillating crystal (quartz microbalance). In addition, the performed adsorption experiments ought to be extended to cells and bacteria.

The last part of this work focused on the influence of a substrate's topography on the adsorption behavior of HPF: Adsorption experiments were carried out on rippled silicon, titanium dioxide and ta-C surfaces with varied wavelengths. Structures with wavelengths that far exceed the dimensions of the investigated molecules (> 100 nm) have little influence on the adsorption behavior of HPF on all substrates. They do not differ from untreated, totally flat substrates. But when the ripple wavelength becomes comparable to the dimension of the protein of interest (< 100 nm), an influence is visible. This is in agreement with many other phenomena in the nano world, where critical processes occur when dimensions match. In the presented case, HPF seems to adsorb in such a way that protein-protein interactions are promoted in order to attach to the surface although the adsorption energy is decreased by the increased curvature of the surface. Proteins arrange themselves along the ripples, which was analyzed in detail for silicon and ta-C. The alignment was less intense for ta-C ripples, which could be an effect of the different surface chemistry. However, no proteins were observed on short-rippled TiO_2 indicating that its surface energy was reduced making it impossible for the proteins to stick to the surface. Ultimately, the topography of substrates, such as silicon, titanium dioxide and tetrahedral amorphous carbon, has a significant influence on the adsorption of human plasma fibrinogen.

As an outlook it would be interesting to obtain more information involving dynamics of the protein adsorption experiment; AFM measurements in the protein solution during the two hour adsorption time would be of interest. A silicon sample with a short wave-

length might be used as stamp pushed into a soluble gel. When performing liquid AFM measurements during the protein adsorption, the gel's structure becomes unstable. Thus, the ripple wavelength ought to change and its influence on the adsorption process should be visible *in situ*. Rippled HOPG and the adsorption of HPF on it would be valuable information to acquire. By performing according experiments, it would be possible to investigate whether a surface curvature interferes with the strong networking of fibrinogen, which was observed on flat HOPG.

In conclusion, this work presented results concerning possible modifications of biomedically relevant surfaces by ion beam irradiation and their influence on the adsorption behavior of biological molecules, such as proteins. Experiments were performed in order to change the substrates' chemistry and topography independently and to analyze their interaction with human plasma fibrinogen. The results indicate there is a codependency of the chemistry and the topography of a substrate concerning its influence on the biocompatibility. Hence, ion beam irradiation appears as an adequate tool to improve the biocompatibility of medically relevant materials (artificial replacements, stents etc.). Suggested extensions to the presented experiments might show whether there is some kind of critical curvature for individual substrates. Future research on already used and implemented biomaterials ought to concentrate more on possible topographical changes.

A   Appendix

A.1   Contact Angle Measurements

Figure A.1 exemplary shows contact angle measurement pictures for HOPG (a) and ta-C (b). A 5 - 8 μl droplet of Millipore water was carefully put on the samples. The laterally installed camera is focused on the resulting profile. The droplet's surface is approximated by a sphere, allowing the determination of the contact angle between droplet and sample surface. The latter is marked by a dashed, green line. The contact angle of HOPG was $\Theta_{HOPG} = (97.4 \pm 6.2)°$, which shows its hydrophobic character. For ta-C, which was synthesized with an ion energy of 1100 eV a contact angle of $\Theta_{ta-C} = (70.2 \pm 0.6)°$ was measured. Thus, it is more hydrophilic.
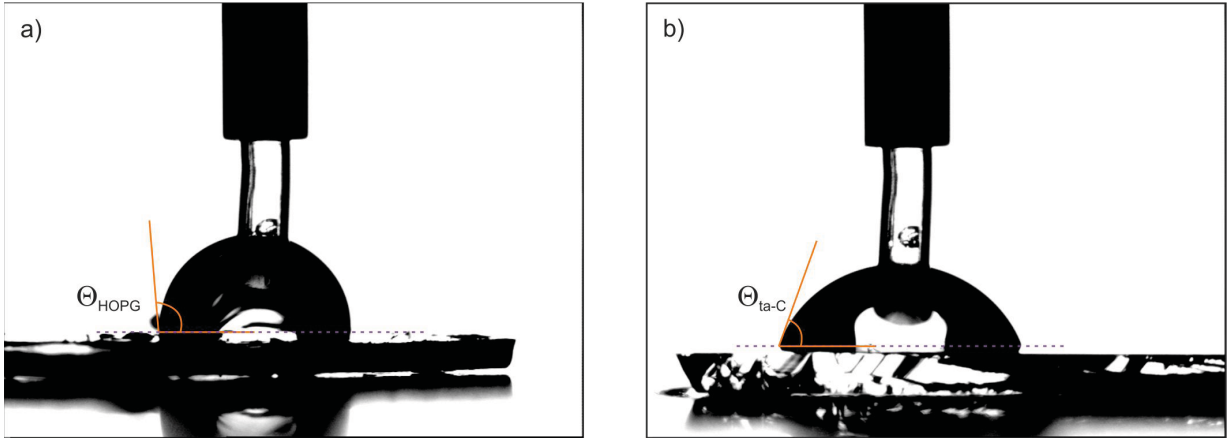
Figure A.1: *Contact angle measurements, exemplary shown for HOPG (a) and ta-C (b). The contact angle Θ is measured between the surface (green, dashed line) and the water droplet.*

A.2   Determination of the Ripple Amplitude

In order to determine the amplitude of the created ripples in a more objective way, a MatLab code was written in close cooperation with Alexander v. Müller and Jura Rensberg, as is subsequently presented. Note, the resolution of each AFM image is 512 x 512 lines. In case of a scan size of 1 μm, this equals a lateral resolution of about 2 nm.
First, the according AFM image (in grey scale and without any scaling information), the wavelength of the ripple structure, a value 'epsilon' and a value AnalysisRange' are entered. All amplitude values are directed to a funtion 'line', which is afterwards derivated. The extreme values of each line were determined within the while loop. A defined ('krit') area is cut around each extremum. This was done until the resulting vector 'DERIVATION' contains less than ten values. Second, the position and absolute value of each extremum was listed. Third, the amplitude difference between neighboring extrem values was computed. Finally, the average and standard derivation of the values for one line was determined. This process can be done for only one line, if 'AnalysisRange' corresponds to one line (1-512) or for the whole image, if 'AnalysisRange' is zero. In case of the latter, the calculation is done for every line and the average amplitude of each line is averaged for

the respective 'picture'. Care was taken during the AFM measurements that the ripples were vertically orientated for the measurements to avoid errors due to a deformation of the ripples' cross section and thus, cause a falsification of the ripple amplitude.

```
function [ output_args ]
= rippleamplitude (picture,lambda,eps,AnalysisRange)

if AnalysisRange>0
%code is computed for 1 line of the AFM image

AverageHeight=mean(mean(picture))
krit=round(lambda/4);
%defines area that is cut around the extrem values

for k=AnalysisRange:AnalysisRange
line=picture(k,1:512);
derivation=diff(line);
SIZE=size(derivation);
plot(line)

%within the while looo: extrem values are determined;
%area around these values is cut;
%this happens until vector 'DERIVATION' contains less than 10 values
Num=[1:512];
epsilon=0;
l=0;
DERIVATION=derivation;
while SIZE(2)>10 && epsilon < eps
    l=l+1;
    [x,y]=min((DERIVATION).^2);
    epsilon=x;
    RememberY(l)=y;
    important(l)=Num(y);
    %'important' refers to position of the zero point of the derivation
    Remember1=DERIVATION(1:RememberY(l)-krit);
    RememberNum1=Num(1:RememberY(l)-krit);
    Remember2=DERIVATION(RememberY(l)+krit:end);
    RememberNum2=Num(RememberY(l)+krit:end);
    Remember=[Remember1,Remember2];
    RememberNum=[RememberNum1,RememberNum2];
    DERIVATION=0;
    Num=0;
```

```
     DERIVATION=Remember;
     Num=RememberNum;
     SIZE=size(DERIVATION);
end


list=sort(important)
length=size(list);
Amplituden=0;
n=0;
for m=1:(length(2)-1)
     abst=round((list(m+1)-list(m))/3);
     if ((derivation(list(m)+abst))*(derivation(list(m+1)-abst)))>0
         n=n+1;
         Amplituden(n)=abs(line(list(m)+1)-line(list(m+1)+1));
     end
end


AverageAmplitude(k)=mean(Amplituden);


end


AVERAGE AMPLITUDE=mean(AverageAmplitude)


end



if AnalysisRange == 0
%code is computed for all lines of the AFM image
%mean amplitude favlues and errors of each line are averaged

AverageHeight=mean(mean(picture))
krit=round(lambda/4);
%defines area that is cut around the extrem values

for k=1:512
line=picture(k,1:512);
derivation=diff(line);
SIZE=size(derivation);

%within the while looo: extrem values are determined;
%area around these values is cut;
%this happens until vector 'DERIVATION' contains less than 10 values
Num=[1:512];
epsilon=0;
```

```
l=0;
DERIVATION=derivation;
while SIZE(2)>10 && epsilon < eps
    [x,y]=min((DERIVATION).^2);
    epsilon=x;
    RememberY(l)=y;
    important(l)=Num(y);
    %'important' refers to position of the zero point of the derivation
    Remember1=DERIVATION(1:RememberY(l)-krit);
    RememberNum1=Num(1:RememberY(l)-krit);
    Remember2=DERIVATION(RememberY(l)+krit:end);
    RememberNum2=Num(RememberY(l)+krit:end);
    Remember=[Remember1,Remember2];
    RememberNum=[RememberNum1,RememberNum2];
    DERIVATION=0;
    Num=0;
    DERIVATION=Remember;
    Num=RememberNum;
    SIZE=size(DERIVATION);
end

list=sort(important);
length=size(list);

Amplituden=0;
n=0;
for m=1:(length(2)-1)
    abst=round((list(m+1)-list(m))/3);
    if ((derivation(list(m)+abst))*(derivation(list(m+1)-abst)))>0
        n=n+1;
        Amplituden(n)=abs(line(list(m)+1)-line(list(m+1)+1));
    end
end

AverageAmplitude(k)=mean(Amplituden);
errorAmp(k)=std(Amplituden);
end

AVERAGE AMPLITUDE=mean(AverageAmplitude)
AVERAGE ERROR=mean(errorAmp)
end

end
```

A.3 Fibrinogen Adsorption on Irradiated, Flat Silicon and Titanium Dioxide

In Figure A.2 AFM height images are presented for flat silicon (a) and titanium dioxide (b) before protein adsorption. The samples were irradtiated with xenon ions under normal incidence. The ions' energy was 20 keV and the fluence was $\Phi = 5 \cdot 10^{16}$ cm^{-2}. After AFM characterizations, protein adsorption experiments were performed. The concentration of HPF within the solution was $c_{HPF} = 10$ μg/ml. Apparently, the proteins form a dense film on both substrates as can be seen in Figure A.2c and d.

Figure A.2: *AFM hight images of irradiated, yet flat silicon (left column) and titanium dioxide (right column). The upper row shows the smooth surface before protein adsorption, the lower row after. Apparently, the HPF molecules form a dense film on both substrates.*

List of Figures

List of Tables

Bibliography

[AF09]   A. Almaguer-Flores, R. Olivares-Navarrete, A. Lechuga-Bernal, L. Ximénez-Fyvie, and S. Rodil. Oral bacterial adhesion on amorphous carbon films. *Diamond Relat. Mater.* **18**, 1179 (2009).

[Agn04]   A. Agnihotri and C. A. Siedlecki. Time-dependent conformational changes in fibrinogen measured by atomic force microscopy. *Langmuir* **20**, 8846 (2004).

[Ais71]   S. Aisenberg and R. Chabot. Ion-beam deposition of thin films of diamondlike carbon. *J. Appl. Phys.* **42**, 2953 (1971).

[All01]   M. Allen, B. Myer, and N. Rushton. In vitro and in vivo investigations into the biocompatibility of diamond-like carbon DLC coatings for orthopedic applications. *J. Biomed. Mater. Res., Part B: Appl. Biomater* **58**, 319 (2001).

[And06]   M. Andara, A. Agarwal, D. Scholvin, R. A. Gerhardt, A. Doraiswamy, C. Jin, R. J. Narayan, C.-C. Shih, C.-M. Shih, S.-J. Lin, and Y.-Y. Su. Hemocompatibility of diamondlike carbonmetal composite thin films. *Diamond Relat. Mater.* **15**, 1941 (2006).

[Atz80]   V. Atzrodt, T. H. Wirth, and H. Lange. Investigation of NiSi and Pd_8Si thin films by AES and XPS. *Phys. Status Solidi A* **62**, 531 (1980).

[Bel90]   D. N. Belton and S. J. Schmieg. Electron spectroscopic identification of carbon species formed during diamond growth. *J. Vac. Sci. Technol., A* **8**, 2353 (1990).

[Bha98]   S. Bhattacharyya, C. Cardinaud, and G. Turban. Spectroscopic determination of the structure of amorphous nitrogenated carbon films. *J. Appl. Phys.* **83**, 4491 (1998).

[Bla90]   D. S. Blair, J. W. Rogers, and C. H. F. Peden. Potassium-assisted, facile oxidation of Si_3N_4 thin films. *J. Appl. Phys.* **67**, 2066 (1990).

[Boy95]   K. J. Boyd, D. Marton, S. S. Todorov, A. H. AlBayati, J. Kulik, R. A. Zuhr, and J. W. Rabalais. Formation of cn thin films by ion beam deposition. *J. Vac. Sci. Technol., A* **13**, 2110 (1995).

[Bra88]   R. M. Bradley and J. M. E. Harper. Theory of ripple topography induced by ion bombardement. *J. Vac. Sci. Technol., A* **6**, 2390 (1988).

[Bra12]   R. M. Bradley. Producing ripple topographies by ion bombardment with codeposition of impurities: A curvature-dependent sputter yield is not required. *Phys. Rev. B* **85**, 115419 (2012).

[Bra13]   R. M. Bradley. Nanoscale patterns produced by ion erosion of a solid with codeposition of impurities: The crucial effect of compound formation. *Phys. Rev. B* **87**, 205408 (2013).

[Cac00]   P. Cacciafesta, A. D. L. Humphris, K. D. Jandt, and M. J. Miles. Human plasma fibrinogen adsorption on ultraflat titanium oxide surfaces studied with atomic force microscopy. *Langmuir* **16**, 8167 (2000).

[Cai06]   K. Cai, J. Bossert, and K. D. Jandt. Does the nanometre scale topography of titanium influence protein adsorption and cell proliferation? *Colloids Surf., B* **49**, 136 (2006).

[Car96]   G. Carter, V. Vishnyakov, and M. Nobes. Ripple topography development on ion bombarded si. *Nucl. Instrum. Methods Phys. Res., Sect. B* **115**, 440 (1996).

[Car99]   G. Carter. The effects of surface ripples on sputtering erosion rates and secondary ion emission yields. *J. Appl. Phys.* **85**, 455 (1999).

[Cas13]   M. Castellino, V. Stolojan, A. Virga, M. Rovere, K. Cabiale, M. R. Galloni, and A. Tagliaferro. Chemico-physical characterisation and in vivo biocompatibility assessment of DLC-coated coronary stents. *Anal. Bioanal. Chem.* **405**, 321 (2013).

[Cha01]   E. Chanson, J. Erlebacher, M. J. Aziz, J. Floror, and M. Sinclair. Synamics of pattern formation during low-energy ion bombardment of Si(001). *Nucl. Instrum. Methods Phys. Res., Sect. B* **178**, 55 (2001).

[Che09a] N. Chekan, N. Beliauski, V. Akulich, L. Pozdniak, E. Sergeeva, A. Chernov, V. Kazbanov, and V. Kulchitsky. Biological activity of silver-doped DLC films. *Diamond Relat. Mater.* **18**, 1006 (2009).

[Che09b] H.-C. Cheng, S.-Y. Chiou, C.-M. Liu, M.-H. Ling, C.-C. Chen, and K.-L. Ou. Effect of plasma energy on enhancing biocompatibility and hemocompatibility of diamond-like carbon film with various titanium concentrations. *J. Alloys Compd.* **477**, 931 (2009).

[Chh97] M. Chhowalla, J. Robertson, C. W. Chen, S. R. P. Silva, C. A. Davis, G. A. J. Amaratunga, and W. I. Milne. Influence of ion energy and substrate temperature on the optical and electronic properties of tetrahedral amorphous carbon (ta-C) films. *J. Appl. Phys.* **81**, 139 (1997).

[Chh00] M. Chhowalla, A. C. Ferrari, J. Robertson, and G. A. J. Amaratunga. Evolution of sp^2 bonding with deposition temperature in tetrahedral amorphous carbon studied by raman spectroscopy. *Appl. Phys. Lett.* **76**, 1419 (2000).

[Chi09] T. K. Chini, D. P. Datta, and S. R. Bhattacharyya. Ripple formation on silicon by medium energy ion bombardment. *J. Phys.: Condens. Matter* **21**, 224004 (2009).

[Cui00] F. Cui and D. Li. A review of investigations on biocompatibility of diamond-like carbon and carbon nitride films. *Surf. Coat. Technol.* **131**, 481 (2000).

[Día96] J. Díaz, G. Paolicelli, S. Ferrer, and F. Comin. Separation of the sp^3 and sp^2 components in the c1s photoemission spectra of amorphous carbon films. *Phys. Rev. B* **54**, 8064 (1996).

[Dav93] C. A. Davis. A simple model for the formation of compressive stress in thin films by ion bombardment. *Thin Solid Films* **226**, 30 (1993).

[Dav98] C. A. Davis, G. J. Amaratunga, and K. M. Knowles. Growth mechanism and cross-sectional structure of tetrahedral amorphous carbon thin films. *Phys. Rev. Lett.* **80**, 3280 (1998).

[Doo84] R. F. Doolittle. Fibrinogen and fibrin. *Annu. Rev. Biochem.* **53**, 195 (1984).

[Dre92] M. S. Dresselhaus and R. Kalish. *Ion Implatation in Diamond, Graphite and related Materials*. Springer-Verlag (1992).

[Erd06] A. Erdemir and C. Donnet. Tribology of diamond-like carbon films: recent progress and future prospects. *J. Phys. D: Appl. Phys.* **39**, R311 (2006).

[Fen95] L. Feng and J. D. Andrade. *Proteins at Interfaces II: Fundamentals and Applications; ACS Symposium Series 602; Chapter 5*. American Chemical Society (1995).

[Fer00] A. C. Ferrari, A. Libassi, B. K. Tanner, V. Stolojan, J. Yuan, L. M. Brown, S. E. Rodil, B. Kleinsorge, and J. Robertson. Density, sp^3 fraction, and cross-sectional structure of amorphous carbon films determined by X-ray reflectivity and electron energy-loss spectroscopy. *Phys. Rev. B: Condens. Matter Mater. Phys* **62**, 11089 (2000).

[Fra09] M. C. Fravventura. *Ion-beam induced nanoscale ripples on Si, TiO_2 and Ti surfaces*. Master's thesis, Politecnico di Milano (2009).

[Fu05] Y. Fu, H. Du, S. Zhang, and W. Huanga. Xps characterization of surface and interfacial structure of sputtered tini films on si substrate. *Mater. Sci. Eng. A* **403**, 25 (2005).

[Gei07] A. K. Geim and A. H. MacDonald. Graphene: Exploring carbon flatland. *Phys. Today* **60**, 35 (2007).

[Ger02] I. Gerhards, C. Ronning, U. Vetter, H. Hofsäss, H. Gibhardt, G. Eckold, Q. Lic, S. Lee, Y. Huang, and M. Seibt. Ion beam synthesis of amorphous carbon thin films containing metallic nanoclusters. *Surf. Coat. Technol.* **158 - 159**, 114 (2002).

[Gil97] K. W. R. Gilkes, H. S. Sands, D. N. Batchelder, J. Robertson, and W. I. Milne. Direct observation of sp^3 bonding in tetrahedral amorphous carbon using ultraviolet raman spectroscopy. *Appl. Phys. Lett.* **70**, 1980 (1997).

[Gil00] K. W. R. Gilkes, S. Prawer, K. W. Nugent, J. Robertson, H. S. Sands, Y. Lifshitz, and X. Shi. Direct quantitative detection of the sp^3 bonding in diamond-like carbon films using ultraviolet and visible raman spectroscopy. *J. Appl. Phys.* **87**, 7283 (2000).

[Gri99] A. Grill. Diamond-like carbon: state of the art. *Diamond Relat. Mater.* **8**, 428 (1999).

[Gri11] L. Grieten, S. D. Janssens, A. Ethirajan, N. V. Bon, M. Ameloot, L. Michiels, K. Haenen, and P. Wagner. Real-time study of protein adsorption on thin nanocrystalline diamond. *Phys. Status Solidi A* **208**, 2093 (2011).

[Hak95] M. Hakovirta, J. Sale, R. Lappalainen, and A. Anttila. Correlation of carbon ion energy with sp^2/sp^3 ratio in amorphous diamond films produced with a mass-separated ion beam. *Physics Letters A* **205**, 287 (1995).

[Hal59] C. E. Hall and H. S. Slayter. The fibrinogen molecule: Its size, shape, and mode of polymerization. *J. Biophysic. Biochem. Cytol.* **5**, 11 (1959).

[Has07] T. Hasebe, S. Nagashima, A. Kamijo, T. Yoshimura, T. Ishimaru, Y. Yoshimoto, S. Yohena, H. Kodama, A. Hotta, K. Takahashi, and T. Suzuki. Depth profiling of fluorine-doped diamond-like carbon (F-DLC) film: Localized fluorine in the top-most thin layer can enhance the non-thrombogenic properties of F-DLC. *Thin Solid Films* **516**, 299 (2007).

[Hau03] R. Hauert. A review of modified DLC coatings for biological applications. *Diamond Relat. Mater.* **12**, 583 (2003).

[Her50] C. Herring. Effect of change of scale on sintering phenomena. *J. Appl. Phys.* **21**, 301 (1950).

[Him88] F. J. Himpsel, F. R. McFee, A. Taleb-Ibrahimi, and J. A. Yarmoff. Microscopic structure of the SiO_2/Si interface. *Phys. Rev. B* **38**, 6084 (1988).

[Hof93] H. Hofsäss, H. Binder, T. Klumpp, and E. Recknagel. Doping and growth of diamond-like carbon films by ion beam deposition. *Diamond Relat. Mater.* **3**, 137 (1993).

[Hof98] H. Hofsäss, H. Feldermann, R. Merk, M. Sebastian, and C. Ronning. Cylindrical spikemodel for the formation of diamondlike thin films by ion deposition. *Appl. Phys. A: Mater. Sci. Process.* **66**, 153 (1998).

[Hof13a] H. Hofsäss, O. Bobes, and K. Zhang. Is sputtering relevant for ion-induced self-organized pattern formation? *AIP Conf. Proc.* **1525**, 386 (2013).

[Hof13b] H. Hofsäss, K. Zhang, H. G. Gehrke, and C. Brüsewitz. Propagation of ripple patterns on si during ion bombardment. *Phys. Rev. B* **88**, 075426 (2013).

[Hof13c] H. Hofsäss, K. Zhang, A. Pape, O. Bobes, and M. Brötzmann. The role of phase separation for self-organized surface pattern formation by ion beam erosion and metal atom co-deposition. *Appl. Phys. A: Mater. Sci. Process.* **111**, 653 (2013).

[Hof14] H. Hofsäss. Surface instability and pattern formation by ion-induced erosion and mass redistribution. *Appl. Phys. A* **114**, 401 (2014).

[Hon98] Y. K. Hong, J.-J. Kim, C. Park, J. S. Kim, and J. K. Kim. Field electron emission of diamondlike carbon films deposited by a laser ablation method. *J. Vac. Sci. Technol., B* **16**, 729 (1998).

[Hön10] J. Hönig. *Untersuchungen zur Adsorption von Proteinen auf nanostrukturierten Oberflächen.* Diploma thesis, Friedrich-Schiller-Universität Jena (2010).

[Ish87] J. Ishikawa, Y. Takeiri, K. Ogawa, and T. Takagi. Transparent carbon film prepared by mass-separated negative carbon ion beam deposition. *J. Appl. Phys.* **61**, 2509 (1987).

[Ism07] F. S. M. Ismail, R. Rohanizadeh, S. Atwa, R. S. Mason, A. J. Ruys, P. J. Martin, and A. Bendavid. The influence of surface chemistry and topography on the contact guidance of MG63 osteoblast cells. *J. Mater. Sci.: Mater. Med.* **18**, 705 (2007).

[Jel10] M. Jelínek, T. Kocourek, J. Remsa, J. Mikšovský, J. Zemek, K. S. Jr., B. Dvořánková, and T. Luxbacher. Diamond/graphite content and biocompatibility of DLC films fabricated by PLD. *Appl. Phys. A* **101**, 579 (2010).

[Joh02] P. John, N. Polwart, and J. W. C.E. Troupe and. The oxidation of (100) textured diamond. *Diamond Relat. Mater.* **11**, 861 (2002).

[Jun03] S.-Y. Jung, S.-M. Lim, F. Albertorio, G. Kim, M. C. Gurau, R. D. Yang, M. A. Holden, and P. S. Cremer. The Vroman effect: A molecular level description of fibrinogen displacement. *J. Am. Chem. Soc.* **125**, 12782 (2003).

[Kal08] N. Kalyanasundaram, M. Ghazisaeidi, J. B. Freund, and H. T. Johnson. Single impact crater functions for ion bombardment of silicon. *Appl. Phys. Lett.* **92**, 131909 (2008).

[Kas87] S. Kasi, H. Kang, and J. W. Rabalais. Chemically bonded diamondlike carbon films from ion-beam deposition. *Phys. Rev. Lett.* **59**, 75 (1987).

[Kee08]   I. V. D. Keere, R. Willaert, A. Hubin, and J. Vereecken. Interaction of human plasma fibrinogen with commercially pure titanium as studied with atomic force microscopy and x-ray photoelectron spectroscopy. *Langmuir* **24**, 1844 (2008).

[Kel10]   A. Keller and S. Facsko. Ion-induced nanoscale ripple patterns on si surfaces: Theory and experiment. *Materials* **3**, 4811 (2010).

[Kel11]   T. F. Keller, J. Schönfelder, J. Reichert, N. Tuccitto, A. Licciardello, G. M. L. Messina, G. Marletta, and K. D. Jandt. How the surface nanostructure of polyethylene affects protein assembly and orientationv. *ACS Nano* **5**, 3120 (2011).

[Kie95]   W. Kiefer. *Spektroskopie amorpher und kristalliner Festkörper*. Steinkopf Verlag, Darmstadt (1995).

[Kim03]   J. Kim and G. A. Somorjai. Molecular packing of lysozyme, fibrinogen, and bovine serum albumin on hydrophilic and hydrophobic surfaces studied by infrared-visible sum frequency generation and fluorescence microscopy. *J. Am. Chem. Soc.* **125**, 3150 (2003).

[Koc08]   T. Kocourek, M. Jelinek, V. Vorlíček, J. Zemek, T. Janča, V. Žížková, J. Podlaha, and C. Popov. DLC coating of textile blood vessels using PLD. *Appl. Phys. A: Mater. Sci. Process.* **93**, 627 (2008).

[Kop95]   I. Koponen, M. Hakovirta, and R. Lappalainen. Modeling the ion energy dependence of the sp^3/sp^2 bonding ratio in amorphous diamondlike films produced with a mass-separated ion beam. *J. Appl. Phys.* **78**, 5837 (1995).

[Kop97]   I. Koponen, M. Hautala, and O.-P. Sievänen. Simulations of ripple formation on ion-bombarded solid surfaces. *Phys. Rev. Lett.* **78**, 2612 (1997).

[Kos11]   S. Kosan. *Ionenstrahlerosion von TiO$_2$*. bachelor thesis, Friedrich-Schiller-Universität Jena (2011).

[Kow99]   T. Kowalewski and D. M. Holtzmann. In situ atomic force microscopy study of alzheimers β-amyloid peptide on different substrates: New insights into mechanism of β-sheet formation. *Proc. Natl. Acad. Sci. U. S. A.* **96**, 3688 (1999).

[Lau91]   W. M. Lau, I. Bello, X. Feng, L. J. Huang, and Q. F. et al. Direct ion beam deposition of carbon films on silicon in the ion energy range of 15500 ev. *J. Appl. Phys.* **70**, 5623 (1991).

[Lau07]   N. Laube, L. Kleinen, J. Bradenahl, and A. Meissner. Diamond-like carbon coatings on ureteral stentsa new strategy for decreasing the formation of crystalline bacterial biofilms? *J. Urol.* **177**, 1923 (2007).

[Lia12]   W.-H. Liao, C.-R. Lin, D.-H. Wei, Y.-R. Shen, Y.-C. Li, J.-A. Lee, and C.-Y. Liang. Concurrent improvement in biocompatibility and bioinertness of diamond-like carbon films with nitrogen doping. *J. Biomed. Mater. Res., Part A* **100A**, 3151 (2012).

[Lif90]   Y. Lifshitz, S. R. Kasi, J. Rabalais, and W. Eckstein. Subplantation model for film growth from hyperthermal species. *Phys. Rev. B* **41**, 10468 (1990).

[Lif95]   Y. Lifshitz, G. Lempert, E. Grossman, I. Avigal, C. Uzan-Saguy, R. Kalish, J. Kulik, D. Marton, and J. Rabalais. Growth mechanisms of dlc films from C$^+$ ions: experimental studies. *D, Diamond Relat. Mater.* **4**, 318 (1995).

[Lif96]   Y. Lifshitz. Hydrogen-flee amorphous carbon films: correlation between growth conditions and properties. *Diamond Relat. Mater.* **5**, 388 (1996).

[Lif99]   Y. Lifshitz. Diamond-like carbon : present status. *Diamond Relat. Mater.* **8**, 1659 (1999).

[Lin86]   J. Lindon, G. McManama, L. Kushner, E. Merrill, and E. Salzman. Does the conformation of adsorbed fibrinogen dictate platelet interactions with artificial surfaces? *Blood* **68**, 355 (1986).

[Liu04]   X. Liu, P. K. Chu, and C. Ding. Surface modification of titanium, titanium alloys, and related materials for biomedical applications. *Mater. Sci. Eng. R* **47**, 49 (2004).

[Liu08]   A. Liu, J. Han, J. Zhu, S. Meng, and X. He. Evaluation on corrosion behavior and haemocompatibility of phosphorus incorporated tetrahedral amorphous carbon films. *Mater. Sci. Eng., C* **28**, 1408 (2008).

[Lok06]   C.-N. Lok, C.-M. Ho, R. Chen, Q.-Y. He, W.-Y. Yu, H. Sun, P. K.-H. Tam, J.-F. Chiu, and C.-M. Che. Proteomic analysis of the mode of antibacterial action of silver nanoparticles. *J. Proteome Res.* **5**, 916 (2006).

[Lor10]   M. S. Lord, M. Foss, and F. Besenbacher. Influence of nanoscale surface topography on proteinadsorption and cellular response. *Nano Today* **5**, 66 (2010).

[Lui09]   A. Luican, G. Li, and E. Y. Andrei. Scanning tunneling microscopy and spectroscopy of graphene layers on graphite. *Solid State Commun.* **149**, 1151 (2009).

[Mac92]   S. W. MacLaren, J. E. Baker, N. L. Finnegan, and C. M. Loxton. Surface roughness development during sputtering of gaas and inp: Evidence for the role of surface diffusion in ripple formation and sputter cone development. *J. Vac. Sci. Technol., A* **10**, 468 (1992).

[Mad11]   C. S. Madi, E. Anzenberg, J. Karl F. Ludwig, and M. J. Aziz. Mass redistribution causes the structural richness of ion-irradiated surfaces. *Phys. Rev. Lett.* **106**, 066101 (2011).

[Mak97]   M. A. Makeev and A.-L. Barabasi. Ion-induced effective surface diffusion in ion sputtering. *Appl. Phys. Lett.* **71**, 2800 (1997).

[Mak02]   M. A. Makeev, R. Cuerno, and A.-L. Barabasi. Morphology of ion-sputtered surfaces. *Nucl. Instrum. Methods Phys. Res., Sect. B* **197**, 185 (2002).

[Man08]   D. J. Manura and D. A. Dahl. *SIMION Version 8.0 user Manual.* Scientific Instrument Services, 1027 Old York Rd, Ringoes, NJ 08551, USA (2008).

[Mar03]   K. L. Marchin and C. L. Berrie. Conformational changes in the plasma protein fibrinogen upon adsorption to graphite and mica investigated by atomic force microscopy. *Langmuir* **19**, 9883 (2003).

[McK91]   D. R. McKenzie, D. Muller, and B. A. Pailthorpe. Compressive-stress-induced formation of thin-film tetrahedral amorphous carbon. *Phys. Rev. Lett.* **67**, 773 (1991).

[McK05]   D. McKenzie, A. Merchant, D. McCulloch, H. Malloch, N. Marks, and M. Bilek. Ab initio studies of amorphous carbon films. *Surf. Coat. Technol.* **198**, 212 (2005).

[Mel10]   C. Melis, A. Mattoni, and L. Colombo. Atomistic investigation of poly(3-hexylthiophene) adhesion on nanostructured titania. *J. Phys. Chem.* **114**, 3401 (2010).

[Miy84]   T. Miyazawa, S. Misawa, S. Yoshida, and S. Gonda. Preparation and structure of carbon film deposited by a massseparated C^+ ion beam. *J. Appl. Phys.* **55**, 188 (1984).

[Möl84]   W. Möller and W. Eckstein. TRIDYN - a TRIM simulation code including dynamic composition changes. *Nucl. Instrum. Methods Phys. Res., Sect. B* **2**, 814 (1984).

[Möl88]   W. Möller, W. Eckstein, and J. B. Biersack. TRIDYN - binary collision simulation of atomic collisions and dynamic composition changes in solids. *Comput. Phys. Commun.* **51**, 355 (1988).

[Möl14]   W. Möller. TRI3DYN collisional computer simulation of the dynamic evolution of 3-dimensional nanostructures under ion irradiation. *Nucl. Instrum. Methods Phys. Res., Sect. B* **322**, 23 (2014).

[Mos78]   P. R. Moses, L. M. Wier, J. C. Lennox, H. . Finklea, J. R. Lenhard, and R. W. Murray. X-ray photoelectron spectroscopy of alkylamine-silanes bound to metal oxide electrodes. *Anal. Chem.* **50**, 576 (1978).

[Mou92]   J. F. Moulder, W. F. Stickle, P. E. Sobol, and K. D. Bomben. *Handbook of X-ray Spectroscopy.* Perkin-Elmer Corporation, Physical Eletronics Devision, 6509 Flying Cloud Drive, Eden Prairie, Minnesota 55344, United States of America (1992).

[Mér98]   P. Mérel, M. Tabbal, M. Chaker, S. Moisa, and J. Margot. Direct evaluation of the sp^3 content in diamond-like-carbon films by xps. *Appl. Surf. Sci.* **136**, 105 (1998).

[Mul57]   W. W. Mullins. Theory of thermal grooving. *J. Appl. Phys.* **23**, 333 (1957).

[Nag75]   H. M. Naguib and R. Kelly. Criteria for bombardment-induced structural changes in non-metallic solids. *Radiat. Eff. Defects Solids* **25**, 1 (1975).

[Nar05]   R. J. Narayan. Nanostructured diamondlike carbon thin films for medical applications. *Mater. Sci. Eng., C* **25**, 405 (2005).

[Nef77]   V. Nefedov, Y. Salyn, G. Leonhardt, and R. Scheibe. A comparison of different spectrometers and charge corrections used in X-ray photoelectron spectrospcopy. *J. Electron Spectrosc. Relat. Phenom.* **10**, 121 (1977).

[OV98]   J. Ortega-Vinuesa, P. Tengvall, and I. Lundström. Molecular packing of HSA, IgG, and fibrinogen adsorbed on silicon by AFM imaging. *Thin Solid Films* **324**, 257 (1998).

[Pan09]   Z. Pan, H. Sun, Y. Zhang, and C. Chen. Harder than diamond: Superior indentation strength ofwurtzite bn and lonsdaleite. *Phys. Rev. Lett.* **102**, 055503 (2009).

[Pen01]   X. Peng, Z. Barber, and T. Clyne. Surface roughness of diamond-like carbon films prepared using various techniques. *Surf. Coat. Technol.* **138**, 23 (2001).

[Pie93]   H. O. Pierson. *Handbook of Carbon, graphite, Diamond and Fullerenes*. Noyes Publications, Park Ridge (1993).

[Pra96]   S. Prawer, K. Nugent, Y. Lifshitz, G. Lempert, E. Grossmann, J. Kulik, I. Avigal, and R. Kalish. Systematic variation of the raman spectra of fld films as a function of sp^2 : $sp^3 composition. Diamond Relat. Mater. 5, 433 (1996).$

[Pís13]   P. Písařík, M. Jelínek, K. S. Jr., B. Dvořánková, T. Kocourek, J. Zemek, and D. Chvostová. Study of optical properties and biocompatibility of dlc films characterized by sp^3 bonds. *Appl. Phys. A* **112**, 143 (2013).

[Ras94]   J. R. Rasmusson, E. Erlandson, W. R. Salaneck, M. Schott, D. T. Clark, and I. Lundström. Adsorption of fibrinogen on thin oriented poly(tetrafluoroethylene) (ptfee) fibres sudied by scanning force microscopy. *Scanning Microsc.* **8**, 481 (1994).

[Rez10]   B. Rezek, M. Krátká, A. Kromka, and M. Kalbacova. Effects of protein inter-layers on celldiamond fet characteristics. *Biosens. Bioelectron.* **26**, 1307 (2010).

[Ric96]   F. Richter. Superharte dünne schichten. *Phys. Bl.* **52**, 355 (1996).

[Rie04]   E. Riedel. *Allgemeine und Anorganische Chemie*, volume 8. de Gruyter, Berlin (2004).

[Rie11]   N. A. Riedel, J. D. Williams, and K. C. Popat. Ion beam etching titanium for enhanced osteoblast response. *J. Mater. Sci* **46**, 6087 (2011).

[Roa05]   P. Roach, D. Farrar, and C. C. Perry. Interpretation of protein adsorption: Surface-induced conformational changes. *J. Am. Chem. Soc.* **127**, 8168 (2005).

[Roa06]   P. Roach, D. Farrar, and C. C. Perry. Surface tailoring for controlled protein adsorption: Effect of topography at the nanometer scale and chemistry. *J. Am. Chem. Soc.* **128**, 3939 (2006).

[Rob86]   J. Robertson. Amorphous carbon. *Advances in Physics* **35**, 317 (1986).

[Rob93]   J. Robertson. Deposition mechanisms for promoting sp^3 bonding in diamond-like carbon. *Diamond Relat. Mater.* **2**, 984 (1993).

[Rob94]   J. Robertson. The deposition mechanism of diamond-like a-C and a-C: H. *Diamond Relat. Mater.* **3**, 361 (1994).

[Ron97]   C. Ronning, E. Dreher, J.-U. Thiele, P. Oelhafen, and H. Hofsäss. Electronic and atomic structure of undoped and doped ta-C films. *Diamond Relat. Mater.* **6**, 830 (1997).

[Roy07]   R. K. Roy and K.-R. Lee. Biomedical applications of diamond-like carbon coatings: A review. *J. Biomed. Mater. Res., Part B: Appl. Biomater* **83B**, 72 (2007).

[Sch53]   H. Schmellenmeier. Die beeinflussung von festen oberflächen durch eine ionisierte gasatmosphäre. *Experimentelle Technik der Physik* **1**, 49 (1953).

[Sch57]   H. A. . Scheraga and J. . Michael Laskowski. The fibrinogen-fibrin conversion (1957).

[Sch97]   H.-J. Scheibe, B. Schultrich, H. Ziegele, and P. Siemroth. Deposition of superhard amorphous carbon films by pulsed arc sources. *IEEE Trans. Plasma Sci.* **25**, 685 (1997).

[Sch98]   B. Schultrich, H.-J. Scheibe, D. Drescher, and H. Ziegele. Deposition of superhard amorphous carbon films by pulsed vacuum arc deposition. *Surf. Coat. Technol.* **98**, 1097 (1998).

[Sei57]   F. Seitz and J. Koeler. *Progress in Solid State Physics*, volume 12. Academic Press, New York (1957).

[Shi72]   D. A. Shirley. High resolution X-ray photoemission spectrum of the valence bands of gold. *Phys. Rev. B* **5**, 4709 (1972).

[Shi05]   D. Shindo, T. Musashi, Y. Ikematsu, Y. Murakami, N. Nakamura, and H. Chiba. Characterization of DLC films by EELS and electron holography. *Journal of Electron Microscopy* **54**, 11 (2005).

[Shi14]   T. Shinonaga, M. Tsukamoto, A. Nagai, K. Yamashita, T. Hanawa, N. Matsushita, G. Xie, and N. Abe. Cell spreading on titanium dioxide film formed and modifiedwith aerosol beam and femtosecond laser. *Appl. Surf. Sci.* **288**, 649 (2014).

[Sie10]   D. Siegismund, T. F. Keller, K. D. Jandt, and M. Rettenmayr. Fibrinogen adsorption on biomaterials a numerical study. *Macromol. Biosci.* **10**, 1216 (2010).

[Sig69]   P. Sigmund. Theory of sputtering. I - Sputtering yield of amorphous and polycrystalline targets. *Phys. Rev.* **184**, 383 (1969).

[Sig73]   P. Sigmund. A mechanism of surface micro-roughening by ion bombardment. *J. Mater. Sci* **8**, 1545 (1973).

[Sit99]   P. S. Sit and R. E. Marchant. Surface-dependent conformations of human fibrinogen observed by atomic force microscopy under aqueous conditions. *Thromb. Haemost.* **82**, 1053 (1999).

[Soi09]   A. Soininen, V.-M. Tiainen, Y. T. Konttinen, H. C. van der Mei, H. J. Busscher, and P. K. Sharma. Bacterial adhesion to diamond-like carbon as compared to stainless steel. *J. Biomed. Mater. Res., Part B* p. 882 (2009).

[Som12]   J. Sommerfeld, J. Richter, R. Niepelt, S. Kosan, T. F. Keller, K. D. Jandt, and C. Ronning. Protein adsorption on nano-scaled, rippled TiO_2 and Si surfaces. *Biointerphases* **7** (2012).

[Spe76]   E. G. Spencer, P. H. Schmidt, D. C. Joy, and F. J. Sansalone. Ion-beam-deposited polycrystalline diamondlike films. *Appl. Phys. Lett.* **29**, 118 (1976).

[Sri12]   S. Srinivasan, Y. Tang, Y. Li, Q. Yang, and A. Hirose. Ion beam deposition of DLC and nitrogen doped DLC thin films for enhanced haemocompatibility on PTFE. *Appl. Surf. Sci.* **258**, 8094 (2012).

[Sti03]   H. Stillrich. *Erweiterungen und Tests an einer Anlage zur massenseparierten Ionenstrahldeposition.* Master's thesis, Georg-August-Universität zu Göttingen (2003).

[Stu10]   S. I. Stupp. Self-assembly and biomaterials. *Nano Lett.* **10**, 4783 (2010).

[Ta98]   T. C. Ta, M. T. Sykes, and M. T. McDermott. Real-time observation of plasma protein film formation on well-defined surfaces with scanning force microscopy. *Langmuir* **14**, 2435 (1998).

[Tun05]   S. Tunc, M. F. Maitz, G. Steiner, L. Vázquez, M. T. Pham, and R. Salzer. In situ conformational analysis of fibrinogen adsorbed on Si surfaces. *Colloids Surf., B* **42**, 219 (2005).

[Uhl98]   S. Uhlmann and T. Frauenheim. Molecular-dynamics study of the fundamental processes involved in subplantation of diamondlike carbon. *Phys. Rev. Lett.* **81**, 641 (1998).

[Umb01]   C. C. Umbach, R. L. Headrick, and K.-C. Chang. Spontaneous nanoscale corrugation of ion-eroded SiO_2: The role of ion-irradiation-enhanced viscous flow. *Phys. Rev. Lett.* **87**, 246104 (2001).

[Uzu08]   E. T. Uzumaki, C. S. Lambert, and W. D. B. andC. A. C. Zavaglia. Biocompatibility of titanium based implants with diamond-like carbon coatings produced by plasma immersion ion implantation and deposition. *Key Engineering Materials Vols.* **361 - 363**, 677 (2008).

[Vaj96]   J. J. Vajo, R. E. Doty, and E.-H. Cirlin. Influence of O_2^{+2} energy, flux, and fluence on the formation and growth of sputtering-induced ripple topography on silicon. *J. Vac. Sci. Technol., A* **14**, 2709 (1996).

[Vie09]   E. P. Vieira, S. Rocha, M. C. Pereira, H. Möhwald, and M. A. N. Coelho. Adsorption and diffusion of plasma proteins on hydrophilic and hydrophobic surfaces: Effect of trifluoroethanol on protein structure. *Langmuir* **25**, 9879 (2009).

[vM14]   A. v. Müller. *Investigations of ion beam induced nanoscale ripple patterns and their effect on protein-surface adsorption.* Master's thesis, Friedrich-Schiller-Universität Jena (2014).

[Wan14] Y. Wang, C. Wen, P. Hodgson, and Y. Li. Biocompatibility of TiO_2 nanotubes with different topographies. *J. Biomed. Mater. Res., Part A* **102A**, 743 (2014).

[Was10] J. Wasyluk, T. Perova, D. Lau, M. Taylor, D. McCulloch, and J. Stopford. Ultraviolet and visible raman analysis of thin a-C films grown by filtered cathodic arc deposition. *Diamond Relat. Mater.* **19**, 514 (2010).

[Wei79] C. Weissmantel, K. Bewilogua, C. Schurer, K. Breuer, and H. Zscheile. Characterization of hard carbon films by electron energy loss spectrometry. *Thin Solid Films* **61**, L1 (1979).

[Wen02] K.-W. Weng, C.-L. Chang, and D.-Y. Wang. Effect of ion energy on degradation of diamond-like carbon films exposed to high-energy bombardment from an ion implanter. *Diamond Relat. Mater.* **11**, 1447 (2002).

[Wil09] D. F. Williams. On the nature of biomaterials. *Biomaterials* **30**, 5897 (2009).

[Wil11] M. Wille. *Qualitative Untersuchung diamantähnlicher Schichten, hergestellt mittels Massenseparierter Ionenstrahldeposition (MSIBD)*. Master's thesis, Friedrich-Schiller-Universität Jena (2011).

[Yam10] K. Yamamoto. Chemical bond analysis of amorphous carbon films. *Vacuum* **84**, 638 (2010).

[Yew05] E. O. Yewande, A. K. Hartmann, and R. Kree. Propagation of ripples in monte carlo models of sputter-induced surface morphology. *Phys. Rev. B: Condens. Matter Mater. Phys* **71**, 195405 (2005).

[Yu03] J.-G. Yu, H.-G. Yu, B. Cheng, X.-J. Zhao, J. C. Yu, and W.-K. Ho. The effect of calcination temperature on the surface microstructure and photocatalytic activity of TiO_2 thin films prepared by liquid phase deposition. *J. Phys. Chem. B* **107**, 13871 (2003).

[Zha09] K. Zhang, H. Hofsäss, F. Rotter, M. Uhrmacher, C. Ronning, and J. Krauser. Morphology of Si surfaces sputter-eroded by low-energy Xe-ions at glancing incident angle. *Surf. Coat. Technol.* **203**, 2395 (2009).

[Zie85] J. F. Ziegler, J. Biersack, and U. Littmark. *The stopping and range of ions in solids*, volume 1. Pergamon Press (1985).

Ehrenwörtlich Erklärung

Ich erkläre hiermit ehrenwörtlich, dass ich die vorliegende Arbeit selbstständig, ohne unzulässige Hilfe Dritter und ohne Benutzung anderer als der angegebenen Hilfsmittel und Literatur angefertigt habe. Die aus anderen Quellen direkt oder indirekt übernommenen Daten und Konzepte sind unter Angabe der Quelle gekennzeichnet.

Bei der Auswahl und Auswertung folgenden Materials haben mir nachstehend aufgeführte Personen in der jeweils beschriebenen Weise unentgeltlich geholfen:

- Die SEM Untersuchungen wurde in Zusammenarbeit mit Marcel Wille durchgeführt

- Die Erzeugung der Ripples auf Silicium und Titandioxid und deren Vermessung mittels AFM erfolgte in enger Zusammenarbeit mit Jessica Richter (geb. Hönig), Maria Fravventura, Stefanie Eckner (geb. Kosan) und Alexander v. Müller im Rahmen ihrer jeweiligen Master- bzw. Bachelorarbeiten.

- Die Planung, Durchführung und Auswertung der Adsorptionsexperimente erfolgte in enger Zusammenarbeit mit Dr. Thomas Keller, Jessica Richter (geb. Hönig), Alexander v. Müller.

- Sämtliche XPS Messungen wurden von Ralf Wagner durchgeführt.

- Mike Mühlstädt und Dr. Thomas Keller waren bei der Auswertung der XPS Daten hilfreich.

- Die Raman-Messungen erfolgten überwiegend in Zusammenarbeit mit Marcel Wille, Stephan Stöckel und Dr. Nicolae Tarcea. Ihre Auswertung erfolgte in enger Zusammenarbeit mit Marcel Wille im Rahmen seiner Masterarbeit. Einige Messungen erfolgten in Zusammenarbeit mit Dr. Linda Prinsloo an der Universität von Pretoria (Südafrika).

- Kontaktwinkelmessungen wurden mit Jessica Richter, Dr. Thomas Keller und Christian Helbing durchgeführt.

Weitere Personen waren an der inhaltlich-materiellen Erstellung der vorliegenden Arbeit nicht beteiligt. Insbesonderere habe ich hierfür nicht die entgeltliche Hilfe von Vermittlungs- bzw. Beratungsdiensten (Promotionsberater oder andere Personen) in

Anspruch genommen. Niemand hat von mir unmittelbar oder mittelbar geldwerte Leistungen für Arbeiten erhalten, die im Zusammenhang mit dem Inhalt der vorgelegten Dissertation stehen.

Die Arbeit wurde bisher weder im In- noch im Ausland in gleicher oder ähnlicher Form einer anderen Prüfungsbehörde vorgelegt.

Die geltende Promotionsordnung der Physikalisch-Astronomischen Fakultät ist mir bekannt.

Ich versichere ehrenwörtlich, dass ich nach bestem Wissen die reine Wahrheit gesagt und nichts verschwiegen habe.

Jena, 02. April 2014

---

[1]Faust. Der Tragödie erster Teil, J. W. v. Goethe, 1808